The University of Nottingham
School of Physics & Astronomy

INVESTIGATION OF STRUCTURAL, ELECTRICAL AND OPTICAL PROPERTIES OF DOPED DILUTE GaAsBi GROWN BY MOLECULAR BEAM EPITAXY

by

SULTAN SALEH ALHASSAN

M. Sc (Physics)

Thesis submitted to the University of Nottingham

for the degree of Doctor of Philosophy

February 2022

ABSTRACT

This thesis reports an investigation of the strutural, electrical and optical properties of dilute bimuth (Bi) containing semiconductors materials, namely GaAsBi grown by Molecular Beam Epitaxy (MBE) on GaAs substrates at low temperature. It is well known that the addition of a few percent of Bi in GaAs compound semiconductors has been shown to dramatically reduce the energy bandgap of host material. This remarkable bandgap reduction has several applications in long-wavelength lasers, solar cells, and photonic devices. However, the insertion of these impurity atoms causes defect levels in the bandgap of semiconductor materials. These can have serious effects for the quality of the material, for example, they can reduce charge carrier lifetime and reduce optical efficiency. Indeed, determining the nature and features of the defects existing in the materials, which is critical for many device applications, will improve and help in understanding their implications on the quality of materials and devices performance. In this work, an investigation will be reported on the effect of the orientation of the substrates on the structural, electrical and optical properties of dilute $GaAs_{1-x}Bi_x$ epilayers structures having a Bi composition x = ~5.4%, grown by MBE on (100) and (311)B GaAs planes. The results of this study show that the detected defects affected significantly the electrical and optical properties of semiconductor structures and devices. In particular, X-ray diffraction results revealed that the in-plane strain in the Ga(As,Bi) layer of the samples grown on (100)-oriented substrates is significantly larger than that of the samples grown on (311)B-oriented substrates. Deep Level Transient Spectroscopy (DLTS) measurements showed that the number of electrically active traps were different for the two GaAs substrate orientations.

In particular, three and two electron traps are detected in samples grown on (100) and (311)B GaAs substrates, respectively, with activation energies ranging from 0.12 to 0.41 eV. The observed traps with small activation energies are attributed to Bi pair defects. The photoluminescence (PL) and Raman spectra have evidenced different compressive strain which affects considerably the optical properties. In addition, a further investigation was carried out to study the effect of gamma radiation dose on the electrical and optical properties of dilute GaAsBi layer grown by MBE on a highly doped (100) GaAs substrates. The DLTS revealed that after irradiation the number of electrically active traps decreased. Four, three and two electron traps were detected in as-grown and irradiated samples with 50 kGy and 100 kGy doses, respectively. The PL intensity of the main peak was found to increase with the irradiation dose, evidencing an enhancement of the optical properties and annihilation/contributions of Bi- related traps, and supporting the electrical results. Additionally, this thesis reports the structural and optical properties of n-type Si-doped and p-type Be-doped GaAs$_{1-x}$Bi$_x$ thin films grown by MBE on (311)B GaAs substrates. The experimental studies demonstrate that, the composition of Bi incorporated in both n-type and p-type doped GaAsBi was similar, despite that the samples present remarkable differences in the number of Bi related defects, non-radiative centers and alloy disorder. Particularly, the results evidence that the Bi-related defects in n- and p-doped GaAsBi alloys have important impact on the differences of their optical properties.

PUBLICATIONS

1. Investigation of the effect of substrate orientation on the structural, electrical and optical properties of n-type $GaAs_{1-x}Bi_x$ layers grown by Molecular Beam Epitaxy.
   Sultan Alhassan, Daniele de Souza, Amra Alhassni, Saud Alotaibi, Abdulaziz Almalki, Maryam Alhuwayz, Igor P. Kazakov, Elkhan. M. Pashaev, Alexey V. Klekovkin, Sergio Souto, Yara Galvão Gobato, Noor Al Saqri, Helder Vinicius Avanço Galeti, Faisal S Al Mashary, Hind Albalawi, Norah Alwadai, and Mohamed Henini
   Journal of Alloys and Compounds **885**, 161019 (2021)

2. Structural and optical properties of n-type and p-type $GaAs_{(1-x)}Bi_x$ thin films grown by molecular beam epitaxy on (311)B GaAs substrates.
   Daniele de Souza, Sultan Alhassan, Saud Alotaibi, Amra Alhassni, Amjad Almunyif, Igor P. Kazakov, Alexey V. Klekovkin, Sergey A. Zinov'ev , Igor A. Likhachev, Elkhan. M. Pashaev, Sergio Souto, Yara Galvão Gobato, Helder Vinicius Avanço Galeti, Mohamed Henini
   Semiconductor Science and Technology **36**, 075018 (2021)

3. Effect of thermal annealing on the optical and structural properties of (311)B and (001) GaAsBi/GaAs single quantum wells grown by MBE.
   Haifa Alghamdi, Vanessa Orsi Gordo, Martin Schidbauer, Jorlandio F. Felix, Sultan Alhassan, Amra Alhassani, Gabriela Augusta Prando, Horacio Coelho-Junior, Mustafa Gunes, Helder Vinicus Avanco Galeti, Yara Galvao Gobato, and Mohamed Henini
   Journal of Applied Physics **127**, 125704 (2020)

4. The effect of strain and spatial Bi distribution on the band alignment of GaAsBi single quantum well structure.
   M. Gunes, O. Donmez, G. Gumus, A. Erol, H. Alghamdi, Sultan Alhassan, A. Alhassani, S. Alotaibi, M. Schmidbauer, H.V.A Galeti, M. Henini
   Physica B: Physics of Condensed Matter **602**, 412487 (2020)

5. Effect of bismuth surfactant on the structural, morphological and optical properties of self-assembled InGaAs quantum dots grown by Molecular Beam Epitaxy on GaAs (001) substrates.
   Haifa Alghamdi, Amra Alhassni, Sultan Alhassan, Amjad Almunyif, Alexey V. Klekovkin, Igor N. Trunkin, Alexander L. Vasiliev, Helder V. A. Galeti, Yara Galvão Gobato, Igor P. Kazakov, Mohamed Henini.

Journal of Alloys and Compounds **905**, 164015 (2022)

6. Investigation of the effect of gamma radiation on the electrical and optical properties of dilute $GaAs_{1-x}Bi_x$ grown on Molecular Beam Epitaxy.
   Sultan Alhassan, Faisal S Al Mashary, Jorlandio Francisco Felix, Walter de Azevedo, Amra Alhassni, Amjad Almunyif, Saud Alotaibi, Abdulaziz Almalki, Maryam Alhuwayz, Haifa Alghamdi, Noor Al Saqri, Igor P. Kazakov, Hind Albalawi, and Mohamed Henini.
   Submitted to Radiation Physics and Chemistry

7. Current-induced degradation behaviors of InGaN/GaN multiple-quantum-well UV photodetectors: Role of electrically active defects.
   Pradip Dalapati, Abdulaziz Almalki, Sultan Alhassan, Saud Alotaibi, Maryam Al Huwayz, Taiki Nakabayashi, Takashi Egawa, Makoto Miyoshi, Mohamed Henini.
   Submitted to Applied Surface Science

CONFERENCE PRESENTATIONS

POSTER PRESENTATIONS

- "Investigation on the effect of crystal orientation and doping type on the optical properties of bulk GaAsBi thin films"
  The 10th International Workshop on Bismuth-Containing Semiconductors, Toulouse, France, July 21-24 (2019)

- "Investigation of the effect of substrate orientations on the electrical properties of n-type $GaAs_{1-x}Bi_x$ layers grown by Molecular Beam Epitaxy"
  11th International Conference on Quantum Dots (QD2020).
  Munich, Germany, December 7 -11 (2020)

- "Investigation of the effect of gamma radiation on the electrical properties of n-type $GaAs_{1-x}Bi_x$ layers grown by Molecular Beam Epitaxy"
  31st International Conference on Defects in Semiconductors.
  Oslo, Norway, July 26 - 30 (2021)

ACKNOWLEDGEMENTS

Foremost, I want to express my gratitude to Allah Almighty for providing me with the strength, knowledge, and ability to continue with this thesis, endure, and successfully complete it.

It is my pleasure and honor to express my thankful to those who made this thesis achievable.

I would like to express my sincere gratitue to my supervisor, Prof. **Mohamed Henini,** for the continuous support of my Ph.D study and research, for his patience, motivation, enthusiasm, and immense knowledge. His guidance and advice were invaluable during the research and writing of this thesis. Also, I owe him a debt of gratitude for providing me with various opportunities during my PhD, including attendance at international conferences where I presented my work and explored collaborations with a variety of groups from around the world independently and confidently.

I would like to express my appreciation to **Jouf University** in Saudi Arabia for their financial support of my PhD studies.

I would like to thank all my collaborators; Prof. **Yara Gobato** (Federal University of São Carlos, Brazil) for Raman characterization and for useful discussions, Dr. **Jorlandio F. Felix** (University of Brasilia, Brazil) for exposing my samples to Gamma radiation, Prof. **Igor Kazakov** (Lebedev Physical Institute, Moscow, Russia) for providing me with samples investigated in this thesis, and Dr. **Helder Galeti** (Federal University of São Carlos, Brazil) for his helpful support to learn PL technique; and all other collaborators named in the publications list.

I am also grateful to Mr **Jasbinder Chauhan** and Dr. **Natalia Alexeeva** for their help in processing the devices investigated in this thesis. Also I would like to express my gratitude to all my colleagues in the School of Physics and Astronomy for their support and friendship during my PhD studies.

I would like to thank all my friends and family, specially, my father, **Saleh**, and my mother, **Maqbulah** for providing me infinite support, not only during my PhD studies but throughout my life.

Finally, I would like to express my gratitude to my beloved wife, **Rana**, and to my dear daughter, **Rateel**, for patience and understanding throughout my research. Without the love and care I was given, I would not have the ability to succeed. I cannot thank you enough for always believing in my ability to succeed and encouraging me along the road.

TABLE OF CONTENTS

CHAPTER 1: INTRODUCTION

1.1 INTRODUCTION

After the invention of the transistor in 1947, which was made for the first time from the elemental semiconductor polycrystalline germanium (Ge), a revolution in semiconductor materials industry followed in a large scale. For over a decade, Ge was regarded as the most practical technological material. In the late 1950s, research on the purification of silicon (Si) produced material appropriate for semiconductor devices, and new silicon-based devices began to be produced around 1960 [1]. However, its applicability is limited for electrical devices operating at high temperatures and high frequencies, and for light emitting optoelectronic devices in the visible range [2], due to the nature of its small bandgap and low carrier mobility. Gallium arsenide (GaAs), a III-V compound semiconductor, was considered as a potential candidate in semiconductor industry due to its versatile properties such as band gap, its capability to emit light effectively and operate at high frequencies. One of the most interesting properties of GaAs is that the formation of ternary compound (e.g. $GaAs_{1-x}Bi_x$) allows tailoring the bandgap. Indeed, the set of III-V compound semiconductors and their ternary (e.g. $GaAs_{1-x}Bi_x$) or quaternary (e.g. $Ga_xIn_{1-x}A_{1-y}N_y$) alloys deliver a wide range of band gap energies, which is particularly important when a specific band gap energy is necessary. These properties lead to applications of III-V semiconductors in photonic devices such as laser diodes, optical detectors, and solar cells. Furthermore, the importance of III-V compounds semiconductors has expanded since the introduction of non-equilibrium growth techniques such as Molecular Beam Epitaxy (MBE) in the early 1980s. MBE, which is now widely used in the manufacture of semiconductor devices, has several important capabilities including the formation of atomically flat and abrupt heterointerfaces and the growth of high-purity epitaxial thin-film semiconductors. Fig. 1.1 shows the bandgap energy of the most common semiconductors materials as a function of their lattice constants.

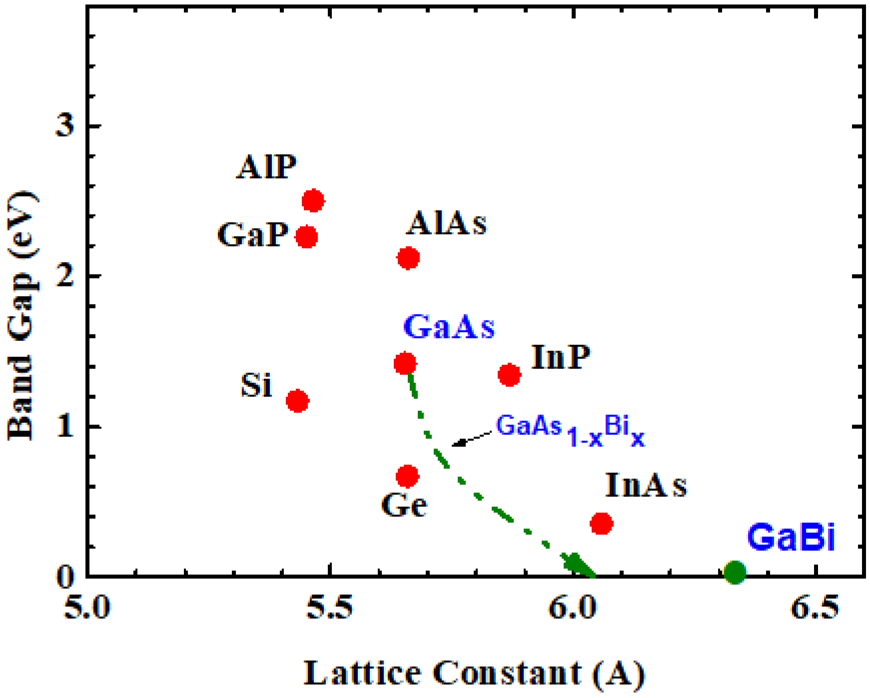

Fig. 1.1: Bandgap as a function of lattice constant of various III-V compound semiconductors materials. The dashed line represents the effect of adding Bi into GaAs.

Another property of GaAs is that the bandgap energy of this material can be tuned by introducing a small fraction of bismuth. This leads to the formation of dilute bismide GaAsBi.

Bismuth is the heaviest element in Group V of the periodic table, and generally it has not been used in device fabrication. Incorporating a small amount of Bi into GaAs reduces its band gap significantly without causing much lattice mismatch strain, making the materials suitable for multi-junction solar cells [3], photonic devices [4] and in long-wavelength optoelectronic devices [5], where a large mismatch between the epitaxial layers and substrate leads to the formation of dislocations in the layers. However, to grow such $GaAs_{1-x}Bi_x$ alloys, special growth conditions are required, including a very low substrate temperature and an As/Ga flux ratio near stoichiometric ratio [6] . Therfore, the creation of deep level defects due to those non-standard growth conditions is a major concern.

Additionally, the growth of epitaxial layers on GaAs substrate with different orientation than the conventional plane direction (100) has generated a wealth of information on the growth mechanisms of epitaxial layers. In fact, the use of non-conventional substrates for the growth of epitaxial semiconductor alloys has a major effect on their properties. In particular, the structural, optical and electrical properties of III-V compound semiconductor strutures are found to change and/or improve by growing the alloys on non-(100) planes. Indeed, semiconductors grown on high index substrates (n11) exhibit unique properties not found in identical structures formed on (100) oriented substrates, such as optical anisotropy [7], high hole mobility [8], and improved optical efficiency [9]. Moreover, although most reports of $GaAs_{1-x}Bi_x$ thin films and devices have been carried out on standard (100) GaAs substrates, there have been few studies on growth on high-index planes, which can have a significant impact on Bi incorporation as well as structural, electrical, and optical properties [10-14].

Furthermore, semiconductor materials are known for their susceptibility to defects, whether they are native due to crystal imperfections or due to foreign impurities induced during incorporation. Therefore, one of the interesting technologically useful features of semiconductors is the possibility to change their electronic and photonic properties by introducing small amounts of impurities in their crystal strutures. This process is known as doping. Defects introduce deep levels in the bandgap of semiconductors and have detrimental effects on the performance of the devices since they act as efficient recombination centres. Consequently, several research efforts have been directed towards understanding, improving and controlling the perfection of semiconductor crystals. Deep level transient spectroscopy (DLTS) is one of the most effective techniques used for characterising and identifying deep levels defects. Additionally, photoluminescence and Raman methods are routinely used to investigate the optical properties of semiconductor alloys.

The study presented in this thesis relates to the characterization of semiconductor alloys based on III-V semiconductors, namely GaAsBi grown by MBE on both (100) and (311)B GaAs substrates using strutural, optical and electrical methods.

1.2 MOTIVATION

Deep defects states in semiconductors materials play an essential role in the electrical and optical properties of III-V semiconductors, as well as in the performance of electronic and optoelectronic devices. Therefore, the main motivation of this thesis is to study the defects present in doped n-type and p-type GaAsBi epilayer devices grown by MBE.

Current-Voltage (I-V), Capacitance-Voltage (C-V), conventional DLTS, Laplace DLTS, X-ray diffraction (XRD), Raman and Photoluminescence characterisation techniques are employed to study the strutural, optical and electrical properties of n-GaAsBi layers grown on (100) and (311)B GaAs substrates. The motivation is to investigate the effect of substrate orientation on the Bi incorporation in n- and p-type doped GaAsBi because most studies focussed mainly on undoped GaAsBi. It is important to mention that the growth of epitixal layers on high index planes represent a step ahead in materials engineering, as it allows an additional degree of freedom in the development of advanced devices with enhanced properties than those fabricated on conventional (100) plane. Additionally, I-V, C-V, conventional DLTS, Laplace DLTS and PL are used to investigate the effect gamma radiation on the electrical and optical properties of dilute n-$GaAs_{1-x}Bi_x$ grown on (100) GaAs substrates. Moreover, XRD, Raman and PL are employed to examine the structural and optical properties of n-type and p-type $GaAs_{1-X}Bi_X$ thin films grown by MBE on (311)B GaAs substrates.

1.3 SCHEME OF THE THESIS

The struture of this thesis is organised as follows:

Chapter 1: discusses the research motivations and structure of the thesis.

Chapter 2: presents the fundamental concepts of semiconductors, crystal structure, energy band gaps, the principles of heterostructure devices. This chapter also covers the properties of GaAs and GaAsBi materials, as well describes the optical properties of semiconductors.

Chapter 3: provides details on the crystal defects as well as the theoretical background of carrier kinetics. The most well known defects in GaAs and dilute Bismuth materials are also discussed.

Chapter 4: describes the experimental techniques used in this thesis including DLTS, Laplace DLTS and PL. Furthermore, the hardware and software needed for implementing these methods are also discussed.

Chapter 5: provides information on the samples studied in this thesis, as well as gives a brief description of the measurements set up.

Chapter 6: discusses the effect of substrate orientation on the structural, electrical and optical properties of n-type $GaAs_{1-X}Bi_X$ layers grown by MBE using XRD, I-V, C-V, DLTS, Laplace DLTS, Raman and PL measurements.

Chapter 7: presents the effect of gamma radiation on the electrical and optical properties of dilute $GaAs_{1-X}Bi_X$ grown by MBE.

Chapter 8: describes the structural and optical properties of n-type and p-type $GaAs_{1-X}Bi_X$ thin films grown by MBE on (311)B GaAs substrates.

Chapter 9: presents an overview of the research work done in this thesis and provides suggestions for future work.

REFERENCES

[1] Donald A. Neamen, *Semiconductor Physics and Semiconductor Devices*. (McGraw-hill, 2012).

[2] D. B. Holt and B. G. Yacobi, *Extended defects in semiconductors: electronic properties, device effects and structures*. (Cambrige University press, 2007).

[3] Z. Zhou, D.F. Mendes, R.D. Richards, F. Bastiman, J.P. David, *Absorption properties of GaAsBi based p–i–n heterojunction diodes*, Semicond. Sci. Technol. **30**, 094004 (2015).

[4] S. Francoeur, M.-J. Seong, A. Mascarenhas, S. Tixier, M. Adamcyk, T. Tiedje, *Band gap of GaAs1−xBix, 0<x<3.6%*, Appl. Phys. Lett. **82**, 3874 (2003).

[5] V. Pačebutas, K. Bertulis, G. Aleksejenko, A. Krotkus, *Molecular-beam-epitaxy grown GaBiAs for terahertz optoelectronic applications*, J. Mater. Sci. Mater. Electron. **20**, 363 (2009).

[6] S. Tixier, M. Adamcyk, T. Tiedje, S. Francoeur, A. Mascarenhas, P. Wei, F. Schiettekatte, *Molecular beam epitaxy growth of GaAs1−xBix*, Appl. Phys. Lett. **82,** 2245 (2003).

[7] R. Notzel, N.N. Ledentsov, L. Daweritz, K. Ploog, M. Hohenstein, *Semiconductor quantum-wire structures directly grown on high-index surfaces*, Phys. Rev. B. **45,** 3507 (1992).

[8] Davies, A. G., J. E. F. Frost, D. A. Ritchie, D. C. Peacock, R. Newbury, E. H. Linfield, M. Pepper, and G. A. C. Jones, *The growth and physics of high*

mobility two-dimensional hole gases, J. Cryst. Growth. **111,** 318 (1991).

[9] M. Henini, A. Polimeni, A. Patanè, L. Eaves, P.C. Main, G. Hill, *Effect of the substrate orientation on the self-organisation of (InGa)As/GaAs quantum dots*, Microelectronics J. **30,** 319 (1999).

[10] M. Henini, J. Ibáñez, M. Schmidbauer, M. Shafi, S. V. Novikov, L. Turyanska, S.I. Molina, D.L. Sales, M.F. Chisholm, J. Misiewicz, *Molecular beam epitaxy of GaBiAs on (311) B GaAs substrates*, Appl. Phys. Lett. **91**, 350 (2007).

[11] J.F. Rodrigo, D.L. Sales, M. Shafi, M. Henini, L. Turyanska, S. Novikov, S.I. Molina, *Effect of annealing on the structural and optical properties of (3 1 1)B GaAsBi layers*, Appl. Surf. Sci. **256**, 5688 (2010).

[12] P.K. Patil, F. Ishikawa, S. Shimomura, *GaAsBi/GaAs MQWs MBE growth on (411) GaAs substrate*, Superlattices Microstruct. **100**, 1205 (2016).

[13] G.A. Prando, V. Orsi Gordo, J. Puustinen, J. Hilska, H.M. Alghamdi, G. Som, M. Gunes, M. Akyol, S. Souto, A.D. Rodrigues, H.V.A. Galeti, M. Henini, Y.G. Gobato, M. Guina, *Exciton localization and structural disorder of GaAs1-xBix/GaAs quantum wells grown by molecular beam epitaxy on (311)B GaAs substrates*, Semicond. Sci. Technol. **33**, 084002 (2018).

[14] H. Alghamdi, V.O. Gordo, M. Schmidbauer, J.F. Felix, S. Alhassan, A. Alhassni, G.A. Prando, H. Coelho-Júnior, M. Gunes, H.V.A. Galeti, Y.G. Gobato, M. Henini, *Effect of thermal annealing on the optical and structural properties of (311)B and (001) GaAsBi/GaAs single quantum wells grown by MBE*, J. Appl. Phys. **127,** 125704 (2020).

CHAPTER 2: FUNDAMENTAL CONCEPTS OF SEMICONDUCTORS

This chapter describes some basic concepts of semiconductor materials such as doping type by the addition of impurity atoms into the host lattice, different structures and orientations of the crystals, energy band gaps and density of states. Heterostructures and their properties including lattice mismatch and band alignment are also discussed. In addition, the electrical and optical properties of semiconductors in general and III-V materials in particular will be highlighted. The properties of selected compounds such as GaAs and GaAsBi are given including the role of bismuth impurity in the modification of the bandgap of GaAs.

2.1. SEMICONDUCTORS

Semiconductors can be defined as materials that have an electrical conductivity value between that of a conductor (e.g., metals) and insulators (e.g., ceramics). The resistivity of semiconductors ranges from $\sim 10^{-2}$ to $\sim 10^{9}$ Ω-cm.

Semiconductors, which are essential in the development of various electronic and optical devices, can be found in computers, mobile phones, light emitting diodes, lasers, solar cells and optical fiber telecommunication systems [1] .

There are two families of semiconductor materials, namely elemental and compound semiconductors. Elemental semiconductors involve a single element, such as silicon (Si) and germanium (Ge) which belong to the group IV of the periodic chemical table.

Compound semiconductors that are made from a combination of elements in the periodic table are labelled as compound semiconductors. Semiconductors with two and three elements are known as binary (e.g. GaAs and GaP) and ternary (e.g. InGaAs, GaAsBi) compounds, respectively [2].

2.1.1 DOPED AND UNDOPED SEMICONDUCTORS

Undoped semiconductors, which are also referred to as intrinsic or pure semiconductors, do not contain a significant amount of impurities that can alter their electrical and optical properties. In intrinsic semiconductors, the number of electrons in the conduction band is equal to the number of holes in the valence band. Since the valence band is fully filled with electrons and the conduction band is fully empty, then these semiconductors behave as insulators at low temperatures (0 Kelvin) because there is no flow of charge carrier to contribute to their conductivity.

Doped semiconductors, known as extrinsic semiconductors, have impurities (called dopants) incorporated into their host lattice in order to change their electrical properties. The type of electrical conductivity, namely n-type and p-type, depends on the dopant atoms since their incorporation changes the concentration of electrons and holes at thermal equilibrium. The dominant charge carrier concentration in n-type and p-type semiconductors are electrons and holes (deficiency of electrons), respectively. For example if arsenic (As: group V) and boron (B: group III) are incorporated in Si (group IV element), n-type and p-type conductivities can be achieved, respectively. The As and B atoms, in this case, are known as donor and acceptor dopants [2,3], respectively. For As and B doped silicon an excess of electrons and holes is achieved, respectively. Similarly, if Si and Be atoms are incorporated substitutionally into GaAs host lattice, n-type and p-type conductivities can be achieved, respectively.

2.2. CRYSTAL STRUCTURE AND PROPERTIES

The performance of semiconductor devices is influenced by the crystal structure, which is determined by the atoms' arrangement in the crystals. A crystal structure formation occurs when atoms or molecules are placed in an arrangement, which forms a three-dimensional periodic array structure without any impurities added in the course of the process of developing the structure. The performance of a semiconductor is very dependent on the crystalline structure. The smallest set of atoms or molecules that can be replicated to form a crystalline structure is the unit cell. Crystal structures can be found in different forms. For example, a simple cube where all corners contain atoms, a body centred cube (bcc) where there is an atom at the center of the cube, and a face centred cube (fcc) where the atoms are located on each face of the cube. These models represent the unit cell [4]. Fig. 2.1 describes the simple cube (a), body-centered cube (b), and face-centered cube (c), respectively [2].

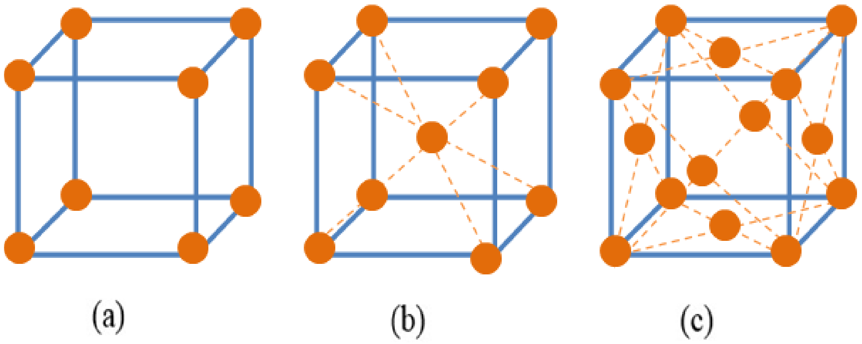

Fig. 2. 1: Crystal structure (a) simple cubic, (b) body-centred cubic and (c) faced-centred cubic.

The crystal structuring in semiconductors can be classified into several types of structures. Examples of these structures are zinc blende structure (e.g. GaAs, GaSb and InAs), and diamond structure, which has one type of element atoms (e.g. Ge, Si and C). In addition, both structures can be made by interpenetration of two fcc lattices, one of which is one-quarter of the distance along the body diagonal. The atoms are grouped as a tetrahedron in both forms, and each atom is covalently connected to four neighbouring atoms. The two structures are very important in the semiconductor industry. Fig. 2.2 shows a diamond structure and a zinc blende structure of some important semiconductors, namely Si and GaAs.

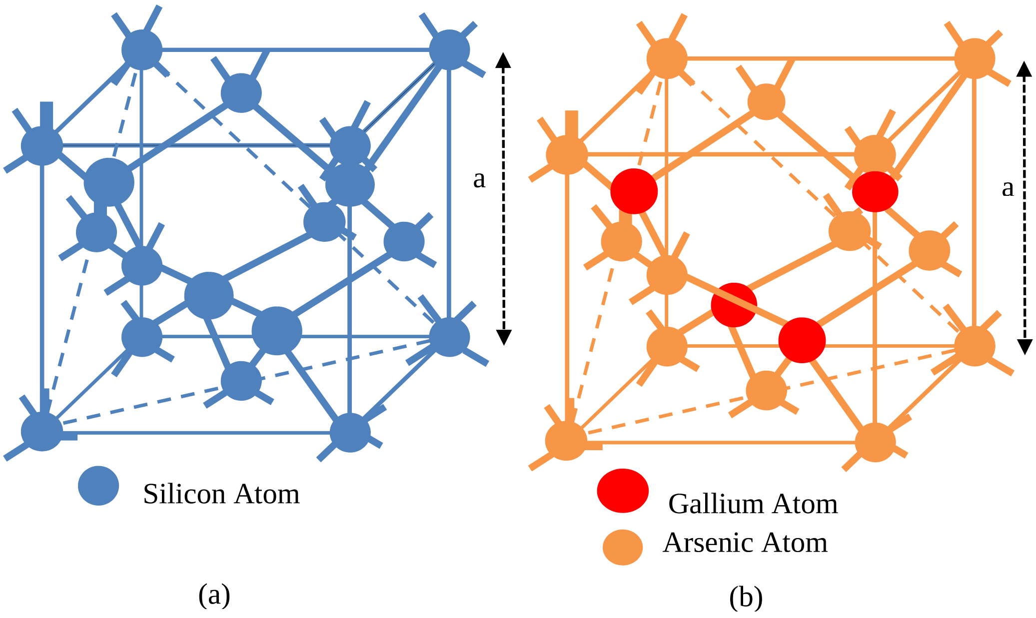

(a)

(b)

Fig. 2. 2: (a) diamond structure for Si. (b) Zincblende structure for GaAs [2].

The orientation of crystal planes is also important as they are crucial in the fabrication of semiconductor devices. Hence, to define the crystal planes, Miller indices are commonly used. Miller indices of a plane can be identified by the intercepts of a plane along with the x, y and z directions, then take reciprocals of the intercepts and ultimately reducing them to the smallest integers [5]. A crystal surface is determined by a set of h, k and l as follows:

I) Direction of (*hkl*) for a plane that has intercepts at 1/*h*, 1/*k* and 1/*l* on the x, y and z axis, respectively.

II) $(\bar{h}kl)$ for a plane that intercepts the negative x axis.

III) $\{hkl\}$ for a collection/set of planes.

IV) [*hkl*] for crystal directions e.g. [100] for the x axis.

V) <*hkl*> for a full set of directions.

Fig. 2. 3 shows some planes in Miller indices cubic crystal.

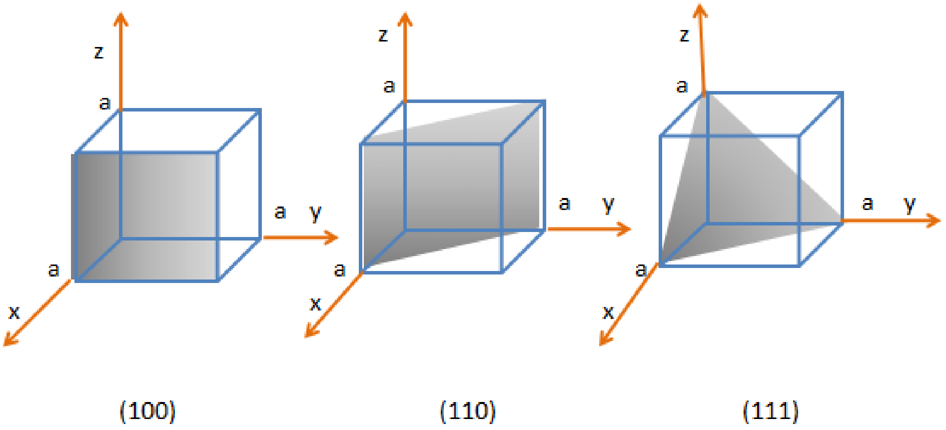

Fig. 2. 3: Miller indices of some planes in a cubic crystal.

The crystalline structure will be the same under any relocation through a direct lattice vector (**R**) which is the sum of primitive vectors (**a**, **b**, **c**) as follows:

$$\boldsymbol{R} = m\boldsymbol{a} + n\boldsymbol{b} + p\boldsymbol{c} \tag{2.1}$$

where m, n and p are integers.

Primitive basis vectors can define the reciprocal basis vectors (**b***, **c*** and **d***) which are given by:

$$\boldsymbol{a}^* = 2\pi \frac{\boldsymbol{b} \times \boldsymbol{c}}{\boldsymbol{a} \cdot \boldsymbol{b} \times \boldsymbol{c}} \tag{2.2}$$

$$\boldsymbol{b}^* = 2\pi \frac{\boldsymbol{c} \times \boldsymbol{a}}{\boldsymbol{a} \cdot \boldsymbol{b} \times \boldsymbol{c}} \tag{2.3}$$

$$\boldsymbol{c}^* = 2\pi \frac{\boldsymbol{a} \times \boldsymbol{b}}{\boldsymbol{a} \cdot \boldsymbol{b} \times \boldsymbol{c}} \tag{2.4}$$

where $\boldsymbol{a} \cdot \boldsymbol{a}^* = 2\pi$, $\boldsymbol{a} \cdot \boldsymbol{b}^* = 0$, and so on.

It can noted that the denominators are identical because $\boldsymbol{a} \cdot \boldsymbol{b} \times \boldsymbol{c} = \boldsymbol{b} \cdot \boldsymbol{c} \times \boldsymbol{a} = \boldsymbol{c} \cdot \boldsymbol{a} \times \boldsymbol{b}$ and they define the volume enclosed by the vectors (**a**, **b** and **c**) with the general reciprocal lattice vector (**G**) given by:

$$\boldsymbol{G} = h\boldsymbol{a}^* + k\boldsymbol{a}^* + l\boldsymbol{a}^* \tag{2.5}$$

where *h*, *k* and *l* are integers.

The relationship between the direct lattice vector (**R**) and the reciprocal vector (**G**) is given by [5].

$$\mathbf{G}.\mathbf{R} = 2\pi \text{ x integer.} \tag{2.6}$$

It is worth pointing out that the planes of the crystal are classified as high and low depending on the orientation of the plane. The planes such as (100), (110) and (111) are called low index planes. While high index planes have an index higher than zero and one e.g. (311)A/B.

2.3. ENERGY BAND GAPS

Insulators, semiconductors, and metals are the three categories of materials classified in solid state physics. The size of the energy bandgap (E_g), which is the difference between the energy of the highest valence band (VB) and the energy of the lowest conduction band (CB), determines this classification. In particular, the energy bandgap for a III-V semiconductor ranges from ~ 0.17 eV (InSb) to ~ 6 eV (AlN) [3]. The energy-wave vector (E-k) relationship is commonly used to represent the band gap of a semiconductor, as shown in Fig. 2.4. In direct bandgap, when k=0, the conduction band minima and valence band maxima have roughly parabolic forms, and their energy is given by:

$$E_C = E_g + \frac{h^2 {k_B}^2}{8\pi^2 m_e^*} \ , E_v = E_g - \frac{h^2 {k_B}^2}{8\pi^2 m_h^*} \qquad (2.7)$$

where h is the Planck's constant, k_B is Boltzmann constant, m_e^* and m_h^* are the effective mass of electron and hole, respectively. E_c and E_v are the energy of conduction and valence bands, respectively

The electrons in the valence band do not have enough energy to be excited to the conduction band at very low temperatures (~ 0 K), thus they are confined in the valence band. As a result, at this low temperature, an intrinsic semiconductor behaves as an insulator [6].

2.3.1. DIRECT AND INDIRECT ENERGY BANDGAPS

The energy bandgap of a semiconductor can either be direct or indirect. This depends on two factors which are the position of the lowest energy of the conduction band and the highest energy of the valence band with respect to the wave vector (k). If the minimum of the conduction and the maximum of the valence band occur at the same k value, i.e. k= 0 then the semiconductor has direct bandgap. An example of a direct energy bandgap is GaAs, otherwise the semiconductor is an indirect bandgap. An example of an indirect bandgap is silicon.

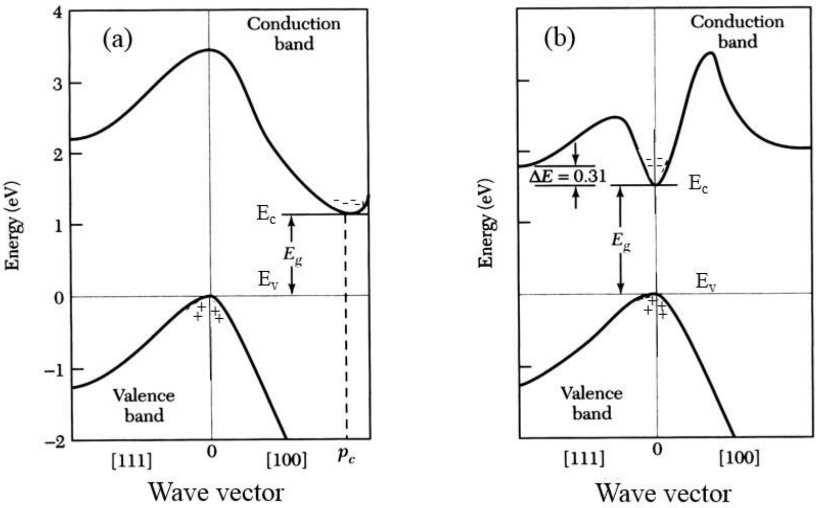

Fig. 2. 4: Energy-band structures of (a) Si has an indirect band gap (b) GaAs has a direct band gap [2].

2.3.2.TEMPERATURE DEPENDENT ENERGY BANDGAPS

The properties of semiconductors are temperature dependent. For example, as the temperature increases the band gap energy decreases. At zero Kelvin (0 K), the bandgap energy of GaAs and Si are 1.52 eV and 1.17 eV, respectively. However, at room temperature, the bandgap decreases to 1.42 eV and 1.12 eV for GaAs and Si, respectively [5]. The reduction of the band gap energy was attributed to the dilation of the lattice constant to be the primary cause. As thermal power is applied to a semiconductor, the inter-atomic spacing increases as the thermal vibration of the atoms increases, resulting in a drop in the potential observed by electrons and hence a reduction in the bandgap occurs. Another contributor to temperature influence on semiconductors energy bandgaps is the electron lattice interaction (electron – phonon) [7]. Varshni [8] proposed an empirical relationship for the temperature dependence of the energy band gap $E_g(T)$, which is given by:

$$E_g(T) = E_g(0) - \frac{\alpha T^2}{T+\beta} \tag{2.8}$$

where $E_g(0)$ is the energy of the bandgap at 0 K, α and β are constants and represent empirical parameters related to the material e.g. $\alpha = 0.49$ meV/K and $\beta = 655$ K , $\alpha = 0.5\,\mathrm{meV/K}$ and $\beta = 220$ K for Si [5] and GaAs [9], respectively.

2.4. DENSITY OF STATES

Distribution of carriers and their concentration in a semiconductor are vital in determining the number of electronic states at a certain energy level that available for carriers to occupy. The density of states N(E) is given by the number of states in a unit volume across a single unit energy that are available per carrier occupation. The interaction between atoms due to the close space between them cause the quantified energy levels to split into a finite number of energy states [10] .

As atoms interact there are high probabilities of breaking the energy levels into a number of energy states. Since the electrons tend to settle in the lowest energy levels available, the highest two occupied energy bands can be identified as the conduction and valence bands. The two bands are separated by a bandgap, a range of energy levels where no states exist. At the lowest temperature (e.g. 0 K), the valence band is totally filled with electrons, while the conduction band electronic states are empty. However, electrons in the valence band can be excited to the conduction band if they gain enough energy to overcome the bandgap. As a result of this process, a hole is formed in the valence band due to the formation of a local positive charge known as vacancies (holes). These electrons need accessible states in the conduction band for occupation. The allowed states at certain energy levels are defined as density states. The density of states is highly reliant on the confinement of carriers (e.g. electrons) and their degree of freedom which in turn depends on material structure. Semiconductors can be classified into four types according to their dimensions: 3D (three-dimension), 2D (two-dimension), 1D (one-dimension) and 0D (zero-dimension). The density states D(E) of 3D (bulk material), 2D (quantum well), and 1D (quantum wire) is $\sim E^{1/2}$, constant (independent of E but follows a step like function), and $\sim E^{-1/2}$, respectively. D(E) of 0D (quantum dot) material is represented by a delta function. Fig. 2.5 shows the density of states as a function of energy for these systems [5] .

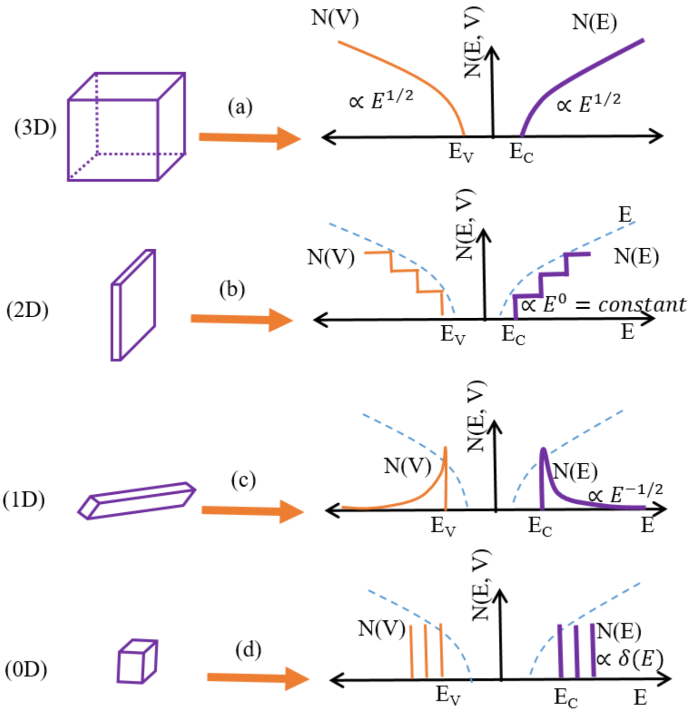

Fig. 2.5: Density of states for (a) bulk material (3D), (b) quantum well (2D), (c) quantum wire (1D) and (d) quantum dot (0D) [5].

2.5. HETEROJUNCTION STRUCTURES

Semiconductors can be categorized into homojunction and heterojunction structures. A homo-junction structure is formed when two layers of the same semiconductor materials are deposited on top of each other (e.g. p-n junction). These materials normally exhibit the same band gap with varied doping. However, when two different semiconductor materials are stacked, then the resulting structure is called a heterojunction. These materials differ in terms of lattice constants, energy bandgaps etc. [4].

2.5.1. LATTICE MISMATCH

A lattice-matched structure is one that is made up of two materials with the same lattice constants (Fig. 2.6 (a)). A lattice-mismatched structure, on the other hand, is formed when two materials with differing lattice constants are grown on top of each other. This mismatched structure has defects occurring at the interface due to strain and dislocations caused by lattice constants disparities. The lattice mismatch can be expressed as [5]:

$$\frac{\Delta a}{a} = \frac{a_{sub} - a_{layer}}{a_{sub}} \tag{2.9}$$

where a_{layer} is the lattice constant of the epitaxial layer and a_{sub} is the lattice constant of the substrate. Strain can either be compressive or tensile in a mismatched structure. When $a_{layer} > a_{sub}$ compressive strain occurs. However, when $a_{layer} < a_{sub}$ tensile strain is achieved. Fig. 2.6 shows a lattice matched and mismatched system.

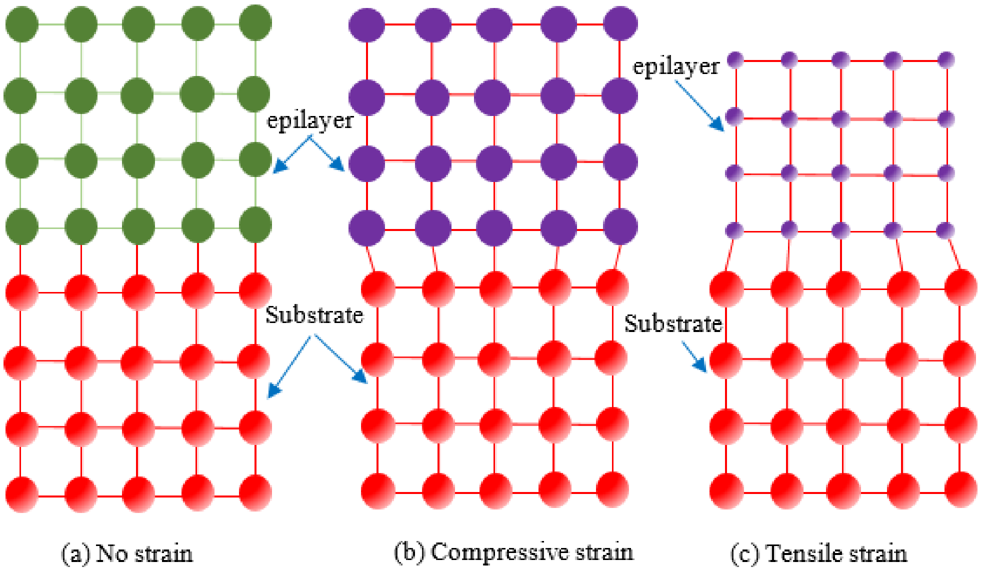

Fig.2.6: Schematic diagram showing (a) lattice matched system; (b) and (c) lattice mismatched system with compressive and tensile strain, respectively.

2.5.2. ATOMIC SIZE AND ELECTRONEGATIVITY

The size of the atoms in the two different semiconductor materials that make up a heterojunction is an important factor in the growth process of heterojunction structures, in addition to lattice matching. The discrepancy in atom size can also create strain in the structure. Indeed, since strain has been proven to have a significant impact on the properties of a heterostructure [11] , the size of atoms that form a heterojunction is important in the development of heterojunction structures.

The characteristic of atoms and molecules to attract electrons to themselves and form chemical bonds is termed electronegativity (χ). χ was first introduced by Linus Pauling [12] and is also referred to as Pauling's electronegativity scale. χ ,which is a unitless quantity, plays an important role during the growth process [5]. The electronegativity scale, which gives the difference between two materials A and B that form a heterojunction, is given by:

$$\chi_A - \chi_B = [(eV)^{-\frac{1}{2}}]\sqrt{E_D(AB) - \frac{[E_D(AA)+E_D(BB)]}{2}} \qquad (2.10)$$

where χ_A and χ_B are the electronegativity of material A and B, respectively. $E_D(AB)$, $E_D(AA)$ and $E_D(BB)$ are the dissociation energies in eV between the atoms AB, AA as well as BB, respectively. The factor $\left[(eV)^{\frac{-1}{2}}\right]$ is used to make the value of electronegativity unitless.

2.5.3. BAND ALIGNMENT

The alignment of the energy bands between two semiconductor materials play a major role in the operation of heterojunction devices. A model to construct the energy band diagram of semiconductor heterostructures was proposed by Anderson in 1962 [13]. Band alignment is particularly important in the transport of charge carriers. Anderson's theory is based on the electron affinity of the materials that make up the heterojunction. Anderson's rule states that if two semiconductors (A and B) are utilised to construct a heterojunction, their vacuum levels must be aligned. As a result, the difference in the electron affinities of A and B ($\kappa_A - \kappa_B$) leads to the offset of both the conduction band (ΔE_c) and valence band (ΔE_v) as expressed below [10]:

$$\kappa_B - \Delta E_c - \kappa_A = 0 \qquad (2.11)$$

$$\Delta E_c = \kappa_B - \kappa_A \text{ and } \Delta E_v = \Delta E_g - \Delta\kappa \qquad (2.12)$$

Heterojunction structures are classified into three categories based on their band alignment (i.e. type I, II and III). Type I heterojunctions also referred to as straddling are formed when the bandgap of semiconductor A is larger than that of semiconductor B. GaAs/InP and AlGaAs/GaAs structures are two common examples of such alignment. Type II heterojunctions, also known as staggered heterojunction, are formed when both the valence band edge and conduction band edge of semiconductor A are lower than the corresponding valence and conduction band edges of semiconductor B. InAIAs/InP is one of such example of type II alignment. Type III heterojunctions, labelled as misaligned type II or broken-gap, is formed when the conduction band of one type of material lies below the valence band of the other type of material as in the case of GaSb/InAs [10]. Fig. 2.7 shows a schematic diagram of type I, II and III heterojunctions [5].

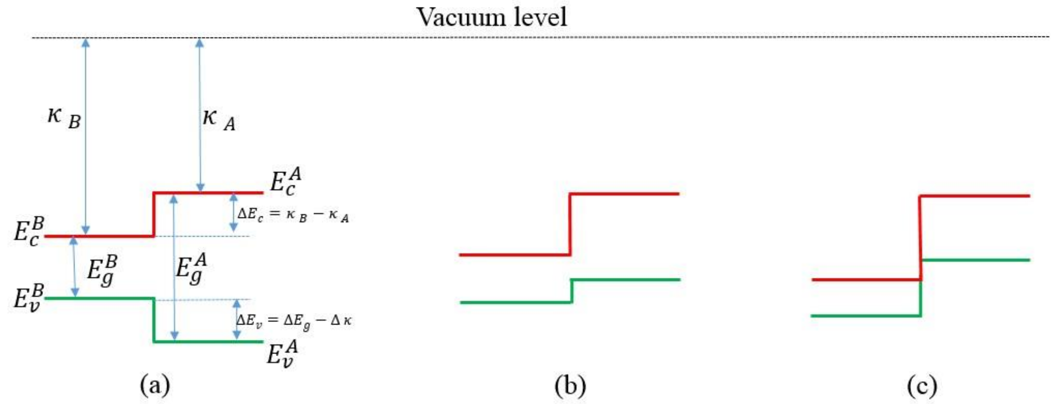

Fig. 2.7: band alignment of (a) type I (straddling), (b) type II (staggered) and (c) type III (broken-gap) heterojunctions [5].

2.6. GENERAL PROPERTIES OF SELECTED SEMICONDUCTORS

In this section some of the important properties of the semiconductors investigated in this thesis will be reviewed, namely gallium arsenide (GaAs) and dilute bismide (GaAsBi).

2.6.1. GALLIUM ARSENIDE

Gallium arsenide (GaAs) was first produced in 1920 by Goldschmidt, and its properties later studied in 1952 [14]. It is one of the most explored compound semiconductor material in the technological arena. GaAs has a face centred cubic lattice (fcc) made up of Ga (Group III) and As (Group V) atoms from the periodic table. As shown in Fig. 2.2 (b), GaAs possesses a zincblende structure of As with Ga atoms positioned on the body diagonals at the coordinates $\left(\frac{a}{4}, \frac{a}{4}, \frac{a}{4}\right)$, where a is the GaAs lattice constant given by [14]:

$$a = 0.565325+3.88\text{x}10^{-6}\ (T- 300K)\ \text{nm} \qquad (2.13)$$

where T is the temperature in Kelvin.

Fig. 2.8 illustrates the energy band structure of GaAs. It can clearly be seen that the conduction band minima and the valence band maxima lie at the same value of wave vector at k = 0. As a result, the transition of electrons from the valence band to the conduction band need a change in energy but without a change in momentum as it is conserved. Hence, the GaAs bandgap is referred to as direct. This is an important property for devices used in optoelectronics applications.

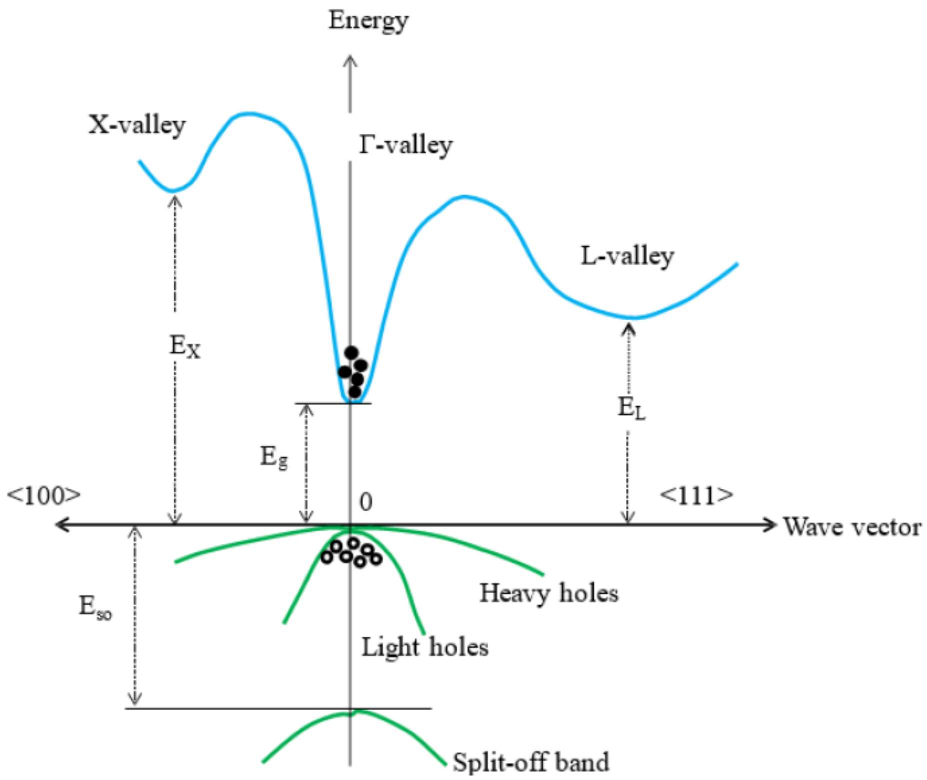

Fig. 2.8: Energy bandgap diagram of GaAs showing three different conduction valleys (X, Γ and L).

GaAs has higher electron mobility than Si. This makes it ideal for devices operating at high frequencies. In addition, the bandgap energy of GaAs (1.42eV) at room temperature is higher than Si (1.12 eV), making GaAs devices more suitable for operations at high temperatures [15]. GaAs is also used as a semi-insulating substrate in integrated circuits because it has a very high resistivity (~ 10^8 Ω-cm) compared to Si (~ 6.4×10^2 Ω-cm). Moreover, optical fibre telecommunication requires lasers operating at specific wavelengths, namely 1.30µm and 1.55µm. Ternary and quaternary semiconductor alloys and different structures such as multiple quantum wells (MQWs) and quantum dots (QDs) have been used to achieve these emissions [16–18] which are not accessible by the use of Si-based structures and devices. Table 2. 1 summarizes some important properties of GaAs.

Table 2. 1: Selected GaAs parameters where m_0 is the free electron rest mass.

Parameter	**GaAs**
Crystal Structure	Zincblende
Lattice constant (nm)	0.5653
Crystal density (g/cm^3)	5.360
Energy band gap (eV) (300K)	1.42
Bandgap type	Direct
Electron effective mass	$0.063m_0$
Hole effective mass	$0.62m_0$ (h_h), $0.087m_0$(l_h)
Dielectric constant (static)	12.85
Specific heat(cal/gK)	0.08
Electron affinity (eV)	4.07

2.6.2. DILUTE BISMIDE MATERIALS

Dilute bismide semiconductors alloys, particularly $GaAs_{1-x}Bi_x$ are promising candidates for long wavelength optoelectronics devices [19], infrared emitters, detector and spintronic related devices [20–22]. The following are some of its well-known properties which make it very attractive to users in devices applications. $GaAs_{1-x}Bi_x$ materials have optical and electrical properties that distinguish it from other materials. For instance, the incorporation of small amounts of Bi atoms into the GaAs host lattice can dramatically affect the bandgap energy of GaAs [22]. For instance, the bandgap of GaAs is reduced by ~88 meV per % Bi, and the spin–orbit (SO) splitting energy (Δ_{so}) is increased significantly. It is worth pointing out that if the splitting is greater than the band gap ($\Delta_{so} > E_g$), the Auger recombination process which involves the split off band is suppressed [21,23]. Because of these unusual properties, such alloys are promising materials for making GaAsBi-based structures suitable for both optoelectronic and spintronic applications [22,24].

The first effective incorporation of Bi into GaAs was achieved using metalorganic vapour phase epitaxy (MOVPE) [25] and molecular beam epitaxy (MBE) techniques [26,27]. Bi atom is the heaviest of the group V elements. The atomic radius of Bi atom is much larger than that of As atom, and it has a lower electronegativity. Because of the significant size difference between Bi and As atoms, a compressive strain develops surrounding the atoms.

The huge variation of atomic potential energy induced in the GaAsBi band structure creates a localized state level near the GaAs valence band maxima, attracting holes from the valence band. The localised potential energy of Bi atoms and the surrounding lattice relaxation significantly disturb the GaAs electronic band structure, resulting in a variety of qualitative effects comparable to those seen in the dilute nitride GaAsN material system. While energy states arise at the valence band maxima in GaAsBi materials, in GaAsN energy states appear near the conduction band minima. It is worth noting that in dilute bismide/nitride GaAs, As atoms are substituted with Bi and N atoms. Further, as predicted by virtual crystal approximation (VCA), these localised energy states behave like isoelectronic impurities [22] and interact with the valence and conduction band of GaAsBi and GaAsN, respectively. The interaction between acceptor-like (GaAsBi) and valence band, and donor-like (GaAsN) and conduction band energy states causes the energy bands to bow significantly, resulting in a substantial reduction of the band gap of GaAs for a small amount of Bi and N. The large drop in GaAs bandgap due to Bi incorporation into the host lattice is thought to be related to the disruption of the valence band maximum (VBM) and 6p state of Bi atom [28]. In GaAs, the Bi 6p orbitals are expected to be close to VBM. As a result of this upward motion of heavy and light hole bands, the substantial band gap reduction occurs. In addition, the shift/change of the split-off band position results in a large increase of the spin-orbit splitting energy [21]. However, a resonant interaction between the conduction band minima and the 2s state of the N atom is thought to be responsible for the substantial decrease in the bandgap of GaAs when N substitutes As [29,30]. The band structures of GaAsBi and GaAsN alloys with respect to GaAs are shown schematically in Fig. 2.9. It is important to mention that arsenic (As) has a higher and lower electronegativity than Bi and N, respectively. This difference in electronegativity could explain the energetic behaviour of Bi and N isoelectronic impurities [31].

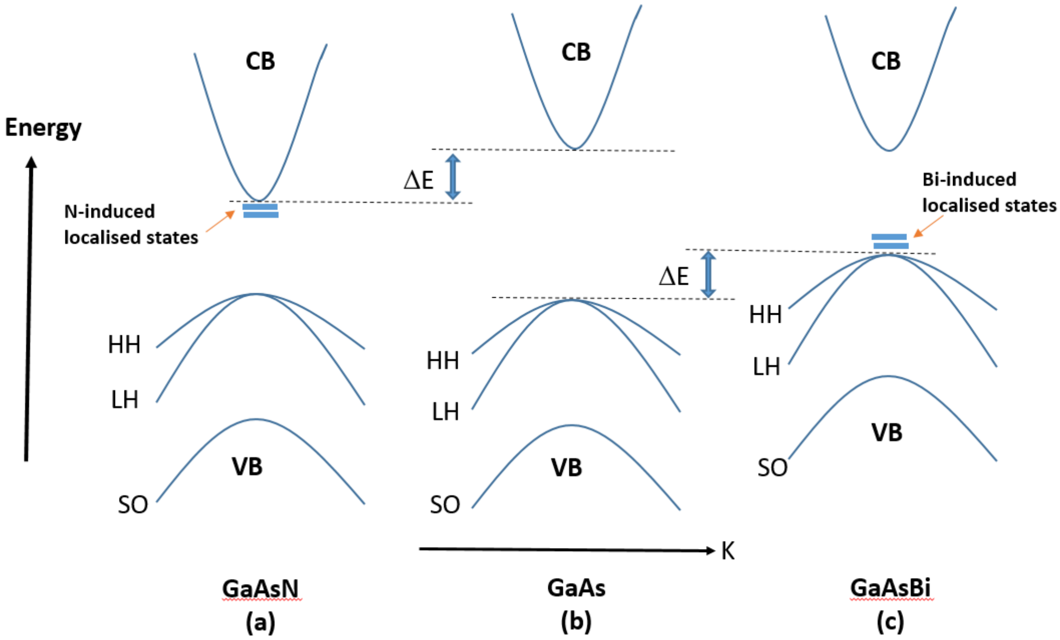

Fig. 2. 9: Band gap structure of (a) dilute GaAsN, (b) GaAs, and (c) dilute GaAsBi. CB, HH, LH and SO represent the conduction band, heavy holes, light holes, and split off bands, respectively. The position of localized energy states in Bi and N are shown by solid blue lines.

2.6.2.1 INCORPORATION OF BISMUTH ON HIGH INDEX GaAs PLANES

The substrate surface orientation plays a major role in the growth of III-V semiconductors. Layer formation on high Miller index surfaces, i.e. surfaces orientated differently than the conventional (100) orientation, provides a major degree of freedom in the epitaxy of III-V GaAs semiconductors. In fact, the incorporation of Bi into high index GaAs substrates grown by MBE was shown to be substantially higher in the (311)B epilayers than in the (100) orientation [32,33]. In addition, the growth of epitaxial layers on high index substrates, i.e. non-(100), can influence growth, impurity incorporation and electronic properties [33].

2.7. OPTICAL PROPERTIES OF SEMICONDUCTORS.

The incidence of a photon onto a semiconductor material's surface can follow a variety of optical processes, including reflection from the surface, transmission through the material, and absorption in the material. If the incident photons have enough energy, they can excite an electron from the valence band to the conduction band. As a result, the created electron-hole pair may interact with lattice vibrations and localised defects within the band gap. Hence, the optical response (i.e. optical spectra) of a semiconductor subjected to photons can provide useful information about the properties of semiconductor materials.

2.7.1. ABSORPTION PROCESS

The operation of optical semiconductor devices depends on the transition of electrons and holes between the energy levels. Generally, the illumination of a semiconductor material with a photon with energy hυ (the photon energy) is equal or greater than the band gap energy E_g (energy band gap) can generate an electron-hole pair. This process which is called absorption is illustrated in Fig. 2.10, where an electron is excited by a photon from the valence band to the conduction band leaving a hole in the valence band. Absorption also occurs when an electron makes a transition by absorbing a photon from the valence band to an empty impurity (neutral acceptor) or from an impurity atom (neutral donor) to the conduction band. An absorption transition can also occur between two impurity atoms. Furthermore, the fundamental absorption process is strongly affected by whether the energy gap is direct or indirect. In a direct semiconductor, e.g. GaAs, an electron at the valence band maximum can execute a vertical transition to the conduction band minimum directly without changing its wavevector (k). Energy is conserved according to the following equation:

$$\mathrm{h}\upsilon = E_f - E_i \tag{2.14}$$

where E_i is the initial state of energy in the lower band, E_f is the final state energy in the upper band. hυ is the photon energy. h is the Planck's constant, υ is the frequency.

For indirect band gap material, e.g. Si, the excited electron between the energy bands needs additional momentum to reach the conduction band. The electron gain this momentum by interacting with a phonon. In this case, the energy conservation is:

$$\mathrm{h}\upsilon = E_f - E_i \pm \mathrm{h}\Omega \tag{2.15}$$

where hΩ is the energy of the phonon.

The bulk semiconductors have a continuous series of energy states within lower and upper bands, hence the interband transitions are possible over a continuous range of frequencies. Moreover, the range of frequencies can be determined by the upper and lower energy limits of the bands. As a result, interband transitions give rise to continuous absorption spectrum from low energy levels at E_g to an upper energy level.

The absorption spectrum of a material is related to its band structure and in particular to the density of states for the transition.

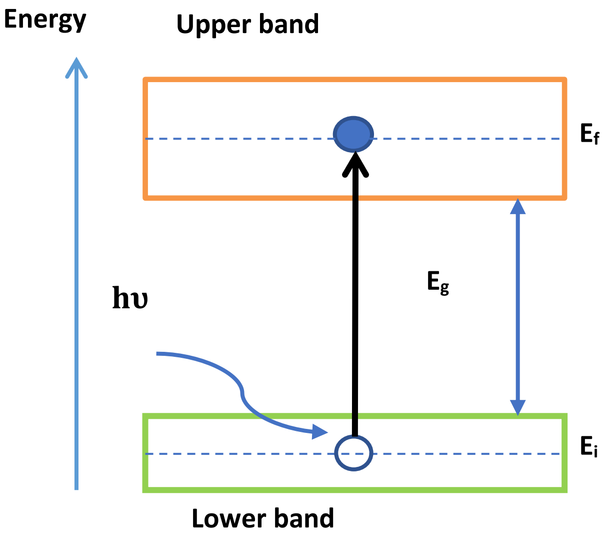

Fig. 2.10: The interband optical absorption between the initial energy states E_i in a lower band and a final state energy E_f in the upper band. E_g is the energy band gap. hυ is the photon energy.

The absorption coefficient (α) as a function of wavelength (λ) for a direct band gap semiconductor (e.g. GaAs), can be expressed as follows [34]:

$$\alpha(\lambda) = A(\mathrm{h\upsilon} - E_g)^{\frac{1}{2}} \tag{2.15}$$

where A is a constant and depends on the properties of the material, E_g is the band gap energy and hυ is the incident photon energy.

2.7.2. EMISSION PROCESS

In absorption process transitions, photon absorption creates an electron-hole pair. However, in emission transitions, an electron recombines with a hole resulting in the emission of a photon. The emission process involves transitions that are the inverse of the absorption process. Moreover, emission of photons occurs when an electron in a high energy state make a transition to a lower empty energy state by releasing energy as photons. The released energy in the form of electromagnetic radiation is defined as the difference between two energy levels. One of the important radiative transition is band to band transition. In this recombination transition a free electron from the conduction band and a hole from the valence band recombine radiatively with high probability, if the semiconductor has a direct band gap. However, for indirect bandgap, as in absorption, a phonon must be involved. It is worth mentioning that, the indirect process is less probable than direct recombination. For example, the probability for a radiative transition in silicon is very small, and the life time for an excited electron in indirect gap material is much longer compared to direct materials. This explains why indirect gap material like Silicon is a poor light emitter [34]

REFERENCES

[1] M. Grundmann, *The physics of semiconductors: An introduction including devices and nanophysics*. (springer, 2006).

[2] S.M. Sze, *Semiconductor devices: physics and technology*. (John Wiley & Sons, 2008).

[3] C. Kittel, *Introduction to Solid State Physics*. (Wiley Sons, 2004).

[4] Donald A. Neamen, S*emiconductor Physics and Semiconductor Devices: Basic Principles*. (McGraw-hill, 2012).

[5] S.M. Sze, K.K. Ng, *Physics of Semiconductor Devices*. (John Wiley & Sons, 2006).

[6] C.A. Colinge, J. P., & Colinge, *Physics of semiconductor devices*. (springer science & Business Media, 2005).

[7] G.B. Fang, Z. M., Ma, K. Y., Jaw, D. H., Cohen, R. M., Stringfellow, *Photoluminescence of InSb, InAs, and InAsSb grown by organometallic vapor phase epitaxy*, J. Appl. Phys. **67,** 7034 (1990).

[8] Y.P. Varshni, *Temperature dependence of the energy gap in semiconductors,* Physica. **34,** 149 (1967).

[9] P.D. Wang, S.N. Holmes, T. Le, R.A. Stradling, I.T. Ferguson, A.G. De Oliveira, *Electrical and magneto-optical of MBE InAs on GaAs*, Semicond. Sci. Technol. **7,** 767 (1992).

[10] J.H. Davies, *The physics of low-dimensional semiconductors: an introduction*. (Cambrige University press, 1997).

[11] D. Bimberg, M. Grundmann, N.N. Ledentsov, *Quantum dot heterostructures*. (John Wiley & Sons, 1999).

[12] L. Pauling, *The nature of the chemical bond. IV. The energy of single bonds and the relative electronegativity of atoms*, J. Am. Chem. Soc. **54,** 3570 (1932).

[13] R.L. Anderson, *Germanium-Gallium Arsenide Heterojunctions [Letter to the Editor]*, IBM J. Res. Dev. **4,** 283 (1960).

[14] J.D. Bernal, *The Goldschmidt memorial lecture*, J. Chem. Soc. **2108** (1949).

[15] I. Vurgaftman, J.R. Meyer, L.R. Ram-Mohan, *Band parameters for III-V compound semiconductors and their alloys*, J. Appl. Phys. **89,** 5815 (2001).

[16] R. Marcks von Wurtemberg, P. Sundgren, J. Berggren, M. Hammar, M. Ghisoni, V. Oscarsson, E. Odling, J. Malmquist, Fabrication and *performance of 1.3-μm vertical-cavity surface-emitting lasers with InGaAs quantum well active regions grown on GaAs substrates, Micro-Optics, VCSELs*, and Photonic Interconnects. **5453,** 229 (2004).

[17] M. Grundmann, O. Stier, D. Bimberg, *InAs/GaAs pyramidal quantum dots: Strain distribution, optical phonons, and electronic structure*, Phys. Rev. B. **52,** 11969 (1995).

[18] H.Y. Liu, I.R. Sellers, T.J. Badcock, D.J. Mowbray, M.S. Skolnick, K.M. Groom, M. Gutiérrez, M. Hopkinson, J.S. Ng, J.P.R. David, R. Beanland, *Improved performance of 1.3 μm multilayer InAs quantum-dot lasers using a high-growth-temperature GaAs spacer layer*, Appl. Phys. Lett. **85**, 704 (2004).

[19] V. Pačebutas, K. Bertulis, G. Aleksejenko, A. Krotkus, *Molecular-beam-epitaxy grown GaBiAs for terahertz optoelectronic applications*, J. Mater. Sci. Mater. Electron. **20,** 363 (2009).

[20] P.M. Mooney, K.P. Watkins, Z. Jiang, A.F. Basile, R.B. Lewis, V. Bahrami-Yekta, M. Masnadi-Shirazi, D.A. Beaton, T. Tiedje, *Deep level defects in n-type GaAsBi and GaAs grown at low temperatures*, J. Appl. Phys. **113,** 13370 (2013).

[21] Ł. Gelczuk, J. Kopaczek, T.B.O. Rockett, R.D. Richards, R. Kudrawiec, *Deep-level defects in n-type GaAsBi alloys grown by molecular beam epitaxy at low temperature and their influence on optical properties*, Sci. Rep. **7,** 12824 (2017).

[22] S. Francoeur, M.-J. Seong, A. Mascarenhas, S. Tixier, M. Adamcyk, T. Tiedje, *Band gap of GaAs1−xBix, 0<x<3.6%*, Appl. Phys. Lett. **82,** 3874 (2003).

[23] T.J.C. Sweeney, S. J., Batool, Z., Hild, K., Jin, S. R., & Hosea, *The potential role of bismide alloys in future photonic devices*, 13th Int. Conf. Transparent Opt. Networks. 1–4 (2011).

[24] B. Fluegel, S. Francoeur, A. Mascarenhas, S. Tixier, E.C. Young, T. Tiedje, *Giant spin-orbit bowing in GaAs1-xBix*, Phys. Rev. Lett. **97,** 067205 (2006).

[25] K. Oe, H. Okamoto, *New semiconductor alloy GaAs 1-xBi x grown by metal organic vapor phase epitaxy*, Japanese J. Appl. Physics, **37,** L1283. (1998).

[26] S. Tixier, M. Adamcyk, T. Tiedje, S. Francoeur, A. Mascarenhas, P. Wei, F. Schiettekatte, *Molecular beam epitaxy growth of GaAs1−xBix*, Appl. Phys.

Lett. **82,** 2245 (2003).

[27] M. Yoshimoto, S. Murata, A. Chayahara, Y. Horino, J. Saraie, K. Oe, *Metastable GaAsBi Alloy Grown by Molecular Beam Epitaxy*, Japanese J. Appl. Physics, **42,** L1235. (2003).

[28] T. Tiedje, E.C. Young, A. Mascarenhas, *Growth and properties of the dilute bismide semiconductor GaAs 1-xBix a complementary alloy to the dilute nitrides*, Int. J. Nanotechnol. **5,** 963 (2008).

[29] W. Shan, W. Walukiewicz, J.W. Ager, E.E. Haller, J.F. Geisz, D.J. Friedman, J.M. Olson, S.R. Kurtz, *Band anticrossing in gainnas alloys*, Phys. Rev. Lett. **82,** 42287 (1999).

[30] S. Tixier, S.E. Webster, E.C. Young, T. Tiedje, S. Francoeur, A. Mascarenhas, P. Wei, F. Schiettekatte, *Band gaps of the dilute quaternary alloys GaN xas 1-x-yBi y and Ga 1-yin yN xas 1-x*, Appl. Phys. Lett. **86,** 112113 (2005).

[31] M.J. Seong, S. Francoeur, S. Yoon, A. Mascarenhas, S. Tixier, M. Adamcyk, T. Tiedje, Bi-induced vibrational modes in GaAsBi, Superlattices Microstruct. **37**, 394 (2005).

[32] M. Henini, J. Ibáñez, M. Schmidbauer, M. Shafi, S. V. Novikov, L. Turyanska, S.I. Molina, D.L. Sales, M.F. Chisholm, J. Misiewicz, *Molecular beam epitaxy of GaBiAs on (311) B GaAs substrates*, Appl. Phys. Lett. **91,** 350 (2007).

[33] R. Kudrawiec, P. Poloczek, J. Misiewicz, M. Shafi, J. Ibáñez, R.H. Mari, M. Henini, M. Schmidbauer, S.V. Novikov, L. Turyanska, S.I. Molina, D.L.

Sales, M.F. Chisholm, *Photomodulated transmittance of GaBiAs layers grown on (001) and (311)B GaAs substrates*, Microelectronics J. **40,** 537 (2009).

[34] S. Perkowitz, *Optical Characterization of Semiconductors: Infrared, Raman, and Photoluminescence Spectroscopy*. (Elsevier, 1993).

CHAPTER 3: SEMICONDUCTOR DEFECTS AND THEIR PROPERTIES

In this chapter, various types of defects are discussed. The effect of defects and their role as trapping and generation recombination centres will be presented. A classification of deep level defects in semiconductors and their carrier kinetics processes are also highlighted. In addition, the presence of defects in GaAs, and dilutes GaAsBi, with their properties will be covered.

3.1 CLASSIFICATION OF DEFECTS

A perfect crystal is created by repeating a basic unit cell along the three crystallographic orientations. However, in a real crystal, the lattice is not perfect and no crystal has such regularity, thus all crystals contain various types of defects. The defects range from point, complexes, and extended defects, all of which cause the crystal to be imperfect. In this section, an overview of the most important defects will be discussed.

3.1.1 POINT DEFECTS

A point defect, also known as a zero dimensional defect, occurs when an atom is missing or is located in an unusual site in the lattice structure. As a result, a point defect disrupts the crystal arrangements at an isolated location. Therefore, a point defect can be found in different forms such as vacancy, substitutional, interstitial and antisite impurities. A vacancy defect is normally caused by a missing atom at a certain crystal lattice site in a crystal structure, as shown in Fig. 3.1 (a). Another form of defect is the substitutional impurity, as depicted in Fig. 3.1 (b). It is created when a foreign atom impurity replaces and occupies a regular lattice site of the host atom. Similarly, an antisite defect is a special type of substitutional defect, which occurs in compound semiconductor materials like GaAs, and it is formed when a host atom occupies the site of another host atom. In GaAs, an example of an antisite defect is shown in Fig.3.1 (c), where an As atom occupies a Ga site [Ga antisite (As_{Ga})] or a Ga atom occupies an As site [As antisite (Ga_{As})]. The fourth form of a point defect is known as an interstitial impurity. This impurity is formed when an atom occupies the space between regular lattice sites. The interstitial impurity is divided into two categories: if this atom is the same as the host crystal then it is called self-interstitial, and when the atom is a foreign or impurity atom then it is called foreign-interstitial, as can be seen in Fig 3.1 (d). These point defects not only disrupt the crystal's periodicity, but also change the material's electricalproperties, e.g. they can significantly influence its conductivity.

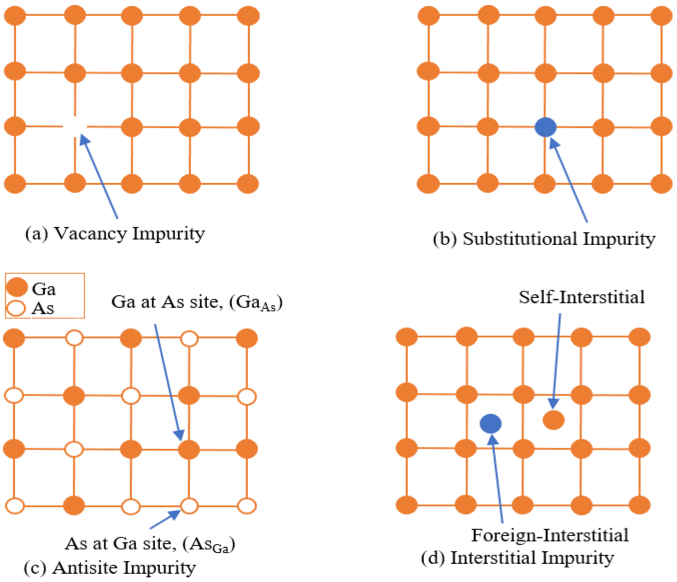

Fig. 3.1: Schematic diagrams of different kinds of point defects in crystalline semiconductors: (a) vacancy impurity; (b) substitutional impurity; (c) antisite impurity; and (d) interstitial impurity.

3.1.2 COMPLEXES OF POINT DEFECTS

When at least two or more point defects interact with each other, they form pairs known as point complex defects. There are different types of complex point defects, for example, a split-interstitials defect is a type of complex point defect and it is formed when two interstitials atoms create a pair in the lattice, as shown in Fig. 3.2 (a). These kinds of defects are formed by either a pair of two interstitial atoms from the same host material (self-interstitials), or by a pair of two impurity interstitials atoms (foreign interstitials). Furthermore, vacancy defects can also create a variety of complex defects in a crystalline material as shown in Fig. 3.2 (b). Particularly, when two vacancies form a pair, the resultant complex defect is referred to as a Di-vacancy. In addition, another kind of complex point defect, referred to as Frenkel defect, is formed when a vacancy and a self-interstitial atom form a pair. A pair of a vacancy and a foreign-interstitial form a vacancy-impurity complex. A split vacancy is created when two vacancies and an interstitial atom form a pair. Finally, an impurity pair complex defect occurs when a substitutional impurity atom forms a pair with an interstitial impurity atom, as shown in Fig. 3.2 (c).

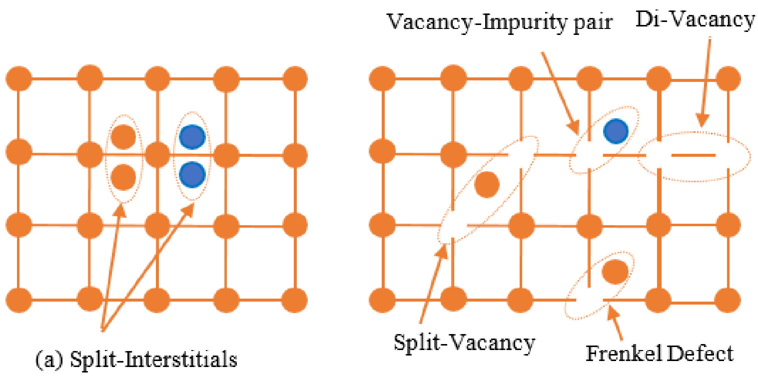

(a) Split-Interstitials

(b) Vacancy complexes

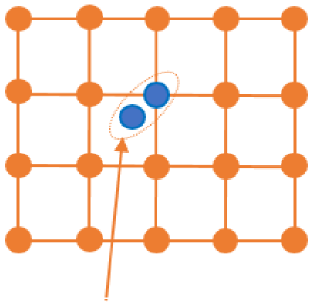

(c) Impurity-Pair

Fig. 3.2: (a) spilt-interstitials, (b) vacancy complexes, and (c) complexes of impurity-pair.

3.1.3 LINEAR DEFECTS

One of the most common defects in semiconductor is the linear defects, often known as dislocations or one-dimensional defects. These kinds of defects normally occur when an entire line of atoms (row) is missing from its normal lattice site in the crystal. Edge dislocations and screw dislocations are the most common types of linear defects. As shown in Fig. 3.3 (a), edge dislocation is formed when an extra half plane of atoms is inserted into the crystal lattice, causing distortion of nearby atoms. The screw dislocation is formed when one part of the crystal lattice is shifted with respect to the other crystal part, as shown in Fig. 3.3 (b).

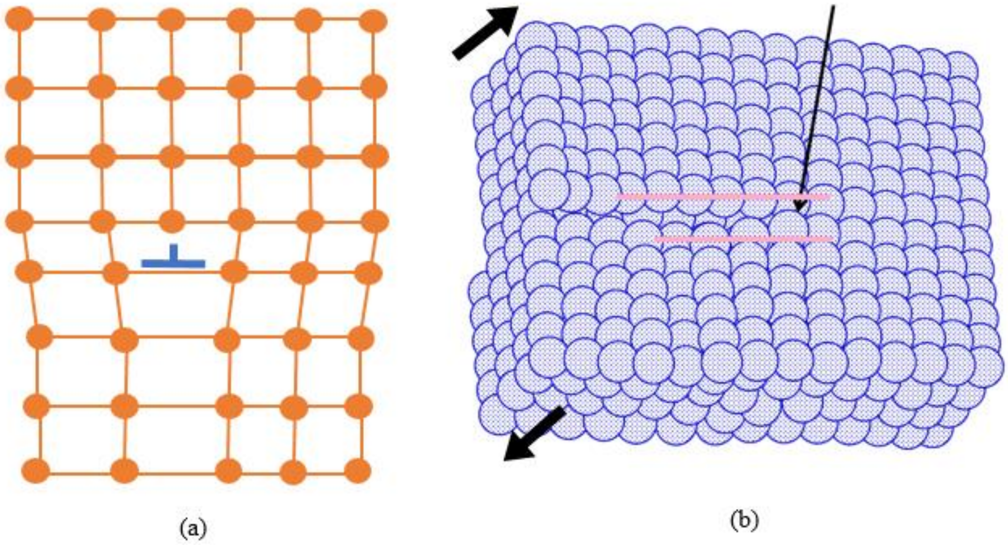
(a)
(b)

Fig. 3.3: Linear defects: (a) edge dislocations and (b) screw dislocations.

3.2 DEFECTS AND THEIR CARRIER KINETICS

The classification of defects based on their enegy and the mechansims of the generation-recombination processes will be thoroughly discussed in this section.

3.2.1 SHALLOW LEVELS AND DEEP LEVELS DEFECTS

Defects tend to have a significant effect on the electrical and optical properties of semiconductor materials. These defects or impurities, which introduce energy levels within the band gap of the material, are classified according to their energetic position. In particular, shallow levels impurities, which are intentionally introduced as dopant atoms, are located near the valence band (E_V) or conduction band (E_C) as shown in Fig. 3.4. If they contribute with electrons to the conduction band and holes to the valence band, these defects are known as shallow donors and acceptors, respectively [1]. Shallow levels have low ionization energy (< 0.025 eV) and easily ionized at room temperature, causing an increase of the electrical conductivity of semiconductor materials.

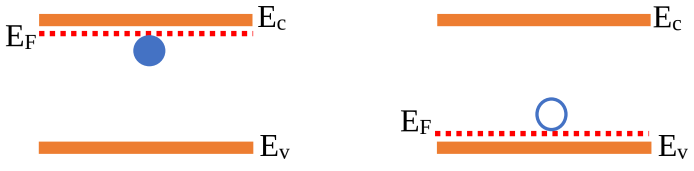

(a) (b)

Fig. 3.4: Schematic diagram of (a) shallow donor level, and (b) shallow acceptor level. E_c, E_v and E_F represent conduction band energy, valence band energy and Fermi level, respectively.

As can be seen in Fig. 3.5, deep level defects are situated far from the edges of conduction and valence bands and have energy levels greater than 0.1 eV. These energy levels are also known as recombination-generation centres and have a large impact on the electrical and optical properties of semiconductors. The conduction mechanisms, which involve these impurities levels, will be presented in the following section.

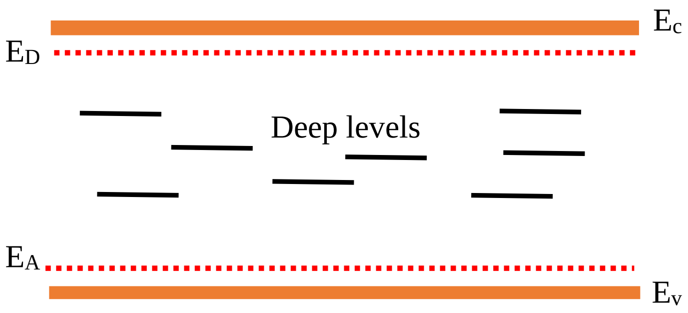

Fig. 3.5: Schematic diagram of deep level defects in semiconductors. E_D and E_A represent shallow donor level and acceptor donor level, respectively.

3.2.2 SHOCKLEY-READ-HALL THEORY

In 1952, the Shockley-Read-Hall (SRH) model was proposed to describe the statistics of recombination and generation of holes and electrons in semiconductors by the trapping mechanism [2]. When electrons are excited from the valence band to the conduction band, electron-hole pairs are formed (pair-generation process), creating free electrons and holes in the conduction band and valence band, respectively. These can contribute to the charge current. The equilibrium concentrations of electrons and holes stay constant with respect to time at thermodynamic equilibrium, resulting in a balance of generation and recombination processes rates. When an external source of energy such as light is applied, the carrier concentration will rise, and therefore the generation and recombination processes take place at different rates. As a result, non-equilibrium conditions will prevail in the system [3].

The emission and capture rates of charge carriers must be considered in order to calculate the occupancy of recombination-generation centres (G-R centres) at equilibrium. According to the theory, if E_T is considered to be the energy of a defect within the forbidden bandgap of a semiconductor, then four sub-processes can happen involving traps levels [3]:

(i) Electron capture, c_n: in this process an electron in the conduction band can be trapped in the deep center (Fig. 3.6 (a)).

(ii) Electron emission, e_n: in this process an electron can be emitted into the conduction band from the trap level E_T (Fig. 3.6 (b)).

(iii) Hole capture, c_P: in this process a hole from the valence band can be captured by the deep centre (Fig. 3.6 (c)).

(iv) Hole emission, e_p: in this process a captured hole from trap level E_T can be emitted into the valence band (or an electron from the valence band is trapped by a trap level E_T leaving a hole in the valence band) (Fig. 3.6 (d)).

The capture and emission processes of an electron and hole are shown in Fig. 3.6, where n is the density of electrons, p is the hole density, c_n is the electron capture coefficient, e_n is the electron emission rate, p_T is a G-R centre occupied by a hole, n_T is a G-R centre occupied by an electron, c_p is the hole capture coefficient and e_p is the emission rate of hole.

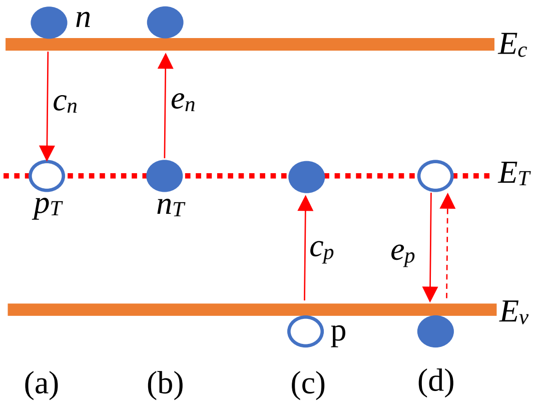

Fig. 3.6: Schematic diagram of capture and emission processes: (a) electron capture, (b) electron emission, (c) hole capture, and (d) hole emission [3].

The state n_T is neutral and the state p_T is positively charged, when a G-R centre is a donor. Alternatively, the state p_T is neutral and the state n_T is negatively charged, when G-R centre is an acceptor. The total density of G-R centres (N_T), occupied either by electrons (n_T) or holes (p_T), is given by:

$$N_T = n_T + p_T \tag{3.1}$$

When an electron or hole is generated by a centre or recombine in a centre, the electron density in the conduction band (n), the hole density in valence band (p) and charge states of the centres n_T and p_T change with time. The following relation describes the rate of change of n with respect to time:

$$\frac{dn}{dt}|_{G-R} = (b) - (a) = e_n n_T - c_n n p_T \tag{3.2}$$

where (a) and (b) are the electron capture and electron emission processes, respectively.

From Equation 3.2, the only parameters that affect the electron emission are the emission rate, (e_n: number of electrons per second emitted by G-R center to the conduction band) and the concentration of the traps that are occupied by electrons, (n_T). It is clear from equation 3.2, that the electron capture process depends only on the presence of electrons in the conduction band, n, the electron capture rate, c_n, and the concentration of hole occupied traps p_T.

Similarly, the change in holes density (p) over time can be described by equation 3.3:

$$\frac{dp}{dt}|_{G-R} = (d) - (c) = e_p p_T - c_p p n_T \tag{3.3}$$

where (c) and (d) are the hole capture and hole emission processes, respectively.

Since the electron capture coefficient c_n determined by the electron thermal velocity υ_{th} and the electron capture cross-section of the G-R center σ_n. c_n can be defined as:

$$c_n = \upsilon_{th} \sigma_n \tag{3.4}$$

The hole capture cofficient is given by:

$$c_{\mathrm{p}} = \upsilon_{th} \sigma_{n\mathrm{p}} \tag{3.5}$$

The density of the G-R state changes as a function of time during the emission or capture process of electrons and holes. Equations 3.2 and 3.3 can by used to calculate the rate change. This rate is determined by:

$$\frac{dn_T}{dt}\Big|_{G-R} = \frac{dp}{dt} - \frac{dn}{dt} = \left(c_n n + e_p\right)(N_T - n_T) - \left(c_p p + e_n\right)n_T \qquad (3.6)$$

In the steady state condition, the density is , $\frac{dn_T}{dt} = 0$. Equation 3.6 can then be rewritten as:

$$n_T = \frac{e_p + c_n n}{e_n + c_n n + e_p + c_p p} N_T \qquad (3.7)$$

When semiconductors are at thermal equilibrium, the rate of emission and capture are the same according to the detailed balance principle:

$$e_n n_T = c_n n p_T \qquad (3.8)$$

By substituting the electron capture coefficient c_n using Equation 3.4 into Equation 3.8, the following equation is obtained:

$$e_n n_T = v_{th}\sigma_n n p_T \qquad (3.9)$$

In the case of holes, a similar equation is found:

$$e_p p_T = v_{th}\sigma_p p n_T \qquad (3.10)$$

The total density of deep levels considering the function of Fermi-Dirac distribution, f, is given by

$$N_T = n_T + p_T = N_T f + N_T(1 - f) \qquad (3.11)$$

where f gives the probability of an electron occupying the energy level E_T and is given by

$$f = \left[\frac{1}{1 + \exp\left(\frac{E_T - E_F}{k_B T}\right)}\right] \qquad (3.12)$$

where E_F is the energy of the Fermi level, k_B is Boltzmann constant and T is temperature.

Substituting Equations 3.11 and 3.12 in Equation 3.8, reults in the following equation.

$$e_n = \sigma_n \langle \upsilon_n \rangle_{th} n \exp\left(\frac{E_T - E_F}{k_B T}\right) \tag{3.13}$$

where *n* is the electron density in conduction band and is given by

$$n = n_i \exp\left(\frac{E_F - E_i}{k_B T}\right) = N_c \exp\left(-\frac{E_c - E_F}{k_B T}\right) \tag{3.14}$$

where n_i is the intrinsic carrier concentration of the material, $n_i = N_c \exp\left(\frac{E_i - E_c}{k_B T}\right)$.

Subsequently, by combining Equation 3.14 and Equation 3.13, the following equation is obtained:

$$e_n = \sigma_n \langle \upsilon_n \rangle_{th} N_c \exp\left(-\frac{E_c - E_T}{k_B T}\right) \tag{3.15}$$

where N_c is the density of states in the conduction band, $N_c = 2\left(\frac{2\pi m_e^* k_B T}{h^2}\right)^{3/2}$ and $\langle \upsilon_n \rangle_{th}$ is the thermal velocity of electrons, $\langle \upsilon_n \rangle_{th} = \left(\frac{3k_B T}{m_e^*}\right)^{\frac{1}{2}}$ and $m_e^*$is the effective mass of electrons.

Similarly, in the case of holes, substituting $p = N_v \exp\left(-\frac{E_F - E_v}{k_B T}\right)$ in Equation (3.10), gives:

$$e_p = \sigma_p \langle \upsilon_p \rangle_{th} N_v \exp\left(-\frac{E_T - E_v}{k_B T}\right) \tag{3.16}$$

where N_v is the density of states in the valence band, $N_v = 2\left(\frac{2\pi m_h^* k_B T}{h^2}\right)^{3/2}$ and $\langle \upsilon_p \rangle_{th}$ is the thermal velocity of holes, $\langle \upsilon_p \rangle_{th} = \left(\frac{3k_B T}{m_h^*}\right)^{\frac{1}{2}}$ and m_h^* is the effective mass of holes.

Equations 3.15 and 3.16 can be substituted with values of $\langle v_n \rangle_{th}$ and N$_c$, and $\langle v_p \rangle_{th}$ and N_v, respectively, and can be written as:

$$e_n = AT^2\sigma_n \exp\left(-\frac{E_c - E_T}{k_B T}\right) \tag{3.17}$$

$$e_p = AT^2\sigma_p \exp\left(-\frac{E_T - E_v}{k_B T}\right) \tag{3.18}$$

where A is a constant, given by:

$$A = 2\left(\frac{2\pi m_e^* k_B}{h^2}\right)^{3/2}\left(\frac{3k_B}{m_e^*}\right)^{1/2} = 4m_e^*\frac{\sqrt{6\pi^3}(k_B)^2}{h^3}$$

The Arrhenius plot of $\left(\frac{e_{n,p}}{T^2}\right)$ versus $\left(\frac{1000}{T}\right)$ provides a straight line graph, from which the activation energy of the deep level can be calculated using the slope of this plot.

3.3 DEFECTS IN COMPOUND SEMICONDUCTORS

Because semiconductor materials are used in almost all modern electronic devices, the semiconductor industry has seen considerable expansion. However, the key challenges and problems in these industries are the production of perfect crystals and structures. In fact, all crystal structures have imperfections due for example to foreign atoms being incorporated unintentionally into the host lattice of semiconductors and/or some atoms can be missing in the crystal due to fabrication processes [1]. Generally, the presence of defects in electronics devices affects significantly their performance by altering their electrical and optical properties. Therefore, identifying and characterising the defects formed during the growth and processing of these materials and devices is critical to understanding their performance [3]. A brief literature overview of defects in GaAs and GaAsBi materials will be discussed in the following section.

3.3.1 DEFECTS IN GaAs

GaAs is widely employed in a variety of electronics and optoelectronics devices. Indeed, different forms of native defects, such as vacancies, interstitials, and antisite defects, can be found in GaAs strutures as a result of the growth process. One of the most common and well-known intrinsic defects in bulk and epitaxial GaAs grown by different techinques is *EL2*. This deep level defect typically has an energy level in the range of 0.70 eV to 0.85 eV [4] with trap concentrations ranging from $\sim 10^{14}$ cm^{-3} to $\sim 10^{16}$ cm^{-3} [5]. The origin of *EL2* is assigned to the isolated Arsenic antisite defect (As_{Ga}) [6–8] or to a complex defect involving As_{Ga} and arsenic interstitial (As_i) [8,9]. In addition, *EL2* defect plays a significant role in controlling the resistivity of GaAs to produce semi-insulating GaAs substrates, which are important in integrated circuit technology [10]. Another common deep level trap in GaAs is *EL3*. This trap has an activation energy range from ~0.408 eV to ~0.575 eV [11]. This trap is commonly associated with complexes of As_i and Arsenic-vacancy (V_{As}) [12]. The presence of *EL5* (~0.43 eV) in GaAs was attributed to complexes involving As interstitials-Ga vacancies (As_iV_{Ga}) [13]. Another common intrinsic defect in GaAs is *EL6* (~0.35 eV) [10] whose origin was associated with native pair defects involving two point defcets, namely: As_{Ga} and V_{As} [14]. Furthermore, trap *EL10* with small activation energy of ~0.18eV, commonly found in bulk GaAs [11], was assigned to a complex defect involving V_{As} and an impurity [15,16].

3.3.2 DEFECTS IN DILUTES GaAsBi

GaAsBi materials are very important alloys due to their unique properties including: (i) the incorporation of Bi into GaAs affects the valence band maxima of GaAs rather than the conduction band. Thus, due to the strong carrier scattering at localized states created by the incorporation of Bi, the hole density and mobility in GaAs are mainly affected [17]; (ii) Bi reduces the band gap of GaAs to low energies more than four times, when compared to Sb or In for the same alloy content [18]; (iii) Bi causes a large spin- orbit splitting in band gap structure which can suppress Auger processes [19]. Indeed, the substantial reduction in the band gap of GaAs (~84 meV /% Bi) [19] due to the incorporation of Bi is of great interest for devices that operate in the long wavelength region [20,21], as well a promising candidate for optoelectronic devices [22].

Due to the large difference in the radii between Bi and As atoms, the substitution of As atoms by Bi atoms in GaAs causes a compressive strain which affect considerably the band structure of GaAs. Furthermore, the localised potential of Bi and the surrounding lattice can as well change the electronic band structure of GaAs. Therefore, incorporation of Bi causes structural defects in GaAs, which can degrade its crystal quality. Furthermore, because Bi tends to surface-segregate at standard GaAs growth temperatures, incorporation of Bi into GaAs necessitates lower growth temperatures, which leads to the creation of defects that can act as non-radiative recombination centers. However, because of the large disparity in atomic potentials and electronegativity between As and Bi, localised states are created at the valence band maxima of GaAs which can also act as trapping centres for the bound holes that could reduce the number of non-radiative centres.

Electrically active defect states in dilute bismide materials have not been thoroughly investigated. However, G. Giatto et al. [23] examined the spatial distribution of Bi atoms experimentally using x-ray absorption spectroscopy, and found that at 1.9%Bi, Bi spread randomly, whereas at 2.4%Bi, it formed pairs and clusters, affecting its electrical and optical properties. The following are some of the defects and properties associated to Bi in GaAs. Bismuth antisite defects (Bi_{Ga}) were reported in GaAsBi layers by M. Kunzer et al. [24]. They observed that a large quantity of Bi, roughly 10%, occupied Ga sites rather than substituting As in Bi-doped Czochralski-grown GaAs. Using electron spin resonance (ESR) technique, they determined an energy level of 0.35-0.5 eV, and observed an increase in both the resistivity and carrier trapping rate in GaAsBi. Furthermore, it is worth noting that the DLTS (Deep Level Transient Spectroscopy) technique has been used by a number of researchers to characterise electrically active defects in GaAsBi alloys. For example, P. M. Mooney et al. [25] have performed DLTS measurements on n-type GaAsBi layers having Bi composition ranging from $\sim 0 \leq x \leq 0.011$ and grown by MBE at substrate temperature ~ 330 ℃. In this study, they reported that the incorporation of Bi into GaAs suppressed the formation of an electron trap with energy level 0.40 eV, by decreasing the total trap concentration in GaAsBi by a factor of 20 as compared to GaAs. They also found that trap “A” with activation energy of 0.12 eV was observed only in GaAsBi sample with 0.7 % Bi, and suggested that this trap may involve Bi as constituent. In addition, P. M. Mooney et al. [26] investigated the electrically active defects in n and p-type GaAsBi epilayers grown by MBE under UV illumination under similar experimental conditions using DLTS measurements. They detected two hole traps, namely H6 and H4, which were observed only in samples containing Bi, and not in p-GaAs. They attributed these defects states with Bi pairs or clusters.

Recently, Ł. Gelczuk et al. [10] employed DLTS to investigate the electron deep level defects in n-type $GaAs_{1-x}Bi_x$ alloys having $0<x<0.023$ grown by MBE on conventional (100) n^+ GaAs substrates. They found that the incorporation of Bi into GaAs suppresses the formation of electron traps observed in GaAs by reducing their total trap concentrations to more than two order of magnitude as compared to trap concentrations in GaAs grown under the same conditions. In addition, they reported that the two levels labelled as ET_0 and ET_1 with activation energies ranging from 0.07 to 0.19 eV in GaAsBi with Bi compositions of 0.8%-2.3%, are Bi- related traps. They suggested that the origin of these defects could be related to Bi pair defects. More recently, M. Fregolent et al. [27], presented a detailed analysis of the properties of defects in n-type GaAsBi grown by MBE at low temperature (~ 390 ℃), having Bi compositions ranging from ~ 1% - 3%). In this study, they detected two traps related to defects involving Bi. One is an electron trap, named as E2 with activation energy varying from 0.32 to 0.48 eV. E2 was assigned to an antisite complex defect $(V_{Ga}+ Bi_{As})^{2-/3-}$. The other one is a hole trap labelled as H_0 with energy level of 1.44 eV. This hole trap, which was comparable to trap HT2 observed by Fuyuki et al [28], was suggested to be a point defect related to As_{Ga} or Bi_{Ga} antisites. It is worth pointing out that the well-known defects in bulk GaAs, *EL2*, *EL3*, and *EL6* were also detected in GaAsBi layers.

REFERENCES

[1] M. D. McCluskey and E. E. Haller, *Dopants and Defects in Semiconductors*. (CRC Press, 2012).

[2] Shockley WT, Read Jr WT, *Statistics of the recombination of electrons and holes*, Phys. Rev. **87,** 835 (1952).

[3] D. K. Schroder, *Semiconductor materials and devices characterization*. (John Wiley & Sons, 2006).

[4] J. Bourgoin and T. Neffati, *The energy level of the EL2 defects in GaAs*, Solid State Electron. **43,** 153 (1999).

[5] J.C. Von Bardeleben, H. J., Stievenard, D., Deresmes, D., Huber, A., & Bourgoin, *Identification of a defect in a semiconductor: EL2 in GaAs*, Phys. Rev. B. **34,** 7192 (1986).

[6] J. Lagowski, M. Kaminska, J.M. Parsey, H.C. Gatos, M. Lichtensteiger, *Passivation of the dominant deep level (EL2) in GaAs by hydrogen*, Appl. Phys. Lett. **41,** 1078 (1982).

[7] Baeumler, M., Kaufmann, U. and Windscheif, J, *Photoresponse of the AsGa antisite defect in as-grown GaAs*, Appl. Phys. Lett. **46,** 781 (1985).

[8] A.C. Irvine, D.W. Palmer, *First observation of the EL2 lattice defect in indium gallium arsenide grown by molecular-beam epitaxy*, Phys. Rev. Lett. **68,** 2168 (1992).

[9] M. Kaminska and E. R. Weber, *EL2 defect in GaAs*, Semicond. Semimetals. **38,** 59 (1993).

[10] Ł. Gelczuk, J. Kopaczek, T.B.O. Rockett, R.D. Richards, R. Kudrawiec, *Deep-level defects in n-type GaAsBi alloys grown by molecular beam epitaxy at low temperature and their influence on optical properties*, Sci.

Rep. **7,** 12824 (2017).

[11] G.M. Martin, A. Mitonneau, A. Mircea, *Electron traps in bulk and epitaxial GaAs crystals*, Electron. Lett. **13,** 191 (1977).

[12] J.R. Morante, A. Pérez-Rodríguez, J. Samitier, A. Romano-Rodríguez, *On the artificial creation of the EL2 center by means of boron implantation in gallium arsenide*, J. Appl. Phys. **70,** 4202 (1991).

[13] R. Yakimova, T. Paskova, C. Hardalov, *Behavior of an EL5-like defect in metalorganic vapor-phase epitaxial GaAs:Sb*, J. Appl. Phys. **74,** 6170 (1993).

[14] K. Yokota, H. Kuchii, K. Nakamura, M. Sakaguchi, H. Takano, Y. Ando, *EL2, EL3, and EL6 defects in GaAs highly implanted with sulfur*, J. Appl. Phys. **88,** 5017 (2000).

[15] D. V. Lang, A.Y. Cho, A.C. Gossard, M. Ilegems, W. Wiegmann, *Study of electron traps in n -GaAs grown by molecular beam epitaxy*, J. Appl. Phys. **47,** 2558 (1976).

[16] P. Blood, J.J. Harris, *Deep states in GaAs grown by molecular beam epitaxy*, J. Appl. Phys. **56,** 993 (1984).

[17] R.N. Kini, A.J. Ptak, B. Fluegel, R. France, R.C. Reedy, A. Mascarenhas, *Effect of Bi alloying on the hole transport in the dilute bismide alloy GaAs1-xBix*, Phys. Rev. B. **83,** 075307 (2011).

[18] A. Mascarenhas, S. Francoeur, S. Yoon, *Physics of Isoelectronic Dopants in GaAs*. (Elsevier, 2005).

[19] B. Fluegel, S. Francoeur, A. Mascarenhas, S. Tixier, E.C. Young, T. Tiedje, *Giant spin-orbit bowing in GaAs1-xBix*, Phys. Rev. Lett. **97,** 067205 (2006).

[20] S. Tixier, M. Adamcyk, T. Tiedje, S. Francoeur, A. Mascarenhas, P. Wei, F.

Schiettekatte, *Molecular beam epitaxy growth of GaAs1−xBix*, Appl. Phys. Lett. **82,** 2245 (2003).

[21] Y. Tominaga, Y. Kinoshita, K. Oe, M. Yoshimoto, *Structural investigation of GaAs1-xBix/GaAs multiquantum wells,* Appl. Phys. Lett. **93,** 131915 (2008).

[22] I.P. Marko, C.A. Broderick, S. Jin, P. Ludewig, W. Stolz, K. Volz, J.M. Rorison, E.P. O'Reilly, S.J. Sweeney, *Optical gain in GaAsBi/GaAs quantum well diode lasers,* Sci. Rep. **6,** 28863 (2016).

[23] G. Ciatto, E.C. Young, F. Glas, J. Chen, R.A. Mori, T. Tiedje, *Spatial correlation between Bi atoms in dilute GaAs1-x Bix: From random distribution to Bi pairing and clustering*, Phys. Rev. B. **78,** 035325 (2008).

[24] M. Kunzer, W. Jost, U. Kaufmann, H.M. Hobgood, R.N. Thomas, *Identification of the Bi Ga heteroantisite defect in GaAs: Bi*, Phys. Rev. B. **48,** 4437 (1993).

[25] P.M. Mooney, K.P. Watkins, Z. Jiang, A.F. Basile, R.B. Lewis, V. Bahrami-Yekta, M. Masnadi-Shirazi, D.A. Beaton, T. Tiedje, *Deep level defects in n-type GaAsBi and GaAs grown at low temperatures*, J. Appl. Phys. **113,** 13370 (2013).

[26] P.M. Mooney, M. Tarun, D.A. Beaton, A. Mascarenhas, K. Alberi, *Deep level defects in dilute GaAsBi alloys grown under intense UV illumination,* Semicond. Sci. Technol. **31,** 085014 (2016).

[27] M. Fregolent, M. Buffolo, C. De Santi, S. Hasegawa, J. Matsumura, H. Nishinaka, M. Yoshimoto, G. Meneghesso, E. Zanoni, M. Meneghini, *Deep levels and carrier capture kinetics in n-GaAsBi alloys investigated by deep level transient spectroscopy,* J. Phys. D. Appl. Phys. **54,** 345109 (2021).

[28] T. Fuyuki, S. Kashiyama, Y. Tominaga, K. Oe, M. Yoshimoto, *Deep-hole traps in p-type GaAs1-xBix grown by molecular beam epitaxy*, Jpn. J. Appl. Phys. **50,** 080203 (2011).

CHAPTER 4: EXPERIMENTAL TECHNIQUES

Semiconductor materials form the basis of several types of electronic and optoelectronic devices, which require electrical contacts. Such contacts can include semiconductor-semiconductor contacts (e.g. p-n junction), where a p-type semiconductor is brought into contact with an n-type semiconductor, and metal-semiconductor contacts, known as Schottky junction/diode or Schottky barrier, where one of the doped side (p-type or n-type) in a p-n junction is replaced by a metal [2]. The main difference between a p-n junction and a Schottky barrier is in the depletion region. A depletion region formed in a p-n junction spreads to both sides where electrons in the n-type region move towards the p-type region and combine with the holes. In this process, fixed negative ions are left on the p-type region, while fixed positive ions are left on the n-type region. These ions of opposite polarity will cause an electrical field on both sides of the junction within the depleted area, preventing further electrons transfer. In the case of a Schottky barrier, the entire depletion region is on the semiconductor side since the depletion layer on the metal side is not existent. Both of these types of electrical contacts are favoured for deep level transient spectroscopy (DLTS) measurements. In this chapter, a Schottky junction will be discussed. The characterization techniques, namely current-voltage (I-V), capacitance-voltage (C-V), DLTS, Laplace DLTS and Photoluminescence (PL), which have been used to investigate the samples presented in this thesis, are reviewed.

4.1 SCHOTTKY DIODE

A Schottky diode is formed when a metal with a work function Φ_m is brought into contact with a semiconductor having a work function $\Phi_s < \Phi_m$. If $\Phi_s > \Phi_m$ an Ohmic contact is formed. Prior to the metal and semiconductor being brought into contact, their Fermi energy levels are different. However, for a semiconductor, once the two materials are into contact, the Fermi levels line up due to the flow of electrons from the conduction band (CB) of the semiconductor, to the metal side of the junction [2]. Fig. 4.1 schematically shows the band diagram of isolated metal and semiconductor, while Fig. 4.2 displays the energy band of the Schottky diode under equilibrium conditions.

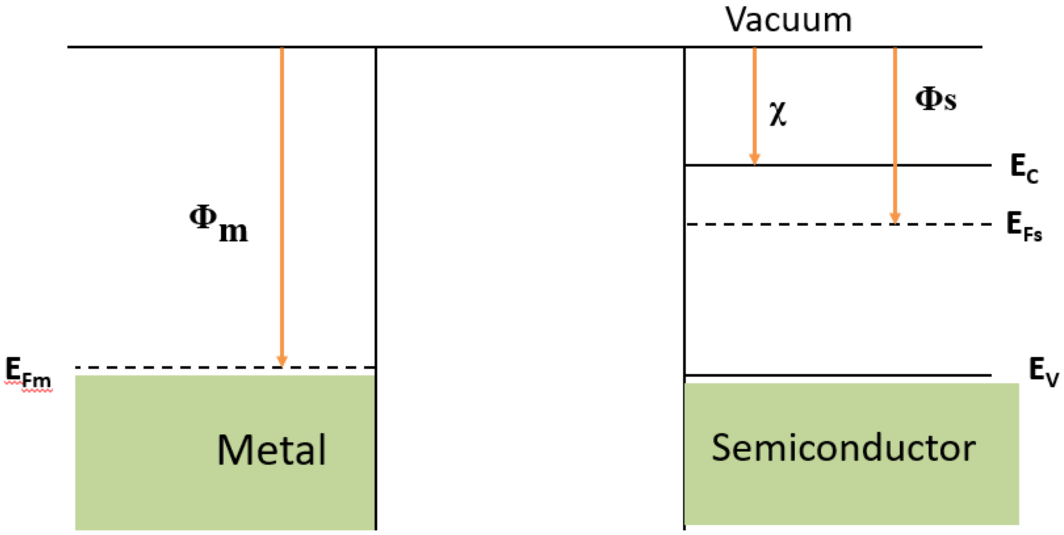

Fig. 4.1: Metal and semiconductor energy band diagrams.

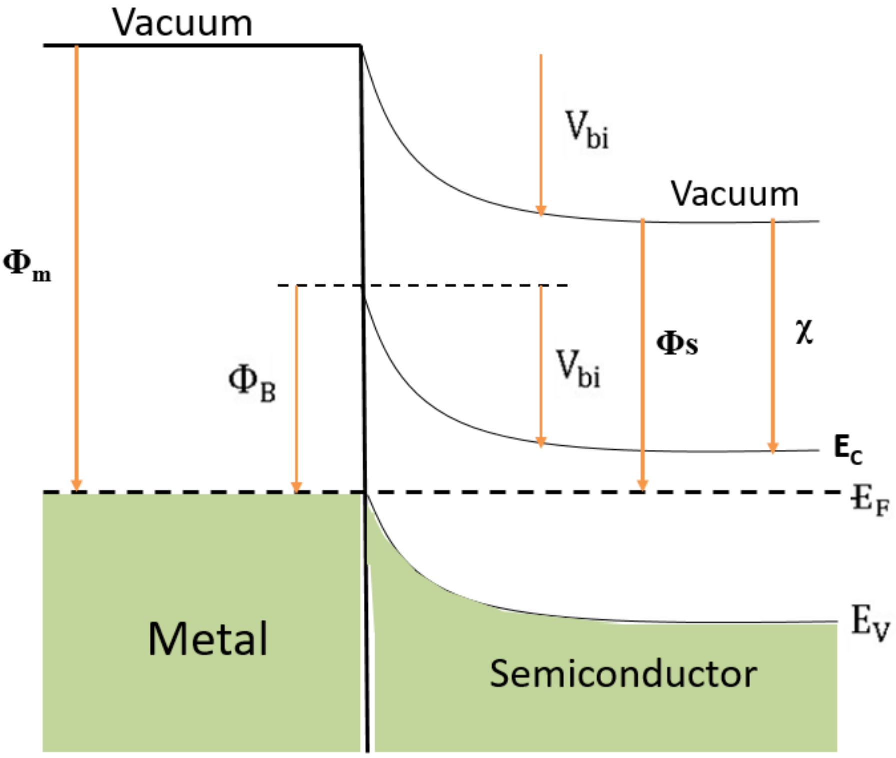

Fig. 4.2: Band diagram of a Schottky contact

Φ_m is the work function of the metal representing the energy required to remove an electron from the metal to vacuum, E_{Fm} is the metal's Fermi level, Φ_s is the semiconductor work function, E_C, E_V and E_F are the energies of the conduction band, valence band and Fermi level, respectively. The electron affinity χ is the energy required to extract an electron from the conduction band (E_C) to the vacuum. For an ideal Schottky diode, the barrier height (ϕ_B) is the barrier that electrons face when they move from metal to semiconductor, and is equal to:

$$\phi_B = \Phi_m - \chi \tag{4.1}$$

On the other hand, in the semiconductor side the change of Fermi level and the depletion region, creates what is called a built-in potential (V_{bi}) which prevents the flow of further electrons from the semiconductor to the metal side of the junction. The built-in potential is given by the following formula:

$$V_{bi} = \Phi_m - \Phi_s \tag{4.2}$$

4.1.1 DEPLETION REGION

Once a metal and an n-type semiconductor are brought into contact, some electrons from the semiconductor side start to migrate to the metal side until a balance in the Fermi levels for both the metal and semiconductor is reached. The migration of electrons leaves behind positively charged ions in the semiconductor, which creates a region with no free charge carriers called a depletion region. This depletion region is formed on the semiconductor side near the interface with the metal [1]. The width of the depletion region (W) can be affected by the applied voltage, built-in potential (V_{bi}) , and the doping concentration. If ρ(x) is the charge density of the depletion region, W can be obtained by using Poisson‟s equation.

$$\mathrm{V} = \frac{1}{\varepsilon_s} \int_0^{W} x \, \rho(x) \mathrm{d}x \tag{4.3}$$

where V is the net potential across the Schottky junction, ε_s and x are the dielectric constant and the distance from the junction to the semiconductor, respectively.

When ρ(x) is considered uniform, it can be written as;

$$\rho = qN_d \tag{4.4}$$

By using Equations 4.3 and 4.4, the width of the depletion region can be given as

$$W = \sqrt{\frac{2\varepsilon_s V}{qN_d}} \tag{4.5}$$

where N_d is concentration of donor ions in the depletion region and q is the charge of carrier. In an ideal situation, the depletion region is completely free of carriers. This is called the depletion region approximation and assumes sharp boundaries between the neutral and depletion regions. However, in reality, it is difficult to have a sharp boundary due to the existence of some charges in the depletion region close to the neutral region. This region of charges in the depletion region is called the Debye length (L_D) and is given by:

$$L_D = \sqrt{\frac{\varepsilon_s k_B T}{q^2 N_d}} \tag{4.6}$$

where k_B and T are the Boltzmann constant and temperature in Kelvin, respectively. When using a low-doped semiconductor or when a large reverse bias is applied, the width of the depletion region will be much larger than the Debye length. In this case, the depletion region approximation is considered to be satisfied [3].

4.1.2 SCHOTTKY DIODE UNDER BIAS CONDITIONS

The Schottky diode at equilibrium condition has been presented in **Fig. 4.2**. The diode will no longer be in this condition if an external voltage is applied. A current will flow through the junction and will depend on the polarity of the voltage applied across metal/semiconductor. If a forward bias V_F is applied ($V_F > 0$; + to the metal and – to the semiconductor), the potential barrier on the semiconductor side (V_{bi}) decreases by V_F to (V_{bi} - V_F). The reduction in the built-in potential is due to the increase of the semiconductor Fermi level by V_F, as shown in Fig. 4.3. On the other hand, if a reverse bias is applied ($V_R < 0$), the Fermi level of the semiconductor decreases by the applied voltage, which is shown in Fig. 4.4. Therefore, the built-in potential will be increased by the amount of applied voltage to (V_{bi} + V_R) [1,3]. The width of the depletion region is affected by the applied voltage. Under forward bias, the depletion region is reduced, and Equation 4.5 is given by:

$$W = \sqrt{\frac{2\varepsilon_s(V_{bi}-V_F)}{qN_d}} \tag{4.7}$$

However, if a reverse bias is applied, the depletion width will get wider and is given by:

$$W = \sqrt{\frac{2\varepsilon_s(V_{bi}+V_R)}{qN_d}} \tag{4.8}$$

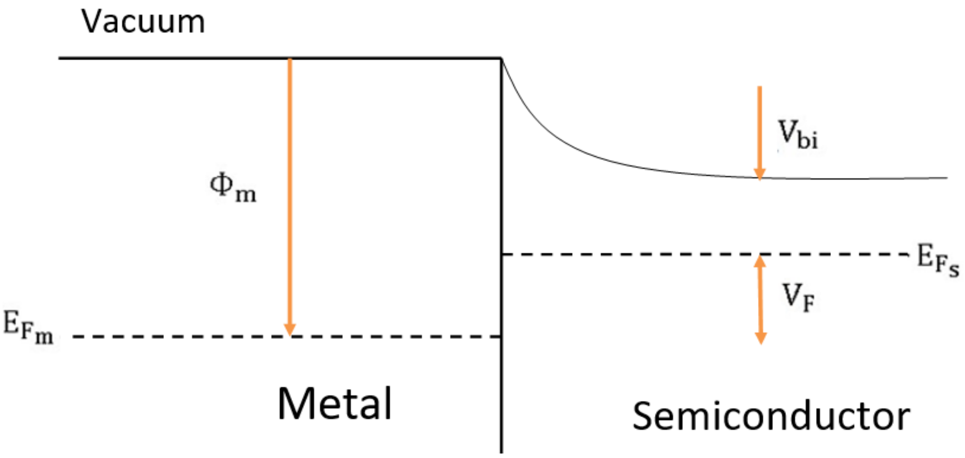

Fig. 4.3: Energy band diagram of a Schottky diode under a forward bias.

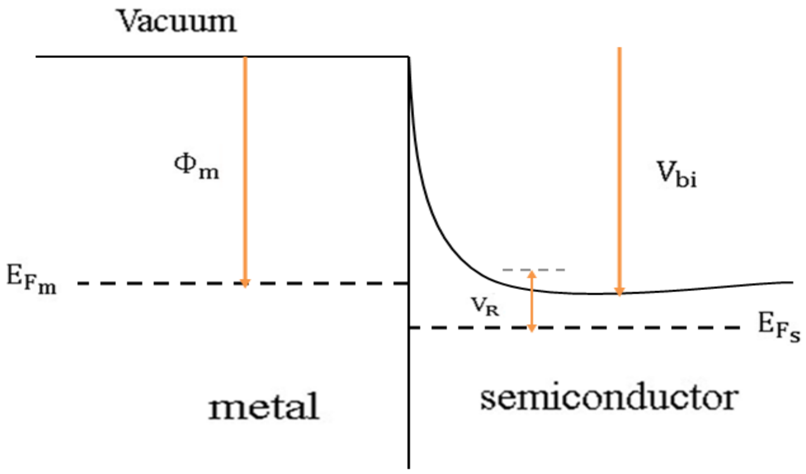

Fig. 4.4: Energy band diagram of a Schottky diode under a reverse bias.

4.2 CAPACITANCE – VOLTAGE (C-V) MEASUREMENTS

The capacitance of a Schottky diode can be compared to the capacitance of a parallel plate capacitor, which is given by:

$$C = \frac{dQ}{dV} \tag{4.9}$$

where dQ is the change of the charge in the depletion region, and dV is the applied voltage. The expression of the capacitance for the parallel plate capacitor can be used as the capacitance of the Schottky diode. Therefore, C can be written as:

$$C = \frac{A\varepsilon_s}{W} \tag{4.10}$$

where A is the area of the diode and W is the width of the depletion region [4]. When a reverse bias is applied, Equation 4.10 can be rewritten by using Equation 4.8 as:

$$C = \frac{dQ}{dV_R} = \frac{A}{2}\sqrt{\frac{2\varepsilon_s q N_d}{V_{bi}+V_R}} \tag{4.11}$$

As can be seen from above equation, the capacitance decreases with increasing reverse bias. In Fig. 4.5, it can be shown that by plotting ($1/C^2$) versus (V_R), the doping concentration (N_d) and the built-in potential (V_{bi}) can be obtained from the slope and the intercept at $1/C^2 = 0$, respectively. If a linear relationship between ($1/C^2$) and (V_R) is obtained, the doping concentration is uniformly distributed throughout the depletion region. However, N_d is non-uniform in the case of a non-linear relationship.

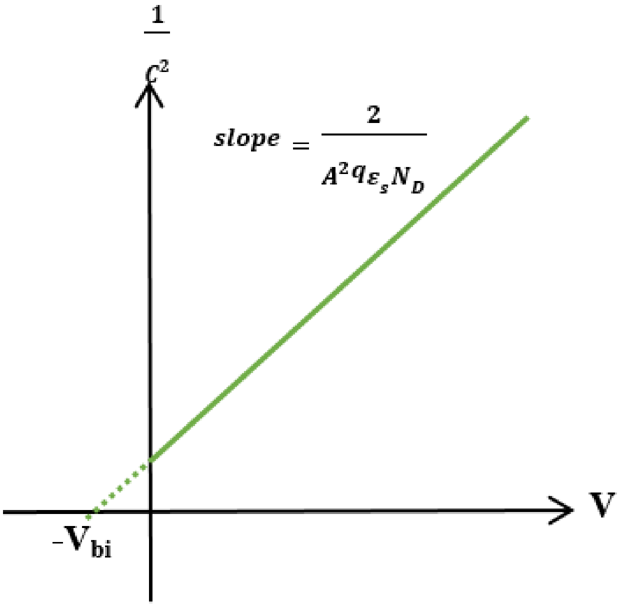

Fig. 4.5: Typical plot of $1/C^2$ versus reverse bias V_R.

4.3 CURRENT – VOLTAGE (I-V) MEASUREMENTS

For an ideal Schottky or p-n junction, the I-V characteristics could be described by the thermionic emission model [5] that includes series resistance (R_s) as:

$$I = I_0[exp\left(\frac{q(V-IR_S)}{nk_BT}\right) - 1] \tag{4.12}$$

where q is the elementary charge, V is the applied voltage, n is the ideality factor, k_B is Boltzmann's constant, T is the temperature and I_0 is the saturation current, which is given by:

$$I_0 = AA^*T^2\,exp\left(\frac{-q\phi_B}{k_BT}\right) \tag{4.13}$$

where A is the effective diode area, A^* is the effective Richardson's constant for the semiconductor material and ϕ_B is the barrier height. It can be noted that I is the current due to the thermionic emission of majority carriers from the semiconductor to the metal. The saturation current (I_0) is the current flow from the metal to the semiconductor and it is independent of the applied voltage.

When a forward bias is applied, $(V - IR_s)\ >>\ k_BT$ and hence Equation 4.12 can be rewritten as:

$$I = I_0\,exp\left(\frac{q(V-IR_S)}{nk_BT}\right) \tag{4.14}$$

Taking the first derivative of I with respect to V results in the following equation:

$$dI/dV = I_0\left(\frac{q}{nk_BT}exp\left(\frac{q(V-IR_S)}{nk_BT}\right) - \frac{q}{nk_BT}exp\left(\frac{q(V-IR_S)}{nk_BT}\right)R_s\frac{dI}{dV}\right) \tag{4.15}$$

Note that $dI/dV = G$, where G is the conductance. Equation 4.15 can be rewritten as:

$$G = \frac{q}{nk_BT} I_0\, exp\left(\frac{q(V-IR_S)}{nk_BT}\right)(1 - G.R_s) = \frac{q}{nk_BT} I\,(1 - G.R_s) \qquad (4.16)$$

$$\frac{G}{I} = \frac{q}{nk_{\boldsymbol{B}}T} - \frac{qR_S}{nk_BT}\,\mathrm{G} \qquad (4.17)$$

By plotting G/I versus G, a straight line is obtained, as shown in **Fig. 4.6**. The ideality factor (n) and R_S could be extracted from the y-intercept and the slope, respectively. This method of extracting n and R_S experimentally is known as Werner's method [6].

By taking the logarithm of Equation 4.14 and plotting $ln\,(I)$ versus $(V - IR_S)$, I_0 could be extracted from the y-intercept. By taking the logarithm of Equation 4.14, equation 4.18 is obtained:

$$ln\,(I) = ln\,(I_0) + \frac{q(V-IR_S)}{nk_BT} \qquad (4.18)$$

Then, by substituting I_0 expressed in Equation (4.13), $\emptyset_B$ can be calculated.

$$\emptyset_B = \frac{k_{\boldsymbol{B}}T}{q} ln\left(\frac{AA^*T^2}{I_0}\right) \qquad (4.19)$$

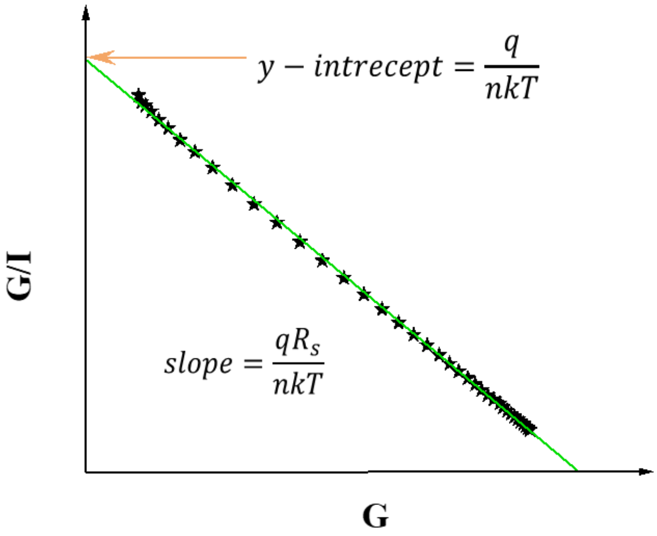

Fig. 4.6: Plot of G/I versus G.

4.4 DEEP LEVEL TRANSIENT SPECTROSCOPY (DLTS)

In 1974, D. V. Lang [7] introduced a novel technique, the so-called deep level transient spectroscopy (DLTS), to investigate the electrically active defects in semiconductors materials. This technique is based on the change of capacitance of a Schottky or a p-n junction diode associated with the space charge region (depletion region). The carriers emission process from the deep levels can be monitored by measuring the capacitance as a function of time and sample temperature. This can be then used to determine different parameters of the defect such as activation energy and capture cross-section.

4.4.1 CAPACITANCE TRANSIENTS

The DLTS technique is based on the concept of capacitance transient that occur in the depletion region of a Schottky or a p-n diode following a reverse bias voltage pulse. If the Schottky is made with an n-type semiconductor, only electrons play a significant role in normal operation of the device. So, the Schottky diode is called majority carrier. Fig. 4.7 illustrates a schematic diagram of the energy band of a Schottky junction under reverse bias (V_R) and the corresponding capacitance transient during a filling pulse (V_P).

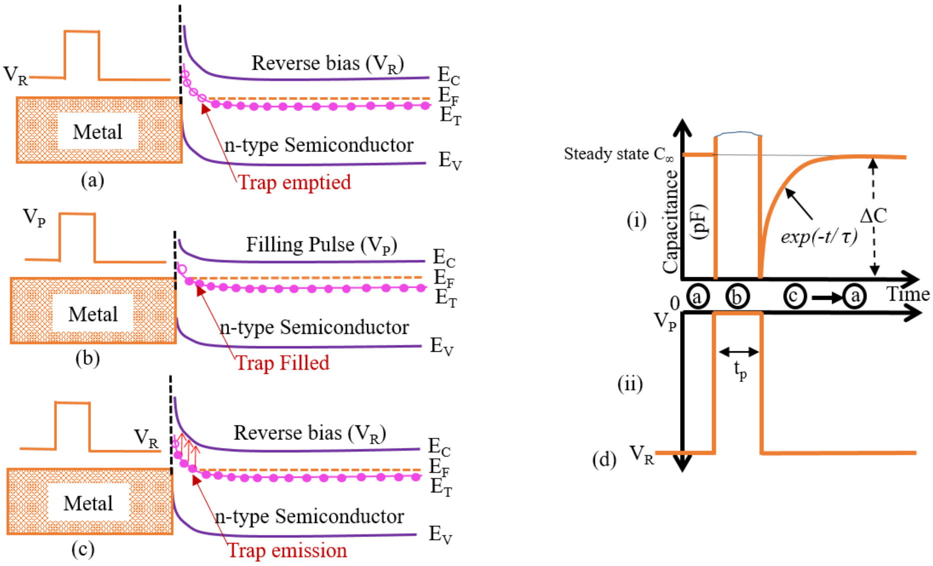

Fig. 4.7: The charge occupancy of deep level E_T is shown in a plot of energy band diagram of a Schottky junction as (a) emptying traps at steady applied reverse bias ($V=V_R$), (b) filling traps during filling pulse ($V=V_P$), (c) traps thermally emitting electrons at steady applied reverse bias ($V=V_R$) and (d) DLTS pulses and corresponding capacitance transient.

At first (Fig. 4.7 (a)), the device is under a steady reverse bias state, in which a depletion region is formed, and traps above the Fermi level are empty. Then, a filling pulse is applied (Fig. 4.7 (b)) with duration t_P which leads to the reduction of the width of the depletion region and hence allow the traps to capture electrons (filling traps). The rate at which the traps capture electrons is given by:

$$\frac{dn_T}{dt} = c_n(N_T - n_T) \tag{4.20}$$

where n_T, c_n and N_T are the number of trap states occupied by electrons, capture coefficient of the electrons, and the total number of available trap states. The capture coefficient of electrons (c_n) is given by the following equation:

$$c_n = \sigma_{\mathrm{n}} \langle v_{th} \rangle n \tag{4.21}$$

where σ_{n} and $\langle v_{th} \rangle$ are the capture cross-section and thermal velocity of electrons. $n = N_d - N_T \cong N_d$ is the effective doping concentration.

The reverse bias is then restored (Fig. 4.7 (c)) and the depletion region is back to its initial width (steady state). In this case, the traps start thermally emitting the electrons back and the corresponding emission rate is given by:

$$\frac{dn_T}{dt} = e_p N_T - (e_p + e_n) n_T \tag{4.22}$$

where e_p and e_n are hole and electron emission rates, respectively.

Assuming that the traps are electron interacting centres, the solution of Equation 4.20 (capture process) and Equation 4.22 (emission process) are given by exponential functions, as shown below [2]:

$$n_T = N_T(1 - exp(-c_n t)),\ c_n >> e_n, e_p \ and\ c_p \tag{4.23}$$

$$n_T = N_T\, exp(-e_n t) = N_T\, exp\left(\frac{-t}{\tau}\right),\ e_n >> c_n, e_p \ and\ c_p \tag{4.24}$$

where c_p is the hole capture coefficient and $\tau = \frac{1}{e_n}$ is the inverse of the electron emission rate (also known as the time constant of the carrier emission).

From the above equation, it is clear that the decrease in the filled trap concentration follows an exponential trend with a time constant τ and hence, this process leads to a capacitance transient as shown in Fig. 4.7 (d).

The occupancy change of trap can be measured indirectly by monitoring the change in capacitance. Thus, by adding the filled traps contribution, n_T in the space charge region, Equation 4.11, could be rewritten as:

$$C = \frac{dQ}{dV_R} = \frac{A}{2}\sqrt{\frac{2\varepsilon_s q N_d^*}{V_{bi}+V_R}} \tag{4.25}$$

where $N_d^* = N_d - n_T$

For $n_T <<$ $\mathrm{N_d}$, Equation 4.25 can be expanded as follows:

$$\Delta C = C_\infty(1 - \frac{n_T}{2N_d}) \tag{4.26}$$

where ΔC is the amplitude of the capacitance transient and $C_\infty = \frac{A}{2}\sqrt{\frac{2\varepsilon_s q N_d}{V_{bi}+V_R}}$ is the steady state capacitance.

From Equation 4.24 and 4.26, the following equation can be obtained to determine the time dependence of majority carrier traps:

$$\Delta C = C_\infty\left(1 - \frac{N_T}{2N_d} exp\left(\frac{-t}{\tau}\right)\right) \tag{4.27}$$

It is worth point out that the minority carrier traps can also be derived using the same process as majority carrier traps. However, for minority carrier traps, the capacitance transient is opposite to that of majority carrier traps.

4.4.2 CONVENTIONAL DLTS

The DLTS technique is based on the rate window concept, in which the capacitance of a Schottky diode or a p-n junction's depletion region is changed between two interval times, t_1 and t_2 ($t_1 < t_2$). The signal of DLTS is expressed as $S(T)$, which is basically the difference of capacitance ($\Delta C = C(t_1) - C(t_2)$) as a function of temperature, given by:

$$S(T) = \Delta C = C(t_1) - C(t_2) = \Delta C_o[exp^{(-e_n t_1)} - exp^{(-e_n t_2)}] \qquad (4.28)$$

Equation 4.28 can be rewritten using the inverse of emission rate (τ) as:

$$S(T) = \Delta C = C(t_1) - C(t_2) = \Delta C_o[exp^{\left(\frac{-t_1}{\tau}\right)} - exp^{\left(\frac{-t_2}{\tau}\right)}] \qquad (4.29)$$

where ΔC_o is the maximum change in the capacitance, which corresponds to the maximum amplitude of DLTS signal and is given by:

$$\Delta C_o = \frac{C_\infty N_T}{2N_d} \qquad (4.30)$$

It is worth noting that the trap concentration can be calculated using equation 4.30:

$$N_T = 2N_d \frac{\Delta C_o}{C_\infty} \qquad (4.31)$$

where N_T and C_∞ are the trap concentration and the capacitance at maximum reverse bias (the capacitance when a trap is completely empty), respectively. Equation 4.31 shows that the trap concentration is directly related to the peak amplitude of the DLTS signal.

In DLTS measurement, $S(T)$ will be maximum when $\tau \approx (t_1 - t_2)$. However, in the case of $\tau \gg (t_1 - t_2)$ or $\tau \ll (t_1 - t_2)$, the DLTS signal will be relatively small, as shown in Fig. 4.8 (a) [7]. The DLTS signal will reach a maximum when $\frac{dS(T)}{d\tau} = 0$ (see Equation 4.29) for:

$$\tau_{max} = \frac{t_2 - t_1}{ln(\frac{t_2}{t_1})} \tag{4.32}$$

Equation 4.32 is known as the rate window. By changing the values of $t_1$and t_2, the value of the rate window can be changed. Using different rate windows will produce different peaks in the DLTS spectra at different temperatures as shown in Fig. 4.8 (b). The trap activation energy is calculated using an Arrhenius plot of the emission rates (from DLTS peaks) as a function of temperature, as depicted in Fig. 4.8 (c). Furthermore, the activation energy can be extracted from the slope of the Arrhenius curve, and the apparent capture cross-section can be calculated from the y-intercept. Equations 4.29 and 4.32 demonstrate that the DLTS signals are reliant on the ratio between $(\frac{t_2}{t_1})$ but not on the absolute values of $t_1$and t_2 .

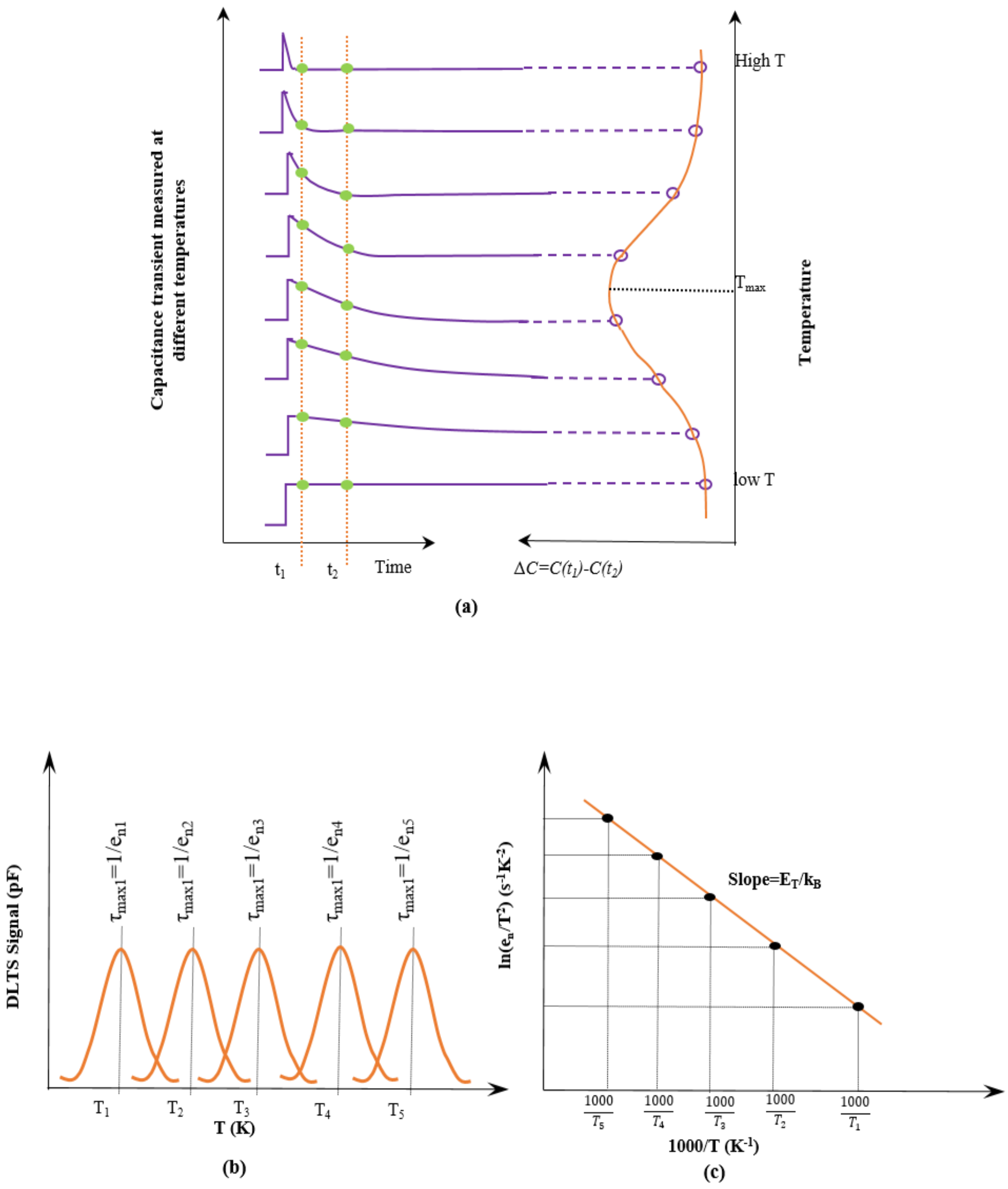

Fig. 4.8: schematics diagrams illustrating (a) the generation of DLTS peaks for one rate window, (b) DLTS peaks for different rate windows and (c) Arrhenius plot obtained from different rate windows [8].

4.5 LAPLACE DLTS SPECTROSCOPY

DLTS is a powerful tool for the investigation of deep-level defects, but it has some drawbacks. For instance, DLTS is a thermal scanning technique and therefore it is difficult to measure the sample temperature accurately during the scan. Since the temperature of the sample is continuously increased or decreased, the activation energy of traps cannot be obtained with high accuracy. Another disadvantage is the poor resolution of the time constant, meaning that conventional DLTS is unable to separate closely spaced defects that have similar emission rates. This poor resolution results is reflected in the broad peaks observed in standard DLTS spectra [9]. A more advanced variant of DLTS, namely the Laplace DLTS method, is used to overcome the limitations of conventional DLTS. Laplace DLTS is an isothermal technique, where during the measurements, the diode is kept at a constant temperature. In Laplace DLTS, the quantitative description of the capacitance transients uses a mathematical approach given by:

$$f(t) = \int_0^\infty F(s) e^{-st} ds \tag{4.33}$$

where $f(t)$ and $F(s)$ are the recorded transient and the spectral density function, respectively. Equation 4.33 expresses the transient capacitance as the Laplace transform of the actual spectral density function $F(s)$. Fig. 4.9 (a) shows the capacitance transient obtained from Laplace DLTS. The real spectrum of emission rates within the transient is obtained by applying an appropriate mathematical algorithm which performs an inverse Laplace transform for the recorded transient $f(t)$ [10]. The Laplace DLTS technique employs three main algorithm routines, i.e. FLOG, CONTIN and FTIKREG, to solve Equation 4.33 [11]. A spectrum of delta-like peaks is obtained as a result of using these algorithms, as shown in Fig. 4.9 (b).

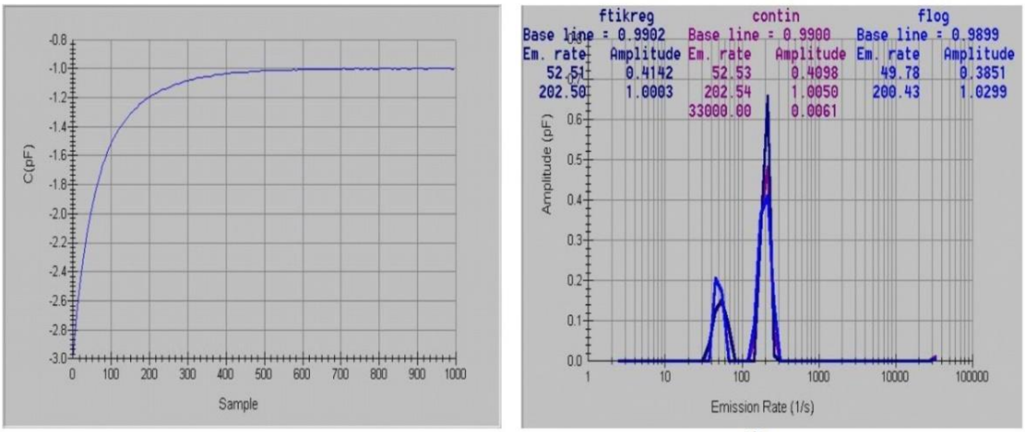

ftikreg		contin		flog	
Base line = 0.9902		Base line = 0.9900		Base line = 0.9899	
Em. rate	Amplitude	Em. rate	Amplitude	Em. rate	Amplitude
52.51	0.4142	52.53	0.4098	49.78	0.3851
202.50	1.0003	202.54	1.0050	200.43	1.0299
		33000.00	0.0061		

(a) (b)

Fig. 4.9: (a) Laplace DLTS capacitance transient and (b) a spectrum of delta-like peaks [8,12].

4.6 DLTS HARDWARE SETUP

The main experimental setup utilised for conventional DLTS and Laplace DLTS measurements is covered in this section. The DLTS system includes the following equipment:

I. A Janis cryostat.
II. Temperature controller.
III. Capacitance meter (Boonton 7200).
IV. Current-voltage source meter (Keithley).
V. Data acquisition and BNC connector box for analogue Input (I)/Output (O).

All these equipment are controlled via a computer through a GPIB interface. Fig. 4.10 shows an experimental photograph of the DLTS system. The block diagram of the DLTS configuration is shown in Fig. 4.11.

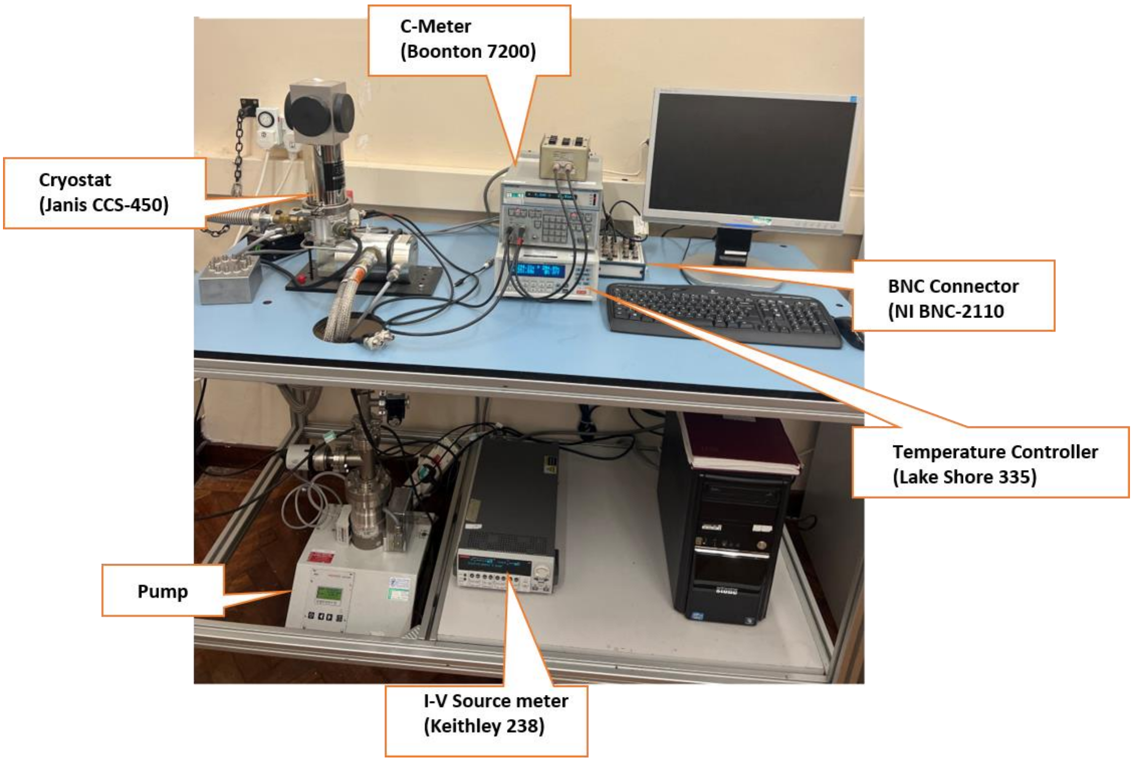

Fig. 4.10: Photograph of the DLTS system used in this thesis.

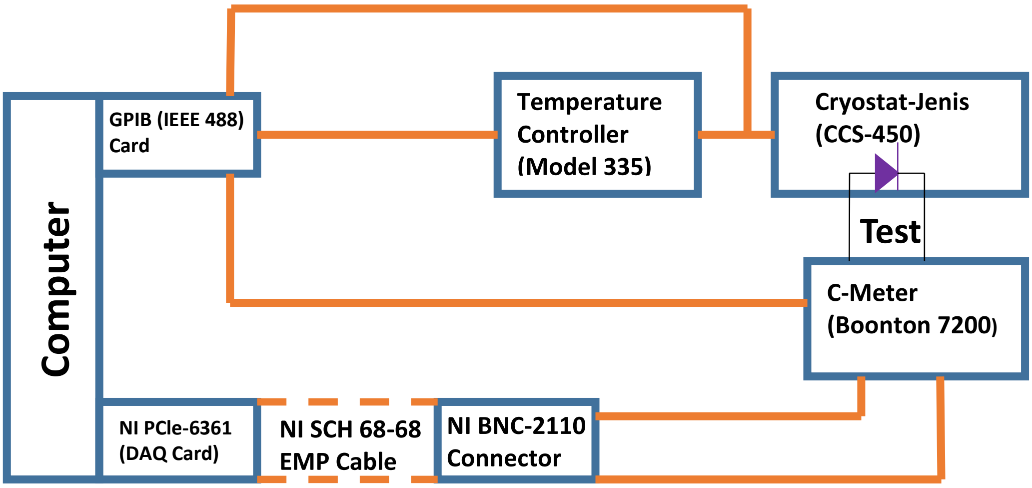

Fig. 4.11: Schematic diagram of the DLTS system.

4.6.1 CRYOSTAT AND TEMPERATURE CONTROLLER

One of the most important factors in the DLTS measurement is to measure the temperature of the sample accurately because the emission of carriers from energy levels depends on the temperature. Therefore, to control the temperature of the sample, a cryostat JANIS CCS-450 and a temperature controller Lake Shore 335 models are used. The cryostat is based on a helium (He) closed-loop refrigeration system, where a high efficient and flexible six feet cryogen transfer line is used for the flow of Helium. The cryostat can operate over a temperature range from 10 to 500K with a stability of ±1K. Fig. 4.12 shows a picture of the cryostat which comprises the following components:

I. Lightweight aluminium vacuum shroud.
II. Radiation shield.
III. A cold finger attached to a sample holder.
IV. Electrical ports for sample contacts.

It is important to point out that, to monitor accurately the temperature of the sample, an additional temperature sensor is situated very close to the sample.

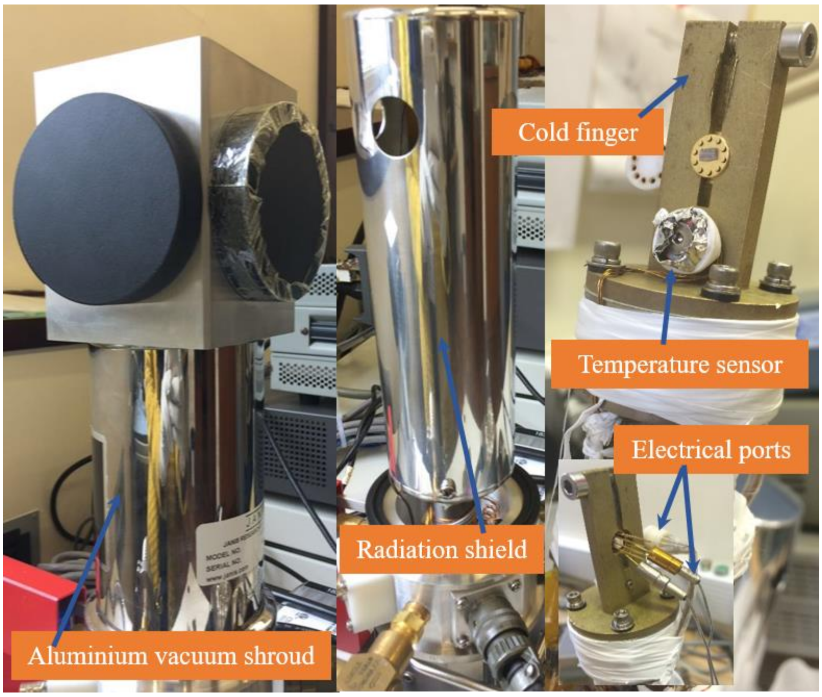

Fig. 4.12: Photograph of the JANIS CCS-450 cryostat.

4.6.2 CAPACITANCE METER

The capacitance transient measurements require a capacitance meter with a high response time. Thus, the Boonton 7200 meter was employed, which has a response time of ~120µs. Furthermore, this capacitance metre is utilised to do standard C-V measurements at various temperatures. It is worth noting that the sampling frequency is 1 MHz.

4.6.3 CURRENT-VOLTAGE SOURCE METER

In order to determine the diode parameters such as ideality factor (n), barrier height (ϕ_B) and series resistance (R_s), I-V measurements were performed on each sample at different temperatures. In addition, I-V characteristics were obtained to determine the suitability of samples for DLTS and Laplace DLTS measurements, which require low reverse currents in the range of µA. The I-V measurements were performed using Keithley 236 current source meter. It has a source voltage ranging from 100 μV to 110 V with a sensitivity of ±10 μV, as well as a source current in the range of 100 fA to 100 mA with a sensitivity of 10 fA.

4.6.4 DATA ACQUISITION AND BNC CONNECTOR BOX

Data acquisition card (DAQ) is an important part of the DLTS technique, since it is used to bias and pulse the diodes. This is accomplished via a National Instruments (NI) PCIe-6321 card, which has a ±10 V input voltage and a pulse width ranging from 0.5 μs to 50 s. A BNC-2110 connector box is needed to collect and send data from the diodes to the computer, where it is processed. The (NI) PCIe-6321 card is connected to the BNC-2110 connector box using a SHC68-68-EPM matching cable.

4.6.5 COMPUTER INTERFACE

A general-purpose interface bus (GPIB) is utilised to provide high-speed communication between all the experimental equipment described above and the computer. The GPIB connectors enable all the equipment to be controlled remotely through the software.

4.7 SYSTEM SOFTWARE

Laplace DLTS software was developed by a joint project ***“Copernicus Project CIPA CT-94-0172 and The Foundation for Polish Science Serial No: C3.2.041”*** between the University of Manchester, Manchester, United Kingdom (Professor A. R. Peaker) and Institute of Physics of the Polish Academy of Sciences, Warsaw, Poland (the late Professor L. Dobaczewski). This software runs in two modes, i.e. the regular conventional DLTS and Laplace Transient (Laplace DLTS) modes.

4.7.1 CONVENTIONAL DLTS MODE

In DLTS mode, three different types of procedures can be used to perform conventional DLTS measurements. Multi-Rate Window, TrapView and Exponential Fitting, which all use the rate window concept. In each of these three processes, the sample temperature is scanned in steps, typically 2 K/minutes, from the set point to the end point.

In the Multi-Rate Window mode, nine different rate windows are recorded simultaneously, resulting in nine different DLTS signals being generated. The different rate windows used are 5, 10, 20, 50, 100, 200, 500, 1000 and 2000 s^{-1}. These were determined by changing the value of t_1 and t_2 .

In TrapView, a pair of rate windows must be selected between five different pairs, i.e. (4, 10 s^{-1}), (20, 50 s^{-1}), (80, 200 s^{-1}), (400, 1000 s^{-1}) and (2000, 5000 s^{-1}).

In Exponential Fitting, only one rate window could be chosen for a single scan from the available rate windows (10, 20, 50, 100 and 200 s^{-1}). However, for this mode, the lock-in mode can be selected instead of the rate window mode. Lock-in mode has a better resolution when compared to rate window mode but also has a poor signal to noise ratio. In addition, the Arrhenius plot can be generated during the temperature scan and the traps activation energies can be estimated.

Note that in all mentioned modes, DLTS parameters can be set remotely, such as reverse bias and the amplitude and width of filling pulse.

4.7.2 LAPLACE TRANSIENT PROCESSING MOTHOD

Laplace (LDLTS) is an extension method to DLTS technique known as high resolution Laplace transform. In addition, the LDLTS is an isothermal method which digitises and averages capacitance transients at a given fixed temperature. This method is used to increase the signal to noise ratio. The Laplace DLTS peaks are generated using three different algorithms.

4.8 PHOTOLUMINESCENCE

Photoluminescence (PL) is a type of luminescence emitted from a material that is not heated. PL is the emission of light due to photon absorption. In this section, PL spectroscopy, which is a powerful non-destructive technique for studying the optical properties of semiconductor materials [2], will be discussed.

The investigated sample is subjected to a light source such as a laser with an energy $h\nu$ greater than the material bandgap E_G. The light from the laser source (photons) is absorbed and the excess energy is transferred to the material in a process known as photo-excitation. The material will then emit the excess energy in the form of light known as photoluminescence. The PL spectrum's intensity and the spectral content is used to obtain important information about the material properties, such as the bandgap, the presence of impurity levels and the quality of the material.

In the photo-excitation process, the electrons are excited to higher states and subsequently relax back to their equilibrium states by losing an energy corresponding to the difference in energy between the excited and equilibrium states in the form of light in a process known as radiative recombination. However, a non-radiative process occurs when the difference in the energy is lost as heat.

Fig. 4.13 shows the excitation of electrons, in which non-equilibrium electrons tend to relax back into the equilibrium state (relaxation within bands to the edge of the energy band), and finally emit light due to an electron-hole radiative recombination.

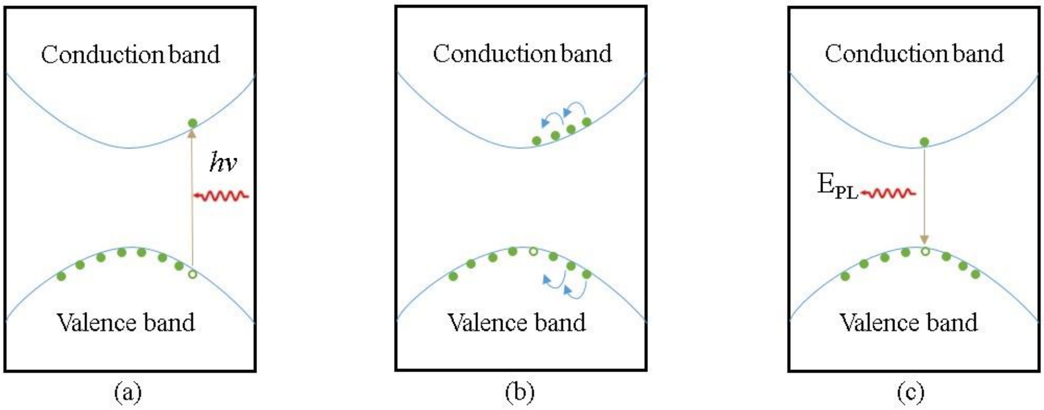

Fig. 4.13: Illustration of the processes involved in PL (a) photo-excitation from the valence band to the conduction band, (b) intra-band relaxation and (c) recombination, which leads to PL emission [8].

It is worth to point out that the PL technique does not require any sample preparation or electrical contacts. Therefore, PL can be used to study samples with high resistivity. Another advantage of the PL is that the luminescence can be measured in various parts of the sample's surface to determine uniformity of the optical response and therefore the sample homogeneity.

4.9 SYSTEM HARDWARE IMPLEMENTATION

This section describes the hardware of the PL system, which operates over a temperature range of 10K - 300K.

The block diagram and photographs of the PL system used in these investigations are shown in Figures 4.14, 4.15, 4.16 and 4.17. Below are descriptions of several key components of the PL system.

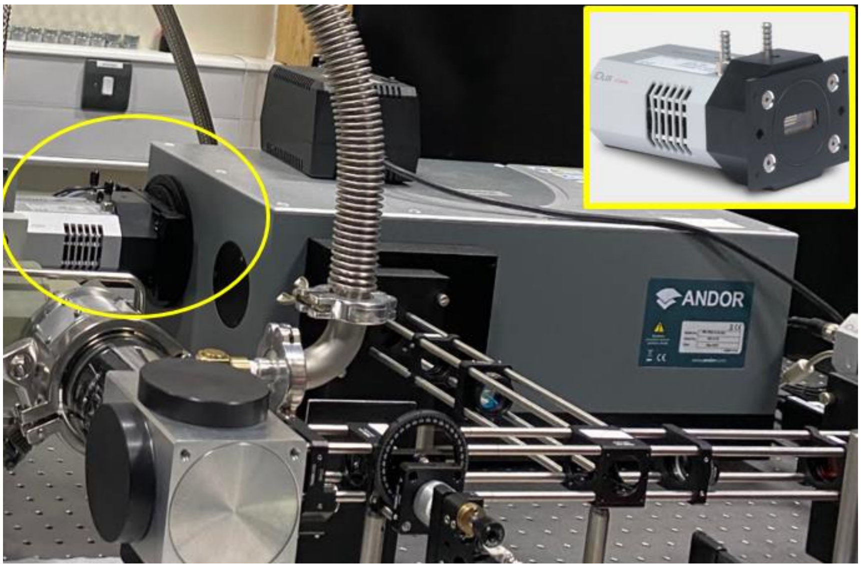

Fig. 4.14: Photograph of the Andor Shamrock 500i spectrometer and InGaAs CCD camera.

4.9.1 SPECTROMETER AND DETECTORS

To allow spectral investigation, the produced photoluminescence was scattered using a grating spectrometer. The spectrometer utilised in this study is 500i spectrometer from Andor. It has a focal length of 500 mm and an aperture of F/6.5. The Shamrock 500i has a unique triple grating turret that allows to select gratings easily. The triple grating turret can be quickly and simply removed or replaced by alternative turret with new gratings. The gratings is interchangeable indexed triple turret with three distinct gratings (300 grooves/mm blazed at 3000 nm, 600 grooves/mm blazed at 2000 nm, and 1200 grooves/mm blazed at 500 nm). The width of the entry and exit slits can be adjusted manually or remotely from 10 µm to 2.5 mm. The CCD camera detector fitted in the spectrometer exit port converts incident photons to electronic signals, allowing it to cover a wide range of wavelengths. The InGaAs and Si CCD detectors employed in the PL system have great sensitivity and can cover the optical wavelength ranges ~600nm-1.7µm and 300nm-1000nm, respectively (see Figure 4.15). The InGaAs detector was employed in this experiment.

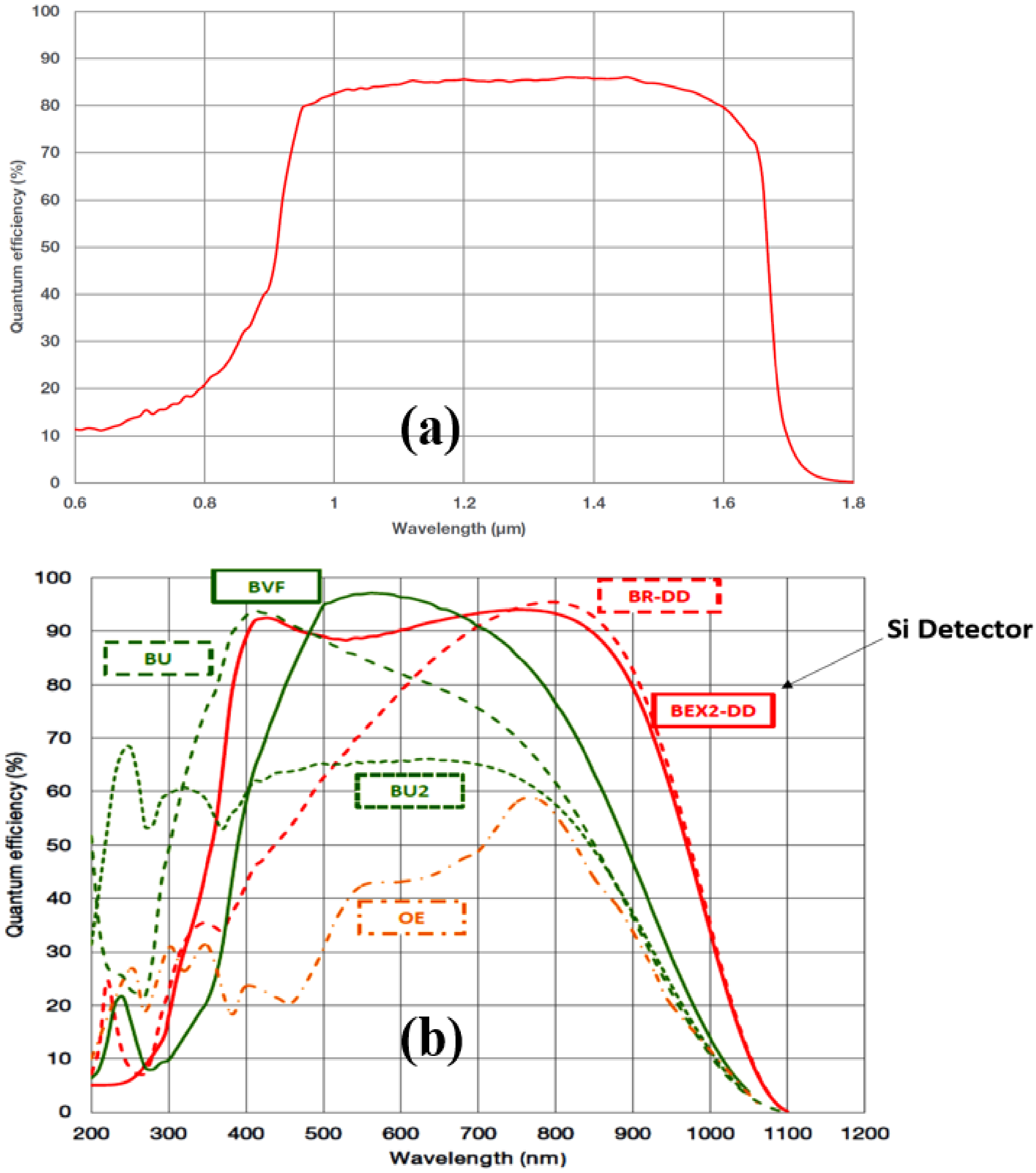

Fig. 4.15: The efficiency response curves of (a) InGaAs CCD detector and (b) Si CCD detector.

4.9.2 LASERS AND OPTICS

The PL system comprises three lasers to excite the samples, primarily blue, green and red lasers with wavelengths 473 nm, 532 nm and 655 nm, respectively. The laser power incident on the sample is controlled manually using a natural density filter. A beam splitter is used to shine the laser on the sample and direct the PL signal to the appropriate spectrometer (one fitted with an InGaAs CCD and the other with a Si CCD). In addition, a long pass filter is installed in front of each monochromator entrance slit to eliminate undesirable high-order lines of the laser light. The PL setup also includes a number of optics, such as lenses and mirrors, to focus the PL signal on the entry slit of the selected spectrometer and the laser light onto the sample. Fig. 4.16 depicts the setup configuration of the PL system used in this thesis.

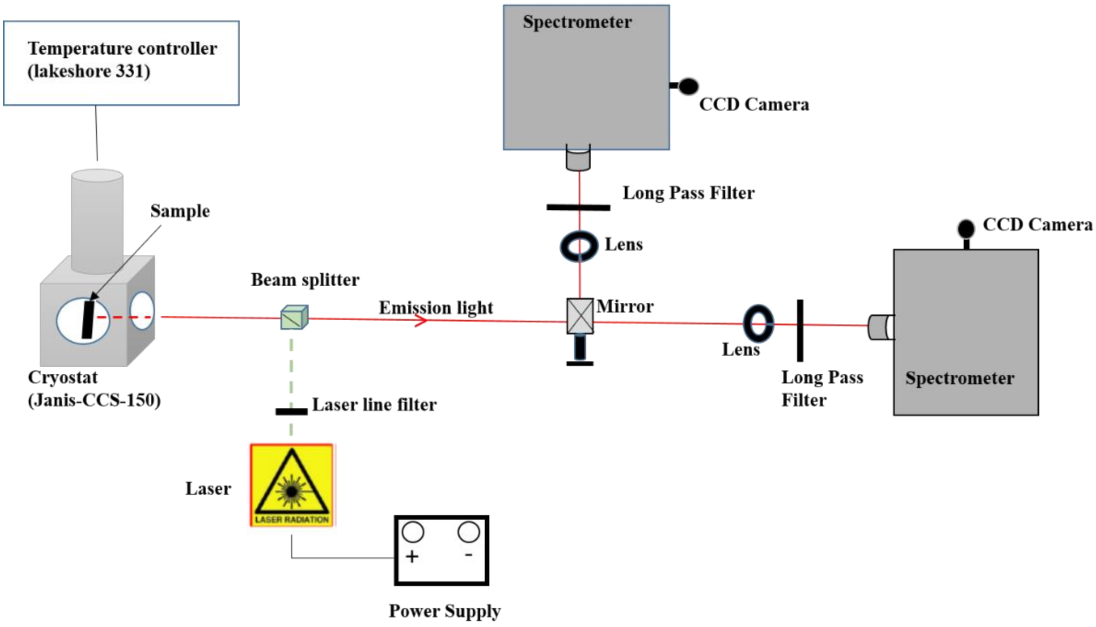

Fig. 4.16: A schematic diagram of the photoluminescence (PL) apparatus.

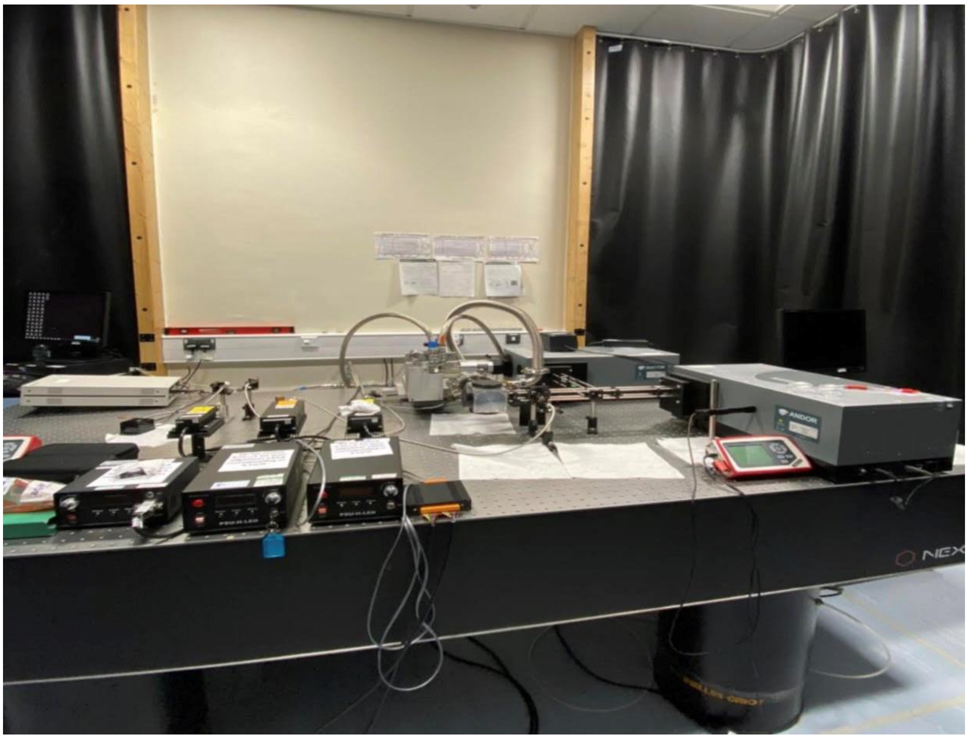

Fig. 4.17: Photograph of the Photoluminescence (PL) apparatus.

4.9.3 CRYOSTAT AND TEMPERATURE CONTROLLER

For the temperature dependent PL measurements in the range10K - 300K, a state-of-the-art Janis CCS-150 cryostat and a temperature controller, model Lake Shore 331, were employed. The refrigeration principle of the cryostat is based on a closed-cycle flow of helium gas (He) through a compressor. It is similar to the one discussed in section 4.6.1, and also includes temperature sensors, radiation shields, and specially designed sample holder.

4.9.4 COMPUTER INTERFACE

The spectrometer and CCD cameras are interfaced with a computer using Windows 10 through USB ports.

4.9.5. SYSTEM CONTROLLING SOFTWARE

Solis Andor’s CCD cameras and spectrometer system control software is used to remotely control the various elements of the PL system. It has a number of features for data acquisition as well as monitoring and controlling the various PL system components. The software can, for example, control the turret's three gratings, the size of the entrance and exit slits, and shutters.

REFERENCES

[1] C.A. Colinge, J. P., & Colinge, *Physics of semiconductor devices.*(springer science & Business Media, 2005).

[2] D. K. Schroder, *Semiconductor materials and devices characterization*. (John Wiley & Sons, 2006).

[3] S.M. Sze, K.K. Ng, *Physics of Semiconductor Devices*. (John Wiley & Sons, 2006).

[4] Donald A. Neamen, *Semiconductor Physics and Semiconductor Devices*. (McGraw-Hill New York, 2012).

[5] Sze, S. M., and M. K. Lee , *Semiconductor Devices. Physics and Technology*. (John Wiley & Sons, Singapore Pte. Ltd, 2013).

[6] J.H. Werner, *Schottky barrier and pn-junctionI/V plots-Small signal evaluation*, Appl. Phys. A. **47**, 291 (1988).

[7] D. V. Lang, *Deep-level transient spectroscopy: A new method to characterize traps in semiconductors*, J. Appl. Phys. **45**, 3023 (1974).

[8] F. AlMashary, *Investigation of the Electrical Properties of Transparent Conductive Oxides Thin Semiconductor Films Grown by Various Techniques*. (University of Nottingham, 2019).

[9] L. Dobaczewski, I.D. Hawkins, A.R. Peaker, *Laplace transform deep level transient spectroscopy: new insight into defect microscopy*, Mater. Sci. Technol. **11,** 1071 (1995).

[10] L. Dobaczewski, P. Kaczor, I.D. Hawkins, A.R. Peaker, *Laplace transform deep-level transient spectroscopic studies of defects in semiconductors*, J. Appl. Phys. **76,** 194 (1994).

[11] L. Dobaczewski, A.R. Peaker, K. Bonde Nielsen, *Laplace-transform deep-level spectroscopy: The technique and its applications to the study of point defects in semiconductors*, J. Appl. Phys. **96**, 4689 (2004).

[12] M. Shafi, *Electrical and Optical Studies of Dilute Nitride and Bismide Compound Semiconductors*. (University of Nottingham, 2010).

CHAPTER 5: EXPERIMENTAL DETAILS

This chapter's objective is to provide a brief overview of the structure of the samples investigated in this thesis. In addition, a brief description of the experimental setup and equipment utilised for electrical and optical characterisation will be presented.

5.1 SAMPLES INVESTIGATED IN THIS STUDY

The main motivation of this thesis is to investigate the optically and electrically active defects present in dilute GaAsBi based structures and devices.

The samples were grown in an MBE system, which is equipped with standard effusion cells, at the Lebedev Physical Institute (Moscow, Russia). For the evaporation of Bi, a standard Ga furnace with reduced screen insulation was used to improve temperature control. n-type and p-type GaAsBi epilayers have been studied using different techniques. The samples details are given below:

(i) For n-type GaAsBi layers, the samples consisted of a 100 nm thick doped GaAs buffer layer (n = ~2-3 x 10^{18} cm^{-3}) followed by 1 µm thick doped $GaAs_{(1-x)}Bi_x$ layer (n-type = 2 x 10^{16} cm^{-3}) grown on (100) and (311)B oriented n^+-GaAs substrates. Si was used as n-type dopant. GaAs control samples not containing Bi and with similar layer structure were also grown under the same growth conditions as those of n-type GaAsBi for comparison purposes. In addition, (100) as-grown dilute GaAsBi samples were irradiated with a gamma cell Cobalt Irradiator (dose rate of 1.3 kGy/h) at different doses of 50 and 100 kGy to investigate the effect of gamma radiation dose on the electrical and optical properties of dilute GaAsBi.

(ii) For p-type structures, the samples consisted of a 100 nm thick doped GaAs buffer layer (p = ~2-3 x 10^{18} cm^{-3}) followed by 1 µm thick doped $GaAs_{(1-x)}Bi_x$ layer (p-type = 2 x 10^{16} cm^{-3}) grown on (311)B oriented semi-insulating GaAs substrates. Be was used as p-type dopant. The respective p-type GaAs control samples were grown without Bi and under the same growth conditions as those of p-type GaAsBi for comparison purposes

The growth conditions of these samples are detailed in each associated experimental chapter.

5.2 MEASUREMENT DETAILS

This section describes the experimental setup and equipment used for the characterisation of the samples.

5.2.1 I-V MEASUREMENTS

The conventional DLTS and Laplace DLTS measurements, which are primarily based on transient of capacitance, require devices with low leakage currents in the range of µA or below. Therefore, all samples are tested for suitabilty to avoid erroneous results. In addition, the I-V characteristics of the devices are measured using Keithley 236 source measure unit, which is controlled via GPIB interface by computer software. The current values are measured at various reverse bias voltages (V_R) with increment of 0.01 V. The maximum value of V_R depends on the Schottky diodes. Additionally, the I-V characteristics as a function of temperature were obtained to determine the diode parameters, as discussed in Chapter 4.

5.2.2 C-V MEASUREMENTS

The C-V measurements were performed at a fixed frequency of 1 MHz for all Schottky diode devices using a Boonton 7200 capacitance meter in order to obtain the background doping concentration, depletion width, and also to calcuate the trap concentration. These important parameters are used in the analysis of DLTS characteristcs.

5.2.3 DLTS MEASUREMENTS

The DLTS and Laplace DLTS techniques, which are explained extensively in Chapter 4, are used to characterise the electrically active defects present in the material systems studied in this thesis. In this section, a brief overview of the experimental methodologies is given. Firstly, the samples were processed into circular mesas of various diameters (200 to 1000µm), and mounted on 10 pins TO5 headers. These were then placed on a holder inside a He closed-loop cycle cryostat, model JANIS CCS-450. The samples were then cooled down to a temperature of 10K. The DLTS measurements began by ramping the temperature up to 450K at a rate of 2K/min and subjecting the samples to a sequence of electrical pulses generated by a pulse generator (National Instrument Box). The resulting capacitance transient was measured with a Boonton 7200 capacitance meter. The change in capacitance transient as a function of temperature is captured in the form of a DLTS signal, and stored in the computer at selected reverse bias voltages (V_R) and filling pulse (V_P).

5.2.4 LAPLACE DLTS MEASUREMENTS

High Resolution Laplace DLTS measurements were used to reslove the broad featureless DLTS peaks. Since Laplace DLTS is an isothermal DLTS procedure, measurements were carried out at a constant temperature within a temperature range where a conventional DLTS peak was present. Further details of these measurements are explained in Chapter 4.

5.2.5 PHOTOLUMINESENCE (PL) MEASUREMENTS

In this study, PL technique was used to study the optical properties of the samples, which were mounted in a closed cycle Helium-cooled cryostat operating in the temperature range 10K to 300K. The samples were excited with a green laser having wavelength equal to 532 nm (~2.33 eV). The dectector used in this experiment is an InGaAs CCD, which covers visible (~600nm) to mid-infrared (1700nm).

5.2.6 XRD AND RAMAN MEASUREMENTS

X-ray diffraction (XRD) measurements were carried out in a Rigaku Smartlab diffractometer using Cu Kα1 radiation in collaboration with Prof. Igor Kazakov’s group at Lebedev Physical Institute (Moscow, Russia). High quality double-crystal Ge (220) was used as collimator. The XRD rocking curves were measured using 2θ-ω scans with a horizontal slit positioned in front of the detector in order to minimize diffuse and background scattering.

Micro-Raman measurements were performed in collaboration with Prof. Yara Gobato’s group at Federal University of Sao Carlos using a 633 nm laser excitation.

The Raman signal was measured in a Lab RAM HR system from Horiba Jovin Yvon that has 50x objective with spectral resolution of about 1 cm^{-1}.

CHAPTER 6: INVESTIGATION OF THE EFFECT OF SUBSTRATE ORIENTATION ON THE STRUCTURAL, ELECTRICAL AND OPTICAL PROPERTIES OF N-TYPE $GaAs_{1-X}Bi_X$ LAYERS GROWN ON (100) AND (311)B GaAs SUBSTRATES BY MOLECULAR BEAM EPITAXY

Current-Voltage (I-V), Capacitance-Voltage (C-V), Deep Level Transient Spectroscopy (DLTS), Laplace DLTS, Photoluminescence (PL) and Micro-Raman techniques have been employed to investigate the effect of the orientation of the substrates on the structural, electrically and optically active defects in dilute $GaAs_{1-x}Bi_x$ epilayers structures having a Bi composition x = ~5.4%, grown by Molecular Beam Epitaxy (MBE) on (100) and (311)B GaAs planes. X-ray diffraction results revealed that the in-plane strain in the GaAsBi layer of the samples grown on (100)-oriented substrate (-0.0484) is significantly larger than that of the samples grown on (311)B-oriented substrate (-0.0183). The substrate orientation is found to have a noticeable impact on the Bi incorporation and the electrical properties of dilute GaAsBi Schottky diodes. The I-V characteristics showed that (100) Schottky diodes exhibited a larger ideality factor and higher barrier height compared with (311)B samples. The DLTS measurements showed that the number of electrically active traps were different for the two GaAs substrate orientations. In particular, three and two electron traps are detected in samples grown on (100) and (311)B GaAs substrates, respectively, with activation energies ranging from 0.12 to 0.41 eV. Additionally, one hole trap was observed only in sample grown on (100) substrates with activation energy of 0.24 eV. The observed traps with small activation energies are attributed to Bi pair defects. PL and Raman spectra have evidenced different compressive strain which affects considerably the optical properties. Furthermore, the PL spectra were also affected by different contributions of Bi-related traps which are different for different substrate orientations in agreement with DLTS results.

6.1 INTRODUCTION

Dilute III-V bismide semiconductors materials such as GaAsBi alloys display strong reduction in the band gap when only a small percentage of bismuth atoms is incorporated into the lattice of the host material like GaAs which has a band gap energy of 1.424 eV at 300K. Particularly, a few percent of Bi incorporated into GaAs, i.e. $GaAs_{1-x}Bi_x$ with x being the Bi composition, leads to a giant bowing in the band gap energy (~ 88 meV/%Bi) [1], as well as an increase in spin-orbit splitting energy [2, 3]. These remarkable properties such as reduction of the band gap make GaAsBi a suitable material for several device applications such as multi-junction solar cells [4], photonic devices [1] and long-wavelength optoelectronic devices [5].

It is well known that the growth temperature of III-V alloys can significantly influence their crystalline quality. In fact, substitutional incorporation of Bi into the host lattice of III-V compounds requires low temperature growth (< 400 ℃). However, low growth temperature of GaAs causes an increased density of defects as well as leads to degradation of the optical quality of alloys [6]. For instance, growing GaAs at temperatures lower than the optimal growth temperatures (~580-600℃) leads to the creation of many point defects, such as As-antisites (As_{Ga}), As-interstitials (As_i) and Ga vacancies (V_{Ga}) [7–9]. Additionally, it is found that as the growth temperature decreases, deep level defects are generated in GaAs and their concentrations are enhanced [7, 10]. Nevertheless, using Bi as a surfactant during the growth of GaAs at low temperatures has proven to enhance surface migration, reduce the density of defects and suppress the formation of traps in GaAs. However, in GaAsBi epilayers where Bi is substituting an arsenic atom, Bi related defects are created. Recently, DLTS and Laplace DLTS (LDLTS) studies of n-type $GaAs_{1-x}Bi_x$ layers grown by MBE on n^+ GaAs substrates with $0 \leq x \leq 0.012$ [11] have shown that a significant reduction of the total traps concentration by a factor of ~20, in contrast to GaAs layers grown at similar temperature (~330 °C). Furthermore, as anticipated for MBE growth at this temperature, the dominant deep level defect in these layers were proposed to be an As_{Ga}-related complex defect, with a deep level energy of about 0.65 eV [11]. More recently, Ł. Gelczuk et al. [7] employed DLTS to investigate the electron deep level defects in n-type $GaAs_{1-x}Bi_x$ alloys having $0<x<0.023$ grown by MBE on conventional (100) n^+ GaAs substrates. They found that the incorporation of Bi into GaAs suppresses the formation of electron traps by reducing their total trap concentrations to more than two order of magnitude compared to trap concentrations in GaAs grown at similar conditions. Additionally, they reported that the two levels with activation energies ranging from 0.07 to 0.19 eV in GaAsBi with Bi compositions of 0.8%- 2.3%, are Bi- related traps. They suggested the origin of these defects to be related to Bi pair defects [7].

Although most investigations of $GaAs_{1-x}Bi_x$ thin films and devices were performed using the conventional (100) GaAs substrates, there are few studies exploring the growth on high-index planes, which can considerably affect the Bi incorporation, and the structural, electrical and optical properties [12–16].

Remarkably, Henini et al have shown that Bi incorporation in $GaAs_{1-x}Bi_x$ thin films can be more enhanced by using (311)B GaAs orientation [12]. In addition, there are relatively very few researches which addressed the doping process of only (100) $GaAs_{(1-x)}Bi_x$ [7,10,11,17–20]. Therefore, it is worth noting that the structural and optical properties of n-type $GaAs_{1-x}Bi_x$ alloys and devices using non-(100) GaAs substrates have not been investigated yet.

In this work the effects of substrate orientation on the structural, optical and electrical properties of n-type dilute $GaAs_{1-x}Bi_x$ epilayer structures grown at low temperature by MBE on conventional (100) and non-conventional (311)B n^+ GaAs substrates were investigated using I-V, C-V, DLTS, LDLTS, PL and Micro- Raman techniques.

6.2 EXPERIMENTAL DETAILS

The samples studied in this work were silicon-doped n-type $GaAs_{1-x}Bi_x$ epilayers grown on highly doped (100) and (311)B n^+ GaAs substrates by MBE at low temperature (~400°C). Fig. 6.1 shows a schematic diagram of the epitaxial layers structure which consisted of 0.1 µm thick GaAs buffer layer heavily doped with Si with a concentration of $2x10^{18}$ cm^{-3}. This was followed by 1 µm thick Si doped GaAsBi layer with a Si concentration of $2x10^{16}$ cm^{-3}. Additionally, similar structures (control samples) consisting of a 1 µm thick n-type GaAs layer (not containing Bi) were grown on (100) and (311)B GaAs substrates at similar conditions, for comparison purposes. Two n-type $GaAs_{1-x}Bi_x$ epitaxial layers with ~5.4% of Bi were examined (see Table 6.1).

The Bi compositions of the $GaAs_{1-x}Bi_x$ epilayer were measured by XRD. For electrical characterization of these devices, all samples have been fabricated in form of circular mesas. Ge/Au/Ni/Au Ohmic contacts were thermally evaporated on the back side of the wafer, with thickness (10, 20, 20 and 150) nm, respectively. Then rapid thermal annealing (RTA) in an Ar atmosphere was performed at 380°C for 30 seconds. This was followed by Au deposition through a shadow mask to form circular mesas Schottky contacts with different diameters on the top side of the samples. PL spectra of (100) and (311)B $GaAs_{(1-x)}Bi_x$ samples were investigated as a function of laser power and temperature using a Janis closed-loop helium cryostat. The samples were excited with a 532 nm Nd:YAG solid state laser. The PL signal was collected in a 0.5 m Spex monochromator coupled with a nitrogen-cooled Ge detector. Micro-Raman measurements were carried out with a 633nm laser excitation. The Raman signal was measured in a Lab RAM HR Horiba Jobin Yvon system with 50x objective with spectral resolution of about 1 cm^{-1}.

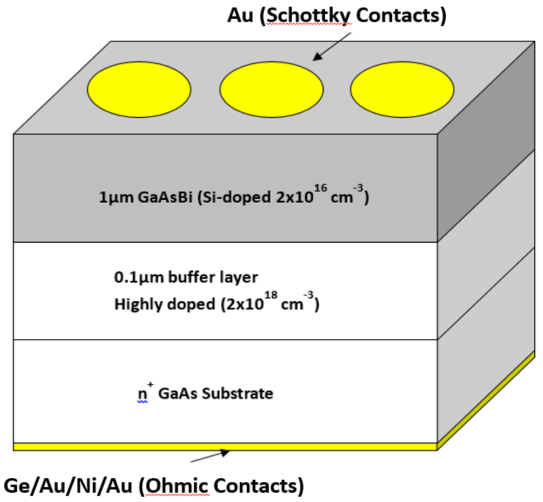

Fig. 6.1: Schematic diagram of n-GaAsBi structure grown on (100) and (311)B n^+ GaAs substrates.

Table 6.1. Samples details: substrate orientation, Bi content obtained from XRD and doping concentration as determined from C-V measurements.

Sample	Substrate orientation	Bi content (from XRD) (%)	Doping Concentration (Nd)
n-GaAs	(100)	0	$3.80\text{x}10^{17}$ cm^{-3}
n-GaAs	(311)B	0	$3.40\text{x}10^{17}$ cm^{-3}
n-GaAsBi	(100)	5.4	$1.03\text{x}10^{16}$ cm^{-3}
n-GaAsBi	(311)B	5.4	$1.14\text{x}10^{16}$ cm^{-3}

6.3 RESULTS AND DISCUSSION

6.3.1 STRUCTURAL CHARACTERISTICS

X-ray diffraction measurements were carried out on a Rigaku Smartlab laboratory diffractometer in the 2θ-ω mode using Cu-$K_{\alpha 1}$ radiation and a double-crystal Ge (220) monochromator with a horizontal slit positioned in front of the detector in order to reduce diffuse and background scattering. XRD curves were measured in θ-2θ scanning mode [21]. The X-ray spot on the sample's surface was about 5mm^2 x 0.4 mm^2. The structure parameters were determined from XRD curves using different (symmetrical and asymmetrical) experimental schemes. Typical XRD curves are shown in Fig. 6.2 and Fig. 6.3 for the (311)B and (100) GaAsBi samples, respectively. In Fig. 6.2 where symmetrical (311) and two asymmetrical (400) diffraction patterns are presented for the (311)B GaAsBi samples. Out-of-plane lattice parameter was obtained from the analysis of symmetrical XRD curves. For (100) GaAs and (311)B GaAs oriented surfaces, the asymmetric reflections (311) and (400) were measured, respectively. Asymmetrical reflections were chosen based on the relative intensity (relationship between incident X-ray radiation and the reflected one).

Asymmetrical reflections were measured from a set of planes with an angle less than the Bragg angle (θ_B) for these planes. The incidence angles θ_{asym} for these reflections are given by $\theta_{asym} = \theta_B \pm \varphi$, where φ is the angle between asymmetrical planes and surface of the sample. Knowing the out-of-plane lattice parameter and the angle between asymmetrical reflected plane and the planes parallel to the surface of the sample, the in-plane lattice parameter of epitaxial layer $a_{||}$ can be calculated from simple geometric considerations [22].

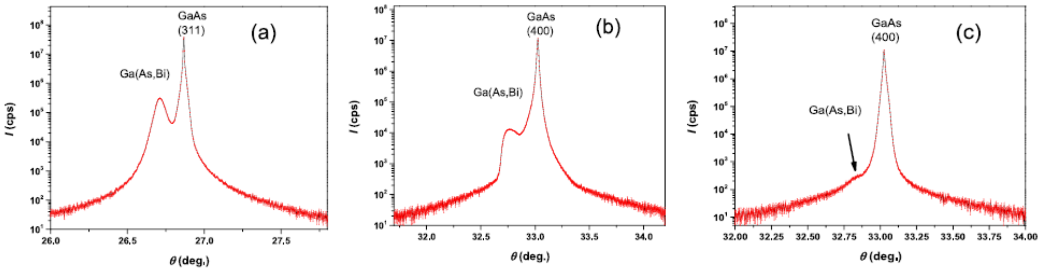

Fig. 6.2: XRD curves of (311)B GaAsBi sample (a) symmetrical (311) diffraction pattern; (b) and (c) asymmetrical (400) diffraction patterns. Asymmetrical patterns were obtained with (b) θ_B - φ and (c) $\theta_B + \varphi$ incidence angles, where θ_B is the Bragg angle for the given set of crystallographic planes, and φ is the angle between (100) planes and the (311)-oriented surface.

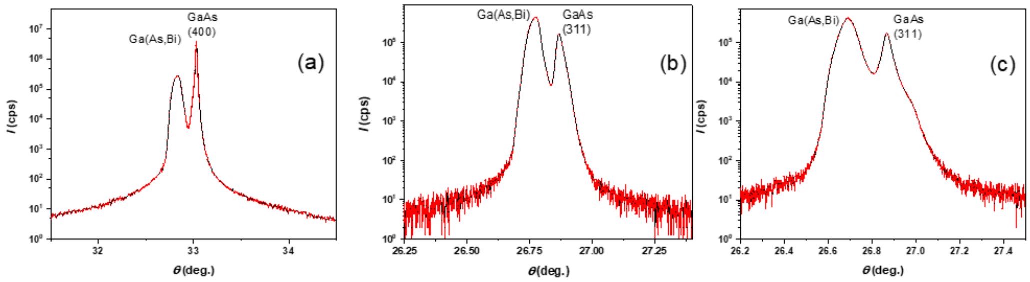

Fig. 6.3: XRD curves of (100) GaAsBi samples (a) symmetrical (400) diffraction pattern; (b) and (c) two asymmetrical (311) diffraction patterns. Asymmetrical patterns were obtained with (b) $\theta_B - \varphi$ and (c) $\theta_B + \varphi$ incidence angles, where θ_B is the Bragg angle for the given set of crystallographic planes and φ is the angle between (311) planes and the (100)-oriented surface.

As can be seen from Fig. 6.2 and 6.3, the XRD patterns of (311)B GaAsBi and (100) GaAsBi samples have similar characteristics. However, it is worth pointing out that the intensity of the peak from the (311)B GaAsBi thin film shown in Fig. 6.2 (c) is lower than that of the (100) GaAsBi sample (Fig. 6.3 (c)). This is due to the large incidence angle which results in less reflected radiation than at the small incidence angle.

Bi concentration was calculated from the lattice parameter of $GaAs_{1-x}Bi_x$ layer determined from symmetrical XRD using Vegard's law [23] with the assumption of diluted alloy of GaAs and GaBi. The drawback of such approach is that there are no reports of growth of bulk GaBi, and therefore one can only consider the theoretical calculation of GaBi lattice [24]. For the present work it was considered that GaBi has a zinc-blend cubic lattice with the lattice parameter a = 6.178 Å. It was found that Bi concentration is equal to 5.4% for both samples grown on (100) and (311)B-oriented surfaces.

Residual strains (ε_{zz} and ε_{xx}) in $GaAs_{1-x}Bi_x$ layer were determined from the analysis of asymmetrical XRD. Out-of-plane $a_\perp$ and in-plane strain $a_{||}$ were used to calculate the deformation of layer's lattice by using the following formulas for strains:

$$\varepsilon_{zz} = \frac{a_\perp - a_{FR}}{a_{FR}}; \varepsilon_{xx} = \frac{a_{||} - a_{FR}}{a_{FR}},$$

where $a_\perp$ is the out-of-plane lattice parameter, $a_{||}$ is the in-plane lattice parameter, and a_{FR} is lattice parameter of fully relaxed GaAs lattice. It was found that epilayer $GaAs_{1-x}Bi_x$; ε_{zz} is equal 0.00035 in both samples, while ε_{xx} for the sample grown on (311)B-oriented surface (ε_{xx} = -0.0183) is 2.64 times less than that of (100)-oriented sample (ε_{xx}= -0.0484).

6.3.2 ELECTRICAL PROPERTIES

6.3.2.1 CURRENT-VOLTAGE CHARACTERISTICS

In order to select suitable diodes for DLTS and LDLTS measurements for both samples grown on different substrate orientations, I-V characteristics were obtained at room temperature. The reverse bias current density (J) for all samples over the voltage bias range -1V to 0V is of the order of few µA/cm^2. Typical room temperature semi-logarithmic J-V characteristics are shown in Fig. 6.4 for all samples. It can be seen from Fig. 6.4 that all samples display a relatively low leakage current density. In particular, the reverse current density for samples grown on (100) is larger than that grown on (311)B. The reverse current density at bias of -1V for (100) GaAs, (311)B GaAs, (100) GaAsBi and (311)B GaAsBi are 1.06x10^{-4} A/cm^{-2}, 8.26x10^{-8} A/cm^{-2} , 7.5×10^{-5} A/cm^{-2} and 6.2×10^{-6} A/cm^{-2}, respectively. The reason for the higher reverse current density in samples grown on (100) can be explained by the higher trap concentrations and more defects in (100) than (311)B [25]. Similar behaviour was observed in previous studies on n-type GaAs grown on conventional (100) and non-conventional substrate orientations (n11) [26] where the reverse current was found to decrease with increasing the index of the plane n.

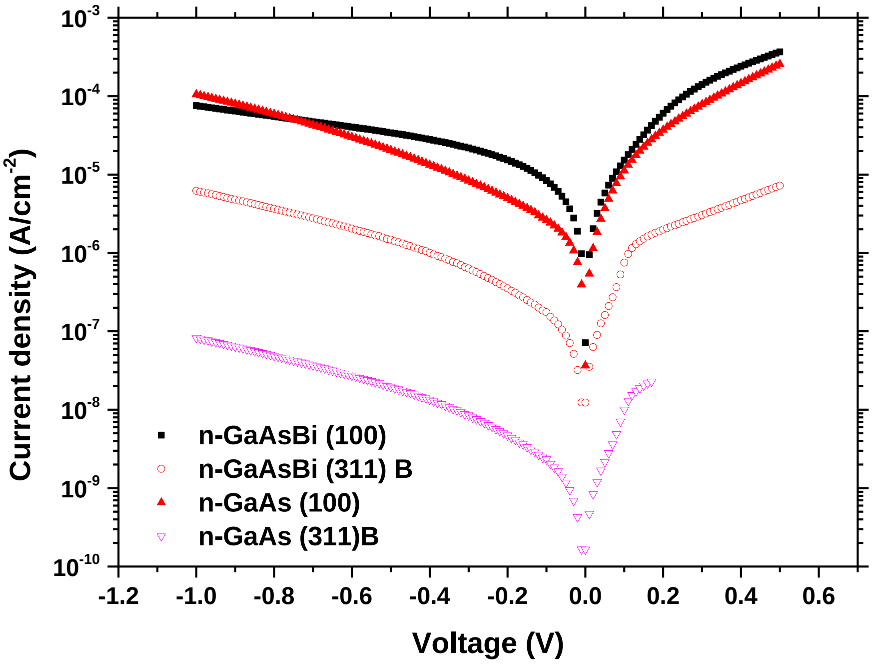

Fig. 6.4: J-V plot for n-type (100) GaAs, (311)B GaAs, (100) GaAsBi and (311)B GaAsBi at room temperature.

Since these devices are Schottky diodes, the I-V characteristics of the diodes can be described by the thermionic emission model [27] as follows:

$$I = I_0[exp\left(\frac{q(V-IR_S)}{nk_{\boldsymbol{B}}T}\right) - 1] \qquad (6.1)$$

where q is the electronic charge, V is the applied voltage, $k_{\boldsymbol{B}}$ is the Boltzmann's constant, n is the ideality factor of the diode, T is the absolute temperature in Kelvin, R_s is the series resistance of the effective diode, and I_0 is the saturation current which is given by:

$$I_0 = AA^*T^2\, exp\left(\frac{-q\phi_B}{k_BT}\right) \qquad (6.2)$$

where A is the diode area, A^* is the effective Richardson's constant (A^*= 8.16 Acm^{-2} K^{-2}), and ϕ_B is the barrier height [28].

The characteristics parameters of these devices such as (n, R_s, ϕ_b and I_0) were calculated by using the Werner's method [29]. This method was explained in Chapter 4, section 4.3. Fig. 6.5 shows the plot of G/I versus G and $ln\ (I)$ versus $(V - IR_s)$ for (311)B GaAsBi. Similar way was used to extract the diode parameters for all samples.

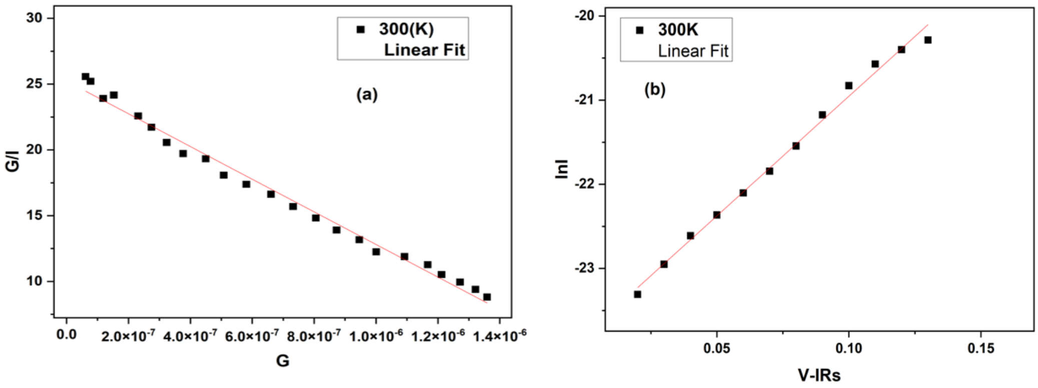

Fig. 6.5: (a) the plot of G/I versus G from I-V curve at room temperature for forward voltage for (311)B GaAsBi sample (this plot was used to determine the ideality factor and series resistance). (b) plot of $ln\ (I)$ versus $(V - IR_s)$ to obtain barrier height.

Series resistance, ideality factors and barrier height for all samples are obtained from the forward I-V characteristics at room temperature. These parameters are summarized in Table 6.2.

Table 6.2. Experimental data of ideality factor, barrier height and series resistance, obtained from I-V characteristics at room temperature for n-type (100) GaAs, (311)B GaAs, (100) (GaAsBi) and (311)B GaAsBi.

Sample	n	ϕ_B (eV)	R_S (kΩ)
n-GaAs (100)	1.50±0.02	0.74±0.03	0.23±0.02
n-GaAs (311)B	1.49±0.02	0.69±0.02	1.32±0.03
n-GaAsBi (100)	2.33±0.01	0.67±0.01	36.30±0.01
n-GaAsBi (311)B	1.61±0.01	0.62±0.01	2.30±0.03

Fig. 6.6 shows the temperature dependence of (a) the ideality factor (n) and (b) barrier height (ϕ_B) of all samples over the temperature range 200 K to 340 K.

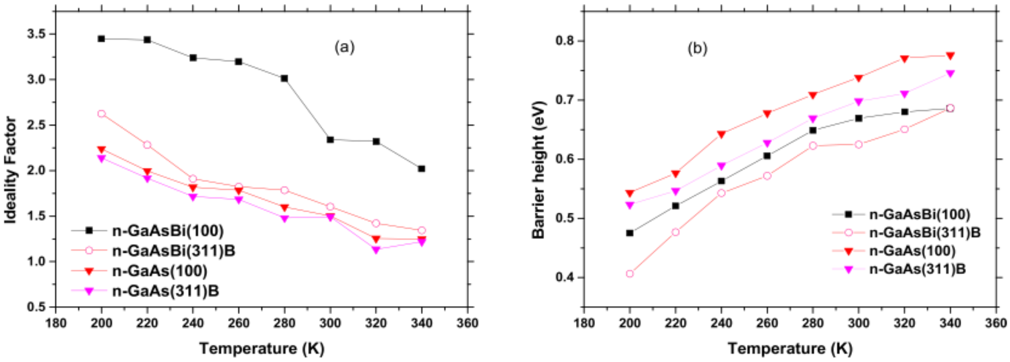

Fig. 6.6: Temperature dependence of (a) ideality factor; (b) barrier height, obtained from I-V characterises for all n-type samples.

As can be seen from Table 6.2, the ideality factor of all devices in forward bias deviates from unity, where n is nearly 2, which suggests that there is significant generation-recombination in depletion region, which is the dominant current mechanism [4,30]. It is worth noting that such deviation of the ideality factor from the thermionic emission can be attributed to several effects, such as inhomogeneity of Schottky barrier height, series resistance, interface states and non-uniformity of interfacial charges [31–33]. As shown in Fig. 6.6 (a) and (b) the values of n decrease with increasing temperature, whereas the values of (ϕ_B) increase as temperature is increased. This behaviour is due to inhomogeneous metal/semiconductor (MS) contacts. At high temperatures, the current flows through the interface states in the regions with a lower barrier height and larger ideality factor, whereas at low temperatures the carriers are frozen, and therefore, the current does not follow the thermionic emission mechanism. Note that at low temperatures, carriers can overcome the lower barriers, and the transmission mechanism will be dominated by the current flowing through the regions with the lower barrier height. As the temperature increases, the carriers gain enough energy to overcome the higher potential barrier, which causes the barrier height to increase with temperature. As a result, the barrier height will increase, while the ideality factor will decrease with increasing temperatures, due to barrier inhomogeneity in MS contacts [34]. However, (100) GaAsBi has larger ideality factors over all temperatures compared to other diodes, whereas the (311)B GaAs has the smallest values. It is worth noting that, and to the best of our knowledge, no previous reports have explained the Schottky diodes behaviour in GaAsBi grown on different substrate orientations in the literature. Therefore, the results will be discussed in context with dilute nitride GaAsN instead.

Furthermore, from Table 6.2 it can also be seen that the barrier height at room temperature for (100) GaAsBi and (311)B GaAsBi are reduced compared with reference samples. In particular, (100) GaAs has relatively larger barrier height, while the (311)B GaAsBi diodes have the lowest values. This reduction in barrier height was observed also by Chen et al. [35] in their study using Cu Schottky contacts to n-type GaAsN grown on (100) and (311)A/B GaAs substrates by Chemical Beam Epitaxy (CBE). They found that samples grown on (311)B exhibited lower barrier height than (100). They attributed this reduction to the polarity of growth surface. On the other hand, Narayanamurti et al. [36] observed in their study using the ballistic electron emission microscopy (BEEM) technique, that the barrier height at room temperature decreases as the nitrogen content increases. They attributed the reduction in the barrier height to the reduction of the band gap, with increasing incorporation of nitrogen.

It is well-known that Bi incorporation is more enhanced in (311)B than in (100) GaAs substrates. This results in an enhancement of the reduction of the energy band gap of (311)B with respect to the (100) samples, as reported previously [12,37]. This fact could explain the larger reduction of the barrier height observed in the (311)B samples. However, this interpretation is in contradiction with XRD results. Therefore, one would expect that the electrical performance of Schottky diodes constructed on GaAsBi layers could also by tailored by the growth orientation or surface polarity, also many other effects such as non-homogeneity of Schottky barrier height, could contribute in reduction of barrier height in (311)B sample [35].

6.3.2.2 CAPACITANCE-VOLTAGE CHARACTERISTICS

The C-V measurements were carried out at room temperature with a frequency of 1 MHz in order to determine the free carrier concentration (N_d). Fig. 6.7 (a) shows the experimental net carrier concentration N_d obtained from the slope of $1/C^2$ as a function of V (reverse voltage) for all samples. The free carrier concentration was found to be homogeneous for all samples. In particular, the free carrier concentrations of (100) GaAs, (311)B GaAs, (100) GaAsBi and (311)B GaAsBi , are ~ $3.8x10^{17}$ cm^{-3} , $3.4x10^{17}$ cm^{-3}, ~$1.03x10^{16}$ cm^{-3} and ~$1.14x10^{16}$ cm^{-3} , respectively. Fig. 6.7 (b) shows Capacitance/Area (C/A) versus V plot for (100) and (311)B GaAsBi samples. As can be seen from Fig. 6.7 (b), the value of C/A of sample grown on (311)B is lower than the one grown on (100). This reduction of C/A of (311)B samples could possibly be due to the growth orientation, which was found to affect the shallow donor concentration $N_{d,}$ as confirmed previously by Hall measurement [35,38,39].

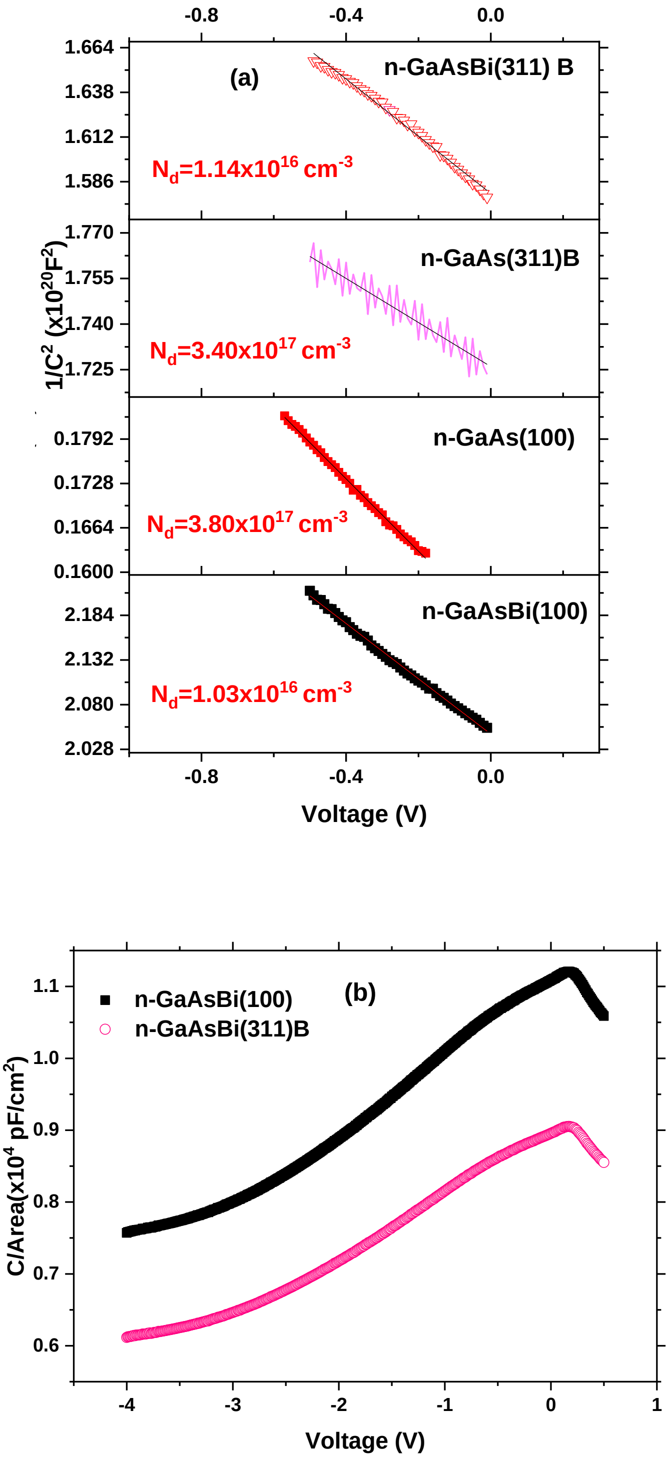

Fig. 6.7: (a) Plot of 1/C^2 versus reverse bias voltage for n-type (100) GaAs, (311)B GaAs, (100) GaAsBi and (311)B GaAsBi at room temperature. (b) The experimental C/A versus V plot for (100) and (311)B GaAsBi samples at room temperature.

6.3.2.3 DLTS AND LAPLACE (DLTS) MEASUREMENTS

In order to study the electrically active defects with energies within the forbidden band gap of these n-type (100) GaAs, (311)B GaAs, (100) GaAsBi and (311)B GaAsBi devices, DLTS technique has been employed [40]. As can be seen in Fig. 6.8, the measurements were carried out over a temperature range from 100 K up to 450 K. The experimental parameters used are: reverse bias (V_R) of -1 V, filling pulse voltage (V_P) of 0V with filling pulse time (t_p) of 1 msec and rate window set to be at 200 s^{-1} for all investigated samples.

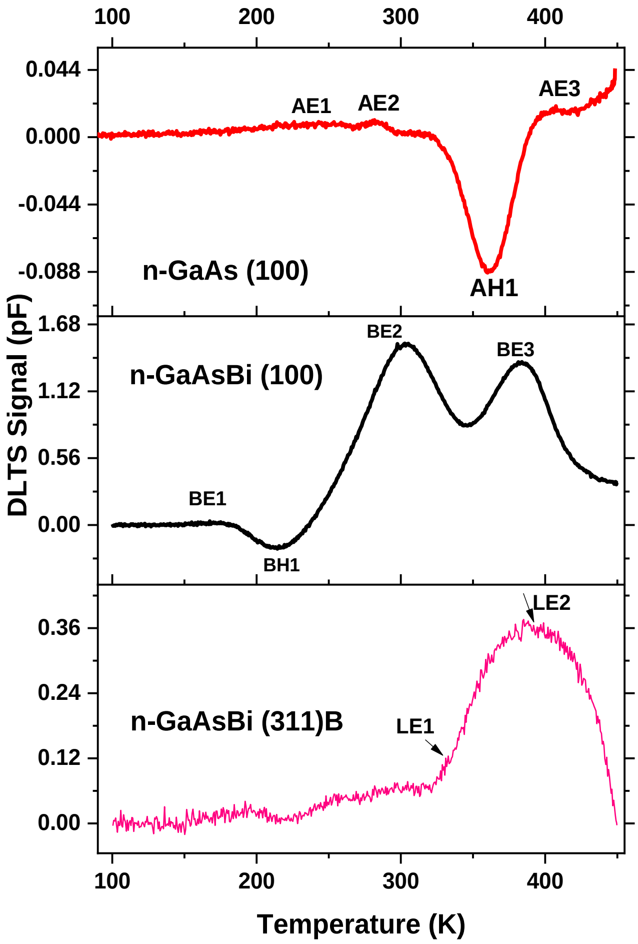

Fig. 6.8: Typical DLTS spectra scans for n-type (100) GaAs, (100) GaAsBi and (311)B GaAsBi samples.

The standard DLTS spectra in Fig. 6.8 of (100) GaAs and (100) GaAsBi samples show three positive peaks corresponding to three majority electron traps. In addition to the electron traps, hole traps (negative peaks) were also observed in (100) GaAsBi and (100) GaAs. While for GaAsBi sample grown on (311)B (Fig. 6.8), a very broad peak is detected over the temperature range ~ 325 K to ~450 K. For control sample (311)B GaAs no defects were detected by DLTS as their concentrations could be too low and are outside the detection limit of DLTS. In order to resolve the broad peaks obtained by DLTS measurements, as well for a better resolution of DLTS spectra observed in the investigated samples, LDLTS measurements were performed [41] on all samples, under same conditions as those used in DLTS experiments. LDLTS revealed the presence of the following traps: (i) (100) GaAs and (100) GaAsBi: three electron traps labelled as (AE1, AE2 and AE3) and (BE1, BE2 and BE3), and one hole trap (AH1) and (BH1), respectively; (ii) (311)B GaAsBi: two electron traps namely (LE1 and LE2). The activation energies of each defect were determined from the Arrhenius plot of the emission rates as a function of inverse temperature as illustrated in Fig. 6.9.

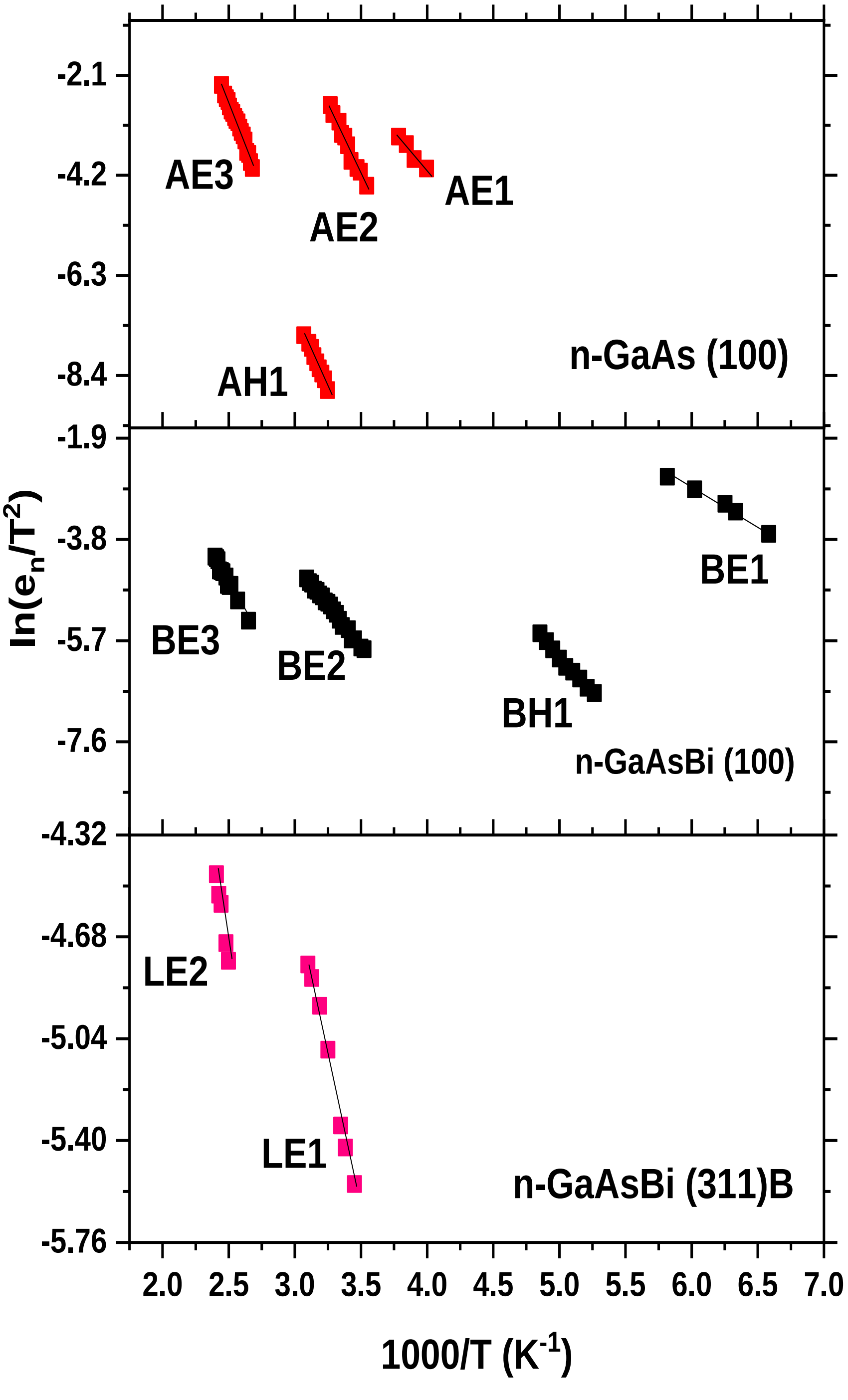

Fig. 6.9: Arrhenius plots obtained from Laplace DLTS for n-GaAsBi grown on (a) (100) and (b) (311)B GaAs substrates, with reverse voltage V_R=-1, filling pulse height V_P=0 V, and filling pulse time t_p=1 msec.

The traps activation energies, apparent cross section and trap concentrations are calculated from the slope and intercept of the Arrhenius plot, as explained in chapter 4. The traps parameters are summarised in Table 6.3.

Table 6.3. Traps parameters for n-(100) GaAs, n-(100) GaAsBi and (311)B GaAsBi.

Sample	Trap Label	Activation energy (eV)	Apparent capture cross-section (cm^2)	Trap concentration (cm^{-3})
n-GaAs (100)	AE1	0.28±0.03	4.3x10^{-17}±0.3	8.2x10^{15}±0.7
	AE2	0.54±0.02	2.1x10^{-13}±0.1	7.2x10^{15}±0.2
	AH1	0.53±0.02	4.8x10^{-16}±0.3	8.1x10^{15}±0.5
	AE3	0.61±0.01	1.8x10^{-14}±0.1	5.1x10^{15}±0.3
n-GaAsBi (100)	BE1	0.12±0.01	1.1x10^{-18}±0.1	1.2x10^{13}±0.1
	BH1	0.24±0.01	9.8x10^{-18}±0.8	5.1x10^{13}±0.3
	BE2	0.27±0.01	9.3x10^{-19}±0.9	7.7x10^{14}±0.5
	BE3	0.41±0.04	6.3x10^{-18}±0.7	9.7x10^{14}±0.4
n-GaAsBi (311)B	LE1	0.19±0.01	5.1x10^{-20}±0.2	1.4x10^{13}±0.1
	LE2	0.29±0.01	1.8x10^{-19}±0.1	1.9x10^{14}±0.1

It can be seen from Table 6.3, that the number of traps detected in sample grown on (100) are higher than sample grown on (311)B. In fact, R. Mari [26] observed that the substrate orientations of GaAs have a significant impact on the incorporation of impurities and traps into the structure. It was reported that impurities are more susceptible to be incorporated in (100) plane than in other high index planes. This result correlated with I-V characterisation discussed above, where samples grown on (100) has higher reverse current than samples grown on (311)B due to higher number of traps.

The best way to identify these active traps created as a result of substrate orientations are to compare their activation energies to each other and/or their DLTS signals. The obtained results are also discussed and compared with previous works.

The traps BE1 (0.12±0.01eV) and LE1 (0.19±0.01) observed in (100) GaAsBi and (311)B GaAsBi, respectively, are likely to correspond to the same traps ET_0 and ET_1 with activation energies ranging from 0.07 to 0.19eV [7] and A' with activation energy of 0.12 eV [11] reported previously. These were assigned to traps involving Bi as a constituent.

Traps AE1, BE2, and LE2 with similar activation energies in the range 0.27 to 0.29eV could be of the same origin. This trap, labelled as ET_2 with an activation energy in the range 0.29 to 0.33eV, was observed also in both GaAs and GaAsBi grown by MBE at low temperature by Gelczuk et al. [7]. This deep level can be attributed to the well-known M_3 trap (E_c-0.34 eV) [42,43] , which has same signature as EL6 trap reported in ref.[43]. The EL6 trap is generally related to complex pair defects involving arsenic antisite (As_{Ga}) and arsenic vacancy (V_{As}) [43] or to divacancy complex defect ($V_{Ga} – V_{As}$) [44]. On the other hand, using theoretical calculations by density functional theory (DFT method) [45], a trap with energy of 0.36 eV (similar to BE2) was found. The authors attributed its origin to a complex defect involving Bi·

Furthermore, the traps AE2 and BE3 with activation energies 0.54±0.02 eV and 0.41±0.04 eV and trap concentrations of $7.2x10^{15}$ cm^{-3} and $9.7x10^{14}$ cm^{-3}, were observed only in n-type (100) GaAs and GaAsBi samples, respectively. Similar deep defect was detected in n-type GaAsBi samples grown at temperatures 330°C and 390℃, respectively, labelled as trap C [11] and trap ET3 [7] with activation energies varying from 0.45 to 0.52 eV [7]. This trap most likely corresponds to the trap level M4. The origin of this trap was attributed to an arsenic vacancy (V_{As}) complex involving an impurity [46].

In addition, the trap level AE3 with activation energy of 0.61±0.01 eV and concentration $5.1x10^{15}$ cm^{-3} was detected only in the n- (100) GaAs control sample (without Bi). This trap was observed also in GaAs and GaAsBi as the dominant electron trap [7]. It was suggested that the origin of this deep level trap could possibly be attributed to trap M6, whose activation energy is 0.62 eV [47]. It is interesting to note that M6 trap is a unique trap in GaAs layers grown by MBE [42]. The origin of this trap might be related to gallium and arsenic vacancies (V_{As} - V_{Ga}) or impurity related complexes (V_{As} – X- V_{Ga}), where X refers to the impurity or interstitial [47]

As seen in Table 6.3, hole traps were also observed in (100) GaAs and (100) GaAsBi labelled as AH1 and BH1, with activation energies 0.53±0.02 eV and 0.24±0.01 eV, respectively. Minority hole trap AH1 appears to have a similar activation energy as that of trap H2 [48], and the trap with activation 0.54±0.02 eV observed in ref.[49]. This trap was suggested to be likely attributed to donor level of the arsenic antisite As_{Ga} complexes defect [48]. Trap BH1 has similar DLTS spectra as those observed in p-type GaAsBi grown by MBE [50] and labelled as HT2 and HT3 with activation energies over a range 0.23- 0.43eV. These traps were assigned to As_{Ga} or its relevant cluster.

6.3.3 OPTICAL PROPERTIES

6.3.3.1 RAMAN SPECTROSCOPY

Fig. 6.10 shows the Raman spectra for all samples, i.e., (100) GaAs and (311)B GaAs (control samples) and (100) GaAsBi and (311)B GaAsBi, in the ranges (i) 150 to 245 cm^{-1} and (ii) 250 to 300 cm^{-1}.

Two intense peaks in the range of 260-300 cm^{-1} were observed in all samples. These Raman peaks are associated with the GaAs optical phonons at the Brillouin zone centre [51,52]. Particularly, the transverse optical mode (TO(Γ)) is observed at around 267 cm^{-1} and the longitudinal optical mode (LO(Γ)) at around 291 cm^{-1}. Furthermore, the GaAs TO(Γ) Raman peak is forbidden by Raman selection rules for the (100) samples, while for the (311)B samples this peak is allowed [53,54]. A broad TO(Γ) Raman peak was observed for the (100) GaAsBi sample, which can be explained by a breakdown of Raman selection rules due to Bi-induced disorder.

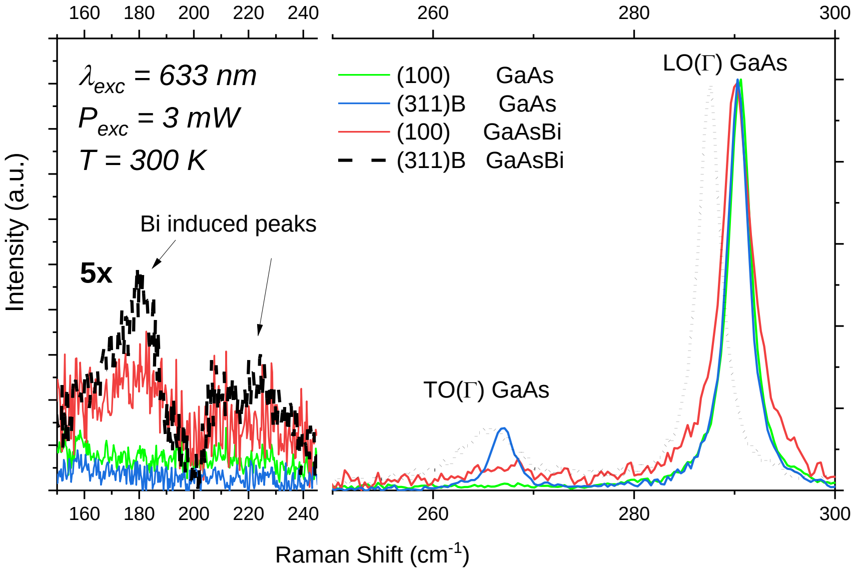

Fig. 6.10: Raman spectra of GaAs and GaAsBi samples grown on GaAs (100) and GaAs (311)B substrates at 300K.

For the GaAsBi samples, additional Raman peaks were detected in the range 150 – 240 cm^{-1}. The observation of these peaks was reported previously for GaAsBi samples [54–60]. Although the nature of the peaks is not well established, it is well known that these peaks are Bi-induced.

The Raman spectra in the range 250 to 300 cm^{-1} were well fitted by two Lorentz functions (the fitting parameters are shown in Table 6.4). Although these samples are doped, we have observed no evidence of the presence of the peak due to plasmons-phonons coupling (LOCP). In general, our results show that the contribution of the LOCP is probably small and that this peak is not well resolved from GaAs LO(Γ) and TO(Γ) Raman modes. In addition, a red-shift of the LO(Γ) Raman peak for GaAsBi samples was observed as compared to the reference GaAs samples. It is expected that the incorporation of bismuth atoms will result in significant changes of the mechanical properties of $GaAs_{1-x}Bi_x$ alloys. Particularly, the Bi incorporation will change the frequency of phonon vibration modes of the crystalline matrix. It was previously observed that the GaAs LO(Γ) position changes linearly with the Bi concentration (x) [54,61]. On the other hand, the phonon frequencies can also be dependent on the presence of strain in the alloys [54,61]. Such stress-induced shifts can basically be described by the phonon deformation potentials (PDPs). Therefore, the total frequency shift could be associated with two different contributions: (i) the changes in the alloying composition (x) of the ternary material ($\Delta\omega_{alloy}$) and (ii) changes of the strain field in the alloy ($\Delta\omega_{strain}$). The total shift of the optical phonon modes can then be quantitatively expressed as $\Delta\omega = \Delta\omega_{strain} + \Delta\omega_{alloy}$ [54,61]. As the Bi content is 5.4% for both (100) and (311)B samples, the different shifts observed for the Raman modes must be due to the strain effect.

Particularly for the (311)B sample, the observed shift is -60 cm^{-1}/xBi which is consistent with previous works [16,55,56,60,61]. On the other hand, for the (100) GaAsBi sample a lower shift was observed probably due to a blue-shift originated by compressive strain ($-\Delta\omega_{strain}$), in agreement with the shift reported by E. Tisbi et al [55]. Furthermore, the High Resolution XRD (HR-XRD) results have shown that the strain for the (100) GaAsBi samples is 2.7 times higher than that of (311)B samples. In addition, a broadening of the LO(Γ) Raman peak was observed for the GaAsBi samples, a disordering effect for these samples which is particularly higher in the (100) GaAsBi samples. Similar broadening was also observed for the TO(Γ) Raman mode, but more importantly the observation of this peak in (100) GaAsBi samples is probably due to Bi induced disorder. A smaller red-shift of the TO(Γ) Raman peak was observed as compared to the red-shift observed for the LO(Γ) Raman peak for GaAsBi samples, which were similarly reported previously in the literature. In general, these results indicate that the introduction of Bi in the (100) samples causes a higher compressive strain and higher crystal disorder as compared to the GaAsBi (311)B samples. These differences have an important impact on the optical emission of these samples as will be discussed below.

Table 6.4. Lorentzian fitting parameters:

	(100) GaAs	**(100) GaAsBi**	**(311)B GaAs**	**(311)B GaAsBi**
LO(Γ)				
ω_{peak} (cm^{-1})	290.5±0.5†	290.2±0.5†	290.3±0.5†	287.5±0.5†
FWHM – Δω (cm^{-1})	2.6±0.5†	3.7±0.5†	2.5±0.5†	2.8±0.5†
Peak relative intensity	1.00±0.01	0.98±0.01	1.00±0.01	0.97±0.01
TO(Γ)				
ω_{peak} (cm^{-1})	*262.4*±0.5†	266.7±0.5†	266.9±0.5†	265.5±0.5†
FWHM – Δω (cm^{-1})	*22.9*±0.5†	10.6±0.5†	2.7±0.5†	6.7±0.5†
Peak relative intensity	*0.007**±0.01	0.04±0.01	0.16±0.01	0.13±0.01
Reduced chi-square	2.59 10^{-5}	1.77 10^{-4}	3.26 10^{-5}	9.14 10^{-5}
Residual Sum of Squares	0.00411	0.02807	0.00518	0.01453
R-Square	0.9992	0.9957	0.9990	0.9971

** less than the noise level ≈0.01; † The experimental error is bigger than the statistic error related to the Fit processes. In these cases, we utilize the experimental error.*

6.3.3.2 Photoluminescence

Fig. 6.11 shows the photoluminescence spectra of GaAs (100), GaAs (311)B, GaAsBi (100) and GaAsBi (311)B layers.

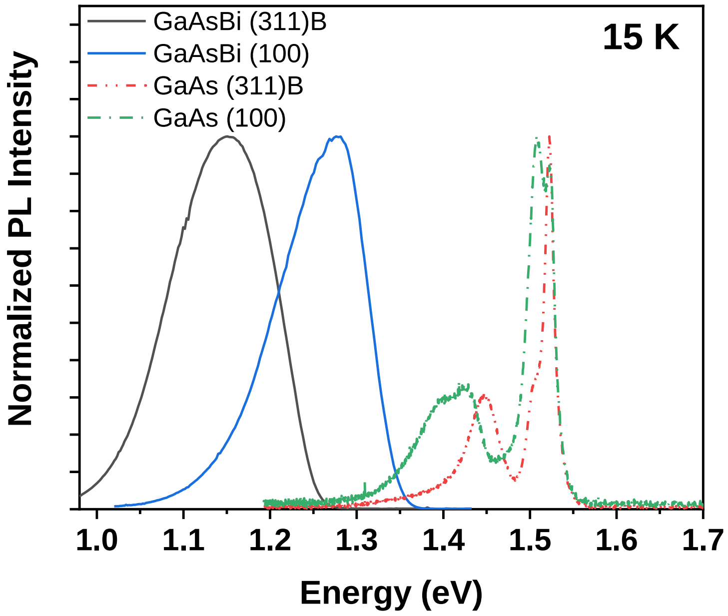

Fig. 6.11: Normalized PL spectra of GaAs and GaAsBi layers at 15K

A sharp emission is clearly seen at around 1.52eV for both GaAs layers as expected. In addition, other PL peaks were also observed: one around 1.508 eV and a broad band in the range of 1.3-1.49 eV which were mainly associated to transitions related to GaAs –like traps/impurities due to the growth conditions. On the other hand, the PL spectra of both (100) and (311)B $GaAs_{0.94}Bi_{0.05}$ layers show a redshift as compared to GaAs samples, as expected [62–64]. The observed redshift of PL peak position was associated with Bi incorporation which induces a band gap reduction. Although both samples have the same Bi concentration, we have observed that the PL peak position of both samples are different and do not show the standard red shift of 89 meV/Bi% previously reported in the literature for GaAsBi layers [1,62,64]. Actually, for these samples this red shift is lower than previously reported. This effect is particularly more important for the (100) GaAsBi samples. It was previously shown a similar behavior for n-doped (100) GaAsBi samples [7] which was associated with the contribution of Bi induced donor traps next to the conduction band which could also induce an additional emission in the spectrum due to a donor trap (DT)-valence band (VB) transition and therefore could result in a reduced red shift. Particularly, these results show that the PL red shift of (100) GaAsBi layer is much lower than for (311)B GaAsBi samples although both samples have the same Bi concentration of 5.4 %. The obtained values of PL peak position for the (100) and (311)B samples are different and could be due to the other contributions such as different Bi induced traps in these samples. However, the XRD results for these samples show that the samples also have different strain which could affect considerably their optical properties. Particularly, it was noticed that the DLTS results have shown higher number of carrier traps for the (100) GaAsBi samples as compared to the (311)B GaAsBi samples which certainly could affect significantly its optical properties. However, the XRD results have also shown that the compressive strain for the (100) samples is 2.7 times higher than for the (311)B samples. An increase of compressive strain will certainly result in important changes in the band structure resulting in blue shift of PL peak position as shown previously [55].

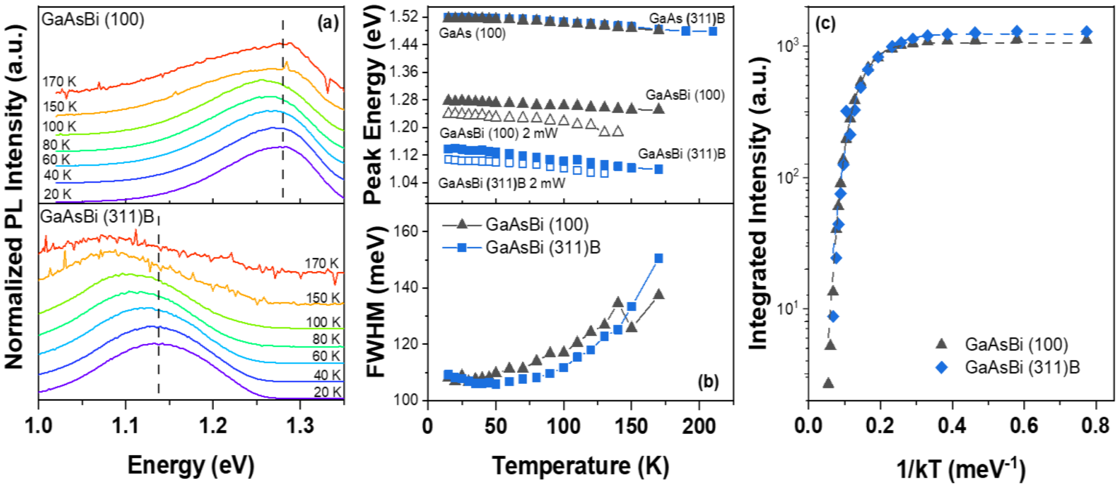

Fig. 6.12: Temperature dependence of (a) PL spectra and of (b) PL peak position and linewidth (c) Arrhenius Plot and activation energies for (100) and (311)B GaAsBi samples.

Fig. 6.12 (a) shows the temperature dependence of the PL spectra, peak energy and Full Width at Half Maximum (FWHM) of the doped $GaAs_{1-x}Bi_x$ samples. It was observed that the PL energy peaks (Fig. 6.12 (b)) exhibit a monotonic redshift with increasing temperature due to the decrease of the band-gap energy with increasing temperature as expected. The temperature dependence of PL intensity was analyzed with a modified Arrhenius equation [15]:

$$\frac{I_{PL}(T)}{I_0} = \frac{1}{1+A_1 e^{\frac{-E_1}{k_B T}}+A_2 e^{\frac{-E_2}{k_B T}}}$$

where I_{PL} is the integrated PL intensity, A_1 and A_2 are constants related to the density of non-radiative recombination centers, E_1 and E_2 are activation energies, k_B is the Boltzmann constant, T the temperature and I_0 the approximate PL intensity when T→0. Fig. 6.12(c) shows the obtained results of Arrhenius fitting and the activation energy values for both GaAsBi (100) and (311)B samples. The obtained E1 and E2 values for (100) and (311)B samples are (20±3)meV and (95±4)meV, and (28±3) mV and (74±3) meV, respectively. These values evidence the presence of Bi clusters and alloy disorder in both samples. Actually, it was previously reported that the $GaAs_{1-x}Bi_x$ layers usually have localized Bi pairs and clusters, which have different configurations and binding energies, and also alloy disorder, and potential fluctuation [15]. Particularly, it was previously reported that the presence of defects/disorder results in two different activation energies: one in the range of 8–17 meV which is usually related to Bi clusters and Bi pairs, and another around 50 meV which is usually related to GaAsBi alloy disorder [15,65]. Therefore, the experimental values obtained in this work are fully consistent to this interpretation.

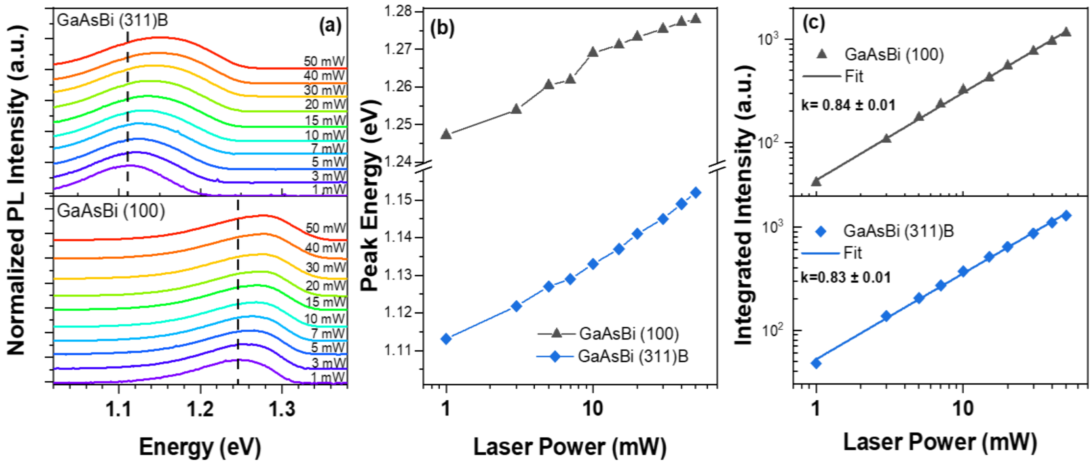

Fig. 6.13: (a) PL spectra for different laser powers (b) PL peak position and (c) Double logarithmic plot of the integrated intensity as function of laser power for GaAsBi (100) and (311)B samples at 10K.

The laser power dependence of PL spectra for both samples was also investigated. Fig. 6.13 (a), (b) and (c) shows the PL spectra versus laser power, the laser power dependence of PL peak position, and integrated PL, respectively at 10K. It was observed that there is a clear blue shift of PL peak energy with increasing laser power. However, this effect seems to be different for (311)B and (100) GaAsBi samples. Particularly, for the (100) samples a blue shift was observed of about 25meV with increasing laser power, while for the (311)B sample a blue shift of about 43meV for a laser power of 50mW was observed (Fig. 6.13(a) and (b)). Fig. 6.13 (c) shows the laser power dependence of integrated PL intensity also at 10K. The laser power dependence was fitted by using the power law which is a standard procedure to investigate the nature of the PL band in semiconductor materials and is given by the following expression: $I = \alpha (P)^k$, where I is the integrated PL intensity, P is the laser power, α and k are fitting parameters [15,62]. It is well known for free exciton emission it is expected to obtain $k \approx 1$ [15,62]. However, for these samples a value slightly lower than k=1 was obtained, i.e., $k \approx 0.8$ for the higher laser power range of 1-50mW. These results indicate some exciton localization which is similar to several previous results reported in the literature for GaAsBi layers [15,62,65]. Therefore, these results could be associated with the emission of localized excitons by the presence of Bi clusters/ alloy disorder, which manifests in a clear blue shift of the PL peak with increasing laser power and is consistent with the obtained values for E_1 and E_2 activation energies [15,62,65]. It is important to note that the DLTS results for the (100) samples have shown a larger number of traps as compared to the (311)B samples. As mentioned above, it was previously reported for n-doped (100) GaAsBi samples that the PL spectra have also a contribution of optical transition related to Bi induced traps close to the conduction band (donor band) which could also affect the laser power dependence and the PL peak position [7]. Therefore, the PL results reported here are consistent with the DLTS results of these samples that have shown that the number of Bi induced traps are more important for (100) GaAsBi samples and therefore these traps affect more the PL of (100) samples as compared with the (311)B samples. On the other hand, as mentioned previously the higher compressive strain observed for (100) GaAsBi samples could also affect their optical properties resulting in the observation of PL peak position at higher energy as compared to GaAsBi (311)B samples with the same amount of Bi%.

6.4 Conclusion

The structural, electrical and optical properties of n-type GaBiAs layers grown under similar conditions on GaAs (100) and (311)B planes have been investigated. It was found that although these samples have the same Bi concentration of 5.4%, they have shown different compressive strain which has important impact on their optical properties. Furthermore, it was observed that the incorporation of Bi reduces the GaAs like electron traps but also induces Bi-related donor traps which are different for GaAsBi samples grown on (100) and (311)B planes. Particularly, the DLTS results have shown that Bi traps are reduced considerably for (311)B samples. Finally, the observed differences in the optical properties of (100) and (311)B GaAsBi samples can be explained by the presence of different compressive strain and by the presence of Bi-induced traps which affect considerably the optical properties of GaAsBi layers.

REFERENCES:

[1] S. Francoeur, M.-J. Seong, A. Mascarenhas, S. Tixier, M. Adamcyk, T. Tiedje, *Band gap of GaAs1−xBix, 0<x<3.6%*, Appl. Phys. Lett. **82**, 3874 (2003).

[2] B. Fluegel, S. Francoeur, A. Mascarenhas, S. Tixier, E.C. Young, T. Tiedje, *Giant spin-orbit bowing in GaAs1-xBix*, Phys. Rev. Lett. **97**, 067205 (2006).

[3] Z. Batool, K. Hild, T.J.C. Hosea, X. Lu, T. Tiedje, S.J. Sweeney, *The electronic band structure of GaBiAs/GaAs layers: Influence of strain and band anti-crossing*, J. Appl. Phys. **111**, 11310 (2012).

[4] Z. Zhou, D.F. Mendes, R.D. Richards, F. Bastiman, J.P. David, *Absorption properties of GaAsBi based p–i–n heterojunction diodes*, Semicond. Sci. Technol. **30**, 094004 (2015).

[5] V. Pačebutas, K. Bertulis, G. Aleksejenko, A. Krotkus, *Molecular-beam-epitaxy grown GaBiAs for terahertz optoelectronic applications*, J. Mater. Sci. Mater. Electron. **20**, 363 (2009).

[6] X. Lu, D.A. Beaton, R.B. Lewis, T. Tiedje, M.B. Whitwick, *Effect of molecular beam epitaxy growth conditions on the Bi content of GaAs1−xBix*, Appl. Phys. Lett. **92**, 192110 (2008).

[7] Ł. Gelczuk, J. Kopaczek, T.B.O. Rockett, R.D. Richards, R. Kudrawiec, *Deep-level defects in n-type GaAsBi alloys grown by molecular beam epitaxy at low temperature and their influence on optical properties*, Sci. Rep. **7**, 12824 (2017).

[8] A.R. Mohmad, F. Bastiman, C.J. Hunter, J.S. Ng, S.J. Sweeney, J.P.R.

David, *The effect of Bi composition to the optical quality of GaAs 1−x Bi x*, Appl. Phys. Lett. **99**, 042107 (2011).

[9] J. Gebauer, R. Krause-Rehberg, S. Eichler, M. Luysberg, H. Sohn, E.R. Weber, *Ga vacancies in low-temperature-grown GaAs identified by slow positrons*, Appl. Phys. Lett. **71**, 638 (1997).

[10] P.M. Mooney, M.C. Tarun, V. Bahrami-Yekta, T. Tiedje, R.B. Lewis, M. Masnadi-Shirazi, *Defect energy levels in p-type GaAsBi and GaAs grown by MBE at low temperatures*, Semicond. Sci. Technol. **31**, 065007 (2016).

[11] P.M. Mooney, K.P. Watkins, Z. Jiang, A.F. Basile, R.B. Lewis, V. Bahrami-Yekta, M. Masnadi-Shirazi, D.A. Beaton, T. Tiedje, *Deep level defects in n-type GaAsBi and GaAs grown at low temperatures*, J. Appl. Phys. **113**, 13370 (2013).

[12] M. Henini, J. Ibáñez, M. Schmidbauer, M. Shafi, S. V. Novikov, L. Turyanska, S.I. Molina, D.L. Sales, M.F. Chisholm, J. Misiewicz, *Molecular beam epitaxy of GaBiAs on (311) B GaAs substrates*, Appl. Phys. Lett. **91**, 350 (2007).

[13] J.F. Rodrigo, D.L. Sales, M. Shafi, M. Henini, L. Turyanska, S. Novikov, S.I. Molina, *Effect of annealing on the structural and optical properties of (3 1 1)B GaAsBi layers*, Appl. Surf. Sci. **256**, 5688 (2010).

[14] P.K. Patil, F. Ishikawa, S. Shimomura, *GaAsBi/GaAs MQWs MBE growth on (411) GaAs substrate*, Superlattices Microstruct. **100**, 1205 (2016).

[15] G.A. Prando, V. Orsi Gordo, J. Puustinen, J. Hilska, H.M. Alghamdi, G. Som, M. Gunes, M. Akyol, S. Souto, A.D. Rodrigues, H.V.A. Galeti, M.

Henini, Y.G. Gobato, M. Guina, *Exciton localization and structural disorder of GaAs1-xBix/GaAs quantum wells grown by molecular beam epitaxy on (311)B GaAs substrates*, Semicond. Sci. Technol. **33**, 084002 (2018).

[16] J.A. Steele, R.A. Lewis, M. Henini, O.M. Lemine, A. Alkaoud, *Raman scattering studies of strain effects in (100) and (311)B GaAs 1-xBix epitaxial layers*, J. Appl. Phys. **114**, 193516 (2013).

[17] R.N. Kini, L. Bhusal, A.J. Ptak, R. France, A. Mascarenhas, *Electron Hall mobility in GaAsBi*, J. Appl. Phys. **106**, 04370 (2009).

[18] R.L. Field, J. Occena, T. Jen, D. Del Gaudio, B. Yarlagadda, C. Kurdak, R.S. Goldman, *Influence of surface reconstruction on dopant incorporation and transport properties of GaAs(Bi) alloys*, Appl. Phys. Lett. **109** (2016) 252105.

[19] M. Yoshimoto, M. Itoh, Y. Tominaga, K. Oe, *Quantitative estimation of density of Bi-induced localized states in GaAs1−xBix grown by molecular beam epitaxy*, J. Cryst. Growth. **378**, 73 (2013).

[20] M.A. Stevens, S. Lenney, J. McElearney, K.A. Grossklaus, T.E. Vandervelde, *Characterization of tellurium and silicon as n-type dopants for GaAsBi*, Semicond. Sci. Technol. **35**, 105006 (2020).

[21] B.A. Aronzon, M. V. Kovalchuk, E.M. Pashaev, M.A. Chuev, V. V. Kvardakov, I.A. Subbotin, V. V. Rylkov, M.A. Pankov, I.A. Likhachev, B.N. Zvonkov, Y.A. Danilov, O. V. Vihrova, A. V. Lashkul, R. Laiho, *Structural and transport properties of GaAs/δ-Mn/GaAs/In xGa1-xAs/GaAs quantum wells*, J. Phys. Condens. Matter. **20**, 145207 (2008).

[22] D.K. Bowen, B.K. Tanner, *High Resolution X-Ray Diffractometry And Topography*, (CRC Press, 2005).

[23] L. Vegard, *Die Konstitution Der Mischkristalle Und Die Raumfüllung Der Atome*, Zeitschrift Für Phys. **5**, 17 (1921).

[24] M. Ferhat, A. Zaoui, *Structural and electronic properties of III-V bismuth compounds*, Phys. Rev. B. **73**, 115107 (2006).

[25] R.H. Mari, M. Shafi, M. Henini, D.Taylor, *Laplace DLTS of molecular beam epitaxy GaAs grown on (100) and (211)B substrates*, Phys. Status Solidi. **12**, 2873 (2009).

[26] R.H. Mary, *Electrical characterisation of defects in III-V compound semiconductors by DLTS*. (University of Nottingham, 2011).

[27] S.M. Sze, K.K. Ng, *Physics of Semiconductor Devices*. (John Wiley & Sons, 2006).

[28] M. Biber, C. Coşkun, A. Türüt, *Current-voltage-temperature analysis of inhomogeneous Au/n-GaAs Schottky contacts*, Eur. Phys. J. Appl. Phys. **31**, 79 (2005).

[29] J.H. Werner, *Schottky barrier and pn-junctionI/V plots-Small signal evaluation*, Appl. Phys. A. **47**, 291 (1988).

[30] C.J. Hunter, F. Bastiman, A.R. Mohmad, R. Richards, J.S. Ng, S.J. Sweeney, J.P.R. David, *Absorption characteristics of GaAs1-xBix/GaAs Diodes in the Near-Infrared*, IEEE Photonics Technol. Lett. **24**, 2191 (2012).

[31] B. Şahin, H. Çetin, E. Ayyildiz, *The effect of series resistance on*

capacitance–voltage characteristics of Schottky barrier diodes, Solid State Commun. **135**, 490 (2000).

[32] E.H. Rhoderick, *Metal-semiconductor contacts*, IEE Proc. I-Solid-State Electron Devices. **129,** 1 (1982).

[33] N. Al Saqri, J.F. Felix, M. Aziz, D. Jameel, C.I.L. de Araujo, H. Albalawi, F. Al Mashary, H. Alghamdi, D. Taylor, M. Henini, *Investigation of the effects of gamma radiation on the electrical properties of dilute GaAs1−xNx layers grown by Molecular Beam Epitaxy*, Curr. Appl. Phys. **15,** 1230 (2015).

[34] N. Yildirim, H. Korkut, A. Türüt, *Temperature-dependent Schottky barrier inhomogeneity of Ni/n-GaAs diodes*, Eur. Phys. J. Appl. Phys. **45**, 10302 (2009).

[35] C. Dong, X. Han, X. Gao, Y. Ohshita, M. Yamaguchi, *Electrical characterization of Cu Schottky contacts to n-type GaAsN grown on (311)A/B GaAs substrates*, J. Alloys Compd. **657,** 325 (2016).

[36] V. Narayanamurti, M. Kozhevnikov, H.P. Xin, C.W. Tu, A. Mascarenhas, Y. Zhang, *Nitrogen-induced evolution of GaAs 1-x N x studied by ballistic electron emission spectroscopy*, National Renewable Energy Lab.(NREL). (2000).

[37] R. Kudrawiec, P. Poloczek, J. Misiewicz, M. Shafi, J. Ibáñez, R.H. Mari, M. Henini, M. Schmidbauer, S.V. Novikov, L. Turyanska, S.I. Molina, D.L. Sales, M.F. Chisholm, *Photomodulated transmittance of GaBiAs layers grown on (001) and (311)B GaAs substrates*, Microelectronics Journal. **40,**

537 (2009).

[38] J.V.V.N.K. Rao, S.V. Reddy, S.S. Naik, *Electrical Characteristics of Rapid Thermal Annealing Effects on Co-polymer of Au / P (VDC-MA)/ n-type InP Schottky Structures*, Int. J. Res. Stud. Sci. Eng. Technol. **3,** 29 (2016).

[39] X. Han, C. Dong, Q. Feng, Y. Ohshita, M. Yamaguchi, *Growth orientation dependence of Si doping in GaAsN*, J. Appl. Phys. **117**, 05570 (2015).

[40] D. V. Lang, *Deep-level transient spectroscopy: A new method to characterize traps in semiconductors*, J. Appl. Phys. **45**, 3023 (1974).

[41] L. Dobaczewski, A.R. Peaker, K. Bonde Nielsen, *Laplace-transform deep-level spectroscopy: The technique and its applications to the study of point defects in semiconductors*, J. Appl. Phys. **96**, 4689 (2004).

[42] D. V. Lang, A.Y. Cho, A.C. Gossard, M. Ilegems, W. Wiegmann, *Study of electron traps in n -GaAs grown by molecular beam epitaxy,* J. Appl. Phys. **47**, 2558 (1976).

[43] K. Yokota, H. Kuchii, K. Nakamura, M. Sakaguchi, H. Takano, Y. Ando, *EL2, EL3, and EL6 defects in GaAs highly implanted with sulfur*, J. Appl. Phys. **88**, 5017 (2000).

[44] Z.Q. Fang, T.E. Schlesinger, A.G. Milnes, *Evidence for EL6 (Ec- 0.35 eV) acting as a dominant recombination center in n-type horizontal Bridgman GaAs*, J. Appl. Phys. **61**, 5047 (1987).

[45] G. Luo, S. Yang, G.R. Jenness, Z. Song, T.F. Kuech, D. Morgan, *Understanding and reducing deleterious defects in the metastable alloy*

GaAsBi, NPG Asia Mater. **9,** e345 (2017).

[46] P. Blood, J.J. Harris, *Deep states in GaAs grown by molecular beam epitaxy*, J. Appl. Phys. **56**, 993 (1984).

[47] A.Z. Li, H.K. Kim, J.C. Jeong, D. Wong, T.E. Schlesinger, A.G. Milnes, *Trap suppression by isoelectronic In or Sb doping in Si-doped n -GaAs grown by molecular-beam epitaxy*, J. Appl. Phys. **64**, 3497 (1988).

[48] P.M. Mooney, M. Tarun, D.A. Beaton, A. Mascarenhas, K. Alberi, *Deep level defects in dilute GaAsBi alloys grown under intense UV illumination*, Semicond. Sci. Technol. **31**, 085014 (2016).

[49] J. Lagowski, D.G. Lin, T. -P. Chen, M. Skowronski, H.C. Gatos, *Native hole trap in bulk GaAs and its association with the double-charge state of the arsenic antisite defect*, Appl. Phys. Lett. **47**, 929 (1985).

[50] T. Fuyuki, S. Kashiyama, Y. Tominaga, K. Oe, M. Yoshimoto, *Deep-hole traps in p-type GaAs1-xBix grown by molecular beam epitaxy*, Jpn. J. Appl. Phys. **50**, 080203 (2011).

[51] R. Loudon, *The Raman effect in crystals*, Adv. Phys. **13**, 423 (1964).

[52] R. Merlin, A. Pinczuk, W.H. Weber, *Overview of Phonon Raman Scattering in Solids, in Raman Scattering in Materials Science*, edited by R. Merlin and W. H. Weber. (Springer, New York, 2000).

[53] J.A. Steele, P. Puech, and R.A. Lewis, *Polarized Raman backscattering selection rules for (hhl)-oriented diamond- and zincblende-type crystals*, J. Appl. Phys. **120**, 05570 (2016).

[54] J. A. Steele, *Structural and Optical Studies of GaAs1-XBix and p-Bi203 for Optoelectronic Devices*. (University of Wollongong, 2015).

[55] E. Tisbi, E. Placidi, R. Magri, P. Prosposito, R. Francini, A. Zaganelli, S. Cecchi, E. Zallo, R. Calarco, E. Luna, J. Honolka, M. Vondráček, S. Colonna, F. Arciprete, *Increasing Optical Efficiency in the Telecommunication Bands of Strain-Engineered Ga(As,Bi) Alloys*, Phys. Rev. Appl. **14**, 014028 (2020).

[56] P. Verma, K. Oe, M. Yamada, H. Harima, M. Herms, G. Irmer, *Raman Studies on GaAs1−xBi x and InAs1−xBix*, J. Appl. Phys. **89**, 1657 (2001).

[57] M.J. Seong, S. Francoeur, S. Yoon, A. Mascarenhas, S. Tixier, M. Adamcyk, T. Tiedje, *Bi-induced vibrational modes in GaAsBi*, Superlattices Microstruct. **37**, 394 (2005).

[58] F. Sarcan, Ö. Dönmez, K. Kara, A. Erol, E. Akalın, M. Çetin Arıkan, H. Makhloufi, A. Arnoult, C. Fontaine, *Bismuth-induced effects on optical, lattice vibrational, and structural properties of bulk GaAsBi alloys*, Nanoscale Res. Lett. **9**, 119 (2014).

[59] R.S. Joshya, V. Rajaji, C. Narayana, A. Mascarenhas, R.N. Kini, *Anharmonicity in light scattering by optical phonons in GaAs1-xBix*, J. Appl. Phys. **119**, 20570 (2016).

[60] J. Li, K. Forghani, Y. Guan, W. Jiao, W. Kong, K. Collar, T.H. Kim, T.F. Kuech, and A.S. Brown, *GaAs1-yBiy Raman signatures: Illuminating relationships between the electrical and optical properties of GaAs1-yBiy and Bi incorporation*, AIP Adv. **5**, 067103 (2015).

[61] A. Erol, E. Akalin, K. Kara, M. Aslan, V. Bahrami-Yekta, R.B. Lewis, T. Tiedje, *Raman and AFM studies on nominally undoped, p- and n-type GaAsBi alloys*, J. Alloys Compd. **722**, 339 (2017).

[62] R. Kudrawiec, M. Syperek, P. Poloczek, J. Misiewicz, R.H. Mari, M. Shafi, M. Henini, Y.G. Gobato, S. V. Novikov, J. Ibáñez, M. Schmidbauer, S.I. Molina, *Carrier localization in GaBiAs probed by photomodulated transmittance and photoluminescence*, J. Appl. Phys. **106**, 02351 (2009).

[63] M. Usman, C.A. Broderick, A. Lindsay, E.P. O'Reilly, *Tight-binding analysis of the electronic structure of dilute bismide alloys of GaP and GaAs*, Phys. Rev. B - Condens. Matter Mater. Phys. **84**, 245202 (2011).

[64] O.M. Lemine, A. Alkaoud, H. V. Avanço Galeti, V. Orsi Gordo, Y. Galvão Gobato, H. Bouzid, A. Hajry, M. Henini, *Thermal annealing effects on the optical and structural properties of (1 0 0) GaAs1-xBix layers grown by Molecular Beam Epitaxy*, Superlattices Microstruct. **65**, 48 (2014).

[65] S. Mazzucato, P. Boonpeng, H. Carrère, D. Lagarde, A. Arnoult, G. Lacoste, T. Zhang, A. Balocchi, T. Amand, X. Marie, C. Fontaine, *Reduction of defect density by rapid thermal annealing in GaAsBi studied by time-resolved photoluminescence*, Semicond. Sci. Technol. **28**, 022001 (2013).

CHAPTER 7: INVESTIGATION OF THE EFFECT OF GAMMA RADIATION ON THE ELECTRICAL AND OPTICAL PROPERTIES OF DILUTE N-TYPE GaAs$_{1-x}$Bi$_x$ GROWN on (100) GaAs SUBSTRATES BY MOLECULAR BEAM EPITAXY

This chapter reports the effect of gamma radiation dose on the electrical and optical properties of dilute GaAsBi layers having Bi composition x = ~5.4%, grown by MBE on a highly doped (100) GaAs substrates. Gamma radiation (γ-) was found to influence the electrical and optical properties of GaAsBi Schottky diodes. In particular, the radiation effect on the Current- Density (J-V) was more pronounced in the samples irradiated with a high dose, with a reduction of five times compared to as-grown samples. Additionally, the irradiated samples showed lower ideality factor, and higher barrier height, than as-grown samples. However, C-V characteristics exhibited an increase in the free carrier concentration in all irradiated samples as compared to as-grown structures, indicating an improvement in diode performance. DLTS revealed that after irradiation the number of electrically active traps decreased. Four, three and two electron traps were detected in as-grown, and 50 kGy and 100 kGy doses irradiated samples, respectively. The photoluminescence intensity of the main peak was found to increase with the irradiation dose, evidencing an enhancement of the optical properties and annihilation/ contributions of Bi- related traps, and supporting the electrical results.

7.1 INTRODUCTION

In general, defects and impurities in semiconductor materials and devices can deteriorate their optical and electrical properties. For example, some defects which act as non-radiative recombination centres, have a significant impact on the quality and performance of both the epitaxial layers and the device characteristics. Post-growth treatments, such as thermal annealing and hydrogenation processes, are well known to reduce the concentration of defects, annihilate and passivate completely defects. In addition, exposing semiconductor materials to high gamma-radiation has been found to enhance their performances. However, a significant number of lattice defects are produced in semiconductors as a result of radiation in space, which degrade the devices' performance.

Several factors such as metal and semiconductor work functions, type of semiconductor material, metallization processing procedures, doping concentrations of semiconductor materials and the presence of defects states have been reported to affect the electrical properties of Schottky diode contacts [1]. Additionally, exposure of semiconductor materials to radiation has been found to modify the atomic configuration and induce other defects into the lattice, which therefore alters their electrical and optical properties [2]. A recent study by Tamotsu H. et al. [2] showed the effect of gamma irradiation on deep electron states in liquid encapsulated Czochralski (LEC) grown GaAs, using DLTS. They reported that the irradiation reduced the concentration of EL6 trap by a factor of 3-5, whilst EL3 trap density was increased by an order of magnitude. B. Bouzazi et al. [3] employed DLTS technique to study the effect of electron irradiation and proton hydrogenation on the electrical properties of GaAsN Schottky diodes grown by CBE and the main nitrogen related nonradiative recombination centre E1, with level energy located at 0.33 eV below the conduction band. The origin of E1 trap formation was attributed to the compensation of the tensile strain in the film caused by the small atomic size of N atom to that of As atom. They found that the concentration of E1 increased with the fluence dose of electron irradiation. More recently, N. Al Saqri et al. [4] used DLTS and LDLTS measurements to investigate the effect of gamma (γ-) irradiation on dilute GaAsN layers with different nitrogen concentrations ranging from 0.2 to 1.2% grown on n^+ GaAs substrates by MBE. In this study, they reported that after irradiation, the number of traps either reduced, remained the same, or additional traps were created. Additionally, they observed that the density of some traps and their capture cross sections increased by about two orders of magnitude.

In the past, several groups have investigated the effect of radiation treatment on the metal/semiconductor Schottky diodes using different radiation sources such as irradiation with electron [5], neutron [6], swift heavy ions [7] and gamma radiations [4,8]. However, gamma irradiation effects on $GaAs_{1-x}Bi_x$ Schottky devices have not been investigated yet. Thus, from the fundamental and application viewpoint, the effect of gamma irradiation on the electrical characteristics of semiconductor based devices such as Schottky barrier diodes is extremely important due to their use in satellites, as well as in the development of particle detectors, and for radiation applications in space. Additionally, studying the defects caused by irradiation can provide useful information for fabricating radiation detectors systems. However, since $GaAs_{1-x}Bi_x$ is a new material the effects of gamma irradiation on electrically active defects are not reported yet. Consequently, an investigation of the formation and/or passivation of charge carrier traps by gamma irradiation in dilute $GaAs_{1-x}Bi_x$ layers can contribute to a better understanding of the behavior of Bi incorporation into the GaAs host lattice. In this work, the influence of gamma irradiation dose on the electrical and optical properties of n-type $GaAs_{1-x}Bi_x$ samples grown by MBE on (100) n^+ GaAs substrates are thoroughly investigated using different techniques including I-V, C-V, DLTS and PL.

7.2 SAMPLE DETAILS

In this work, the samples utilised are silicon-doped n-type $GaAs_{1-x}Bi_x$ (x=5.4% as determined by XRD) epilayers grown on highly doped (100) n+GaAs substrates by MBE at low temperature (~400°C) [9]. The structure of the (100) samples was presented in Chapter 6 (section 6.2.) and illustrated in Figure 6.1. A large sample was cleaved into three pieces for different irradiation doses (0, 50 and 100) kGy. The metallisation fabrication procedure and the electrical characterization techniques used to investigate these devices are similar to those presented in Chapter 6. The samples were then irradiated with a gamma cell Cobalt Irradiator (dose rate of 1.3 kGy/h) at different doses of 50 and 100 kGy in the Institute of Physics at the University of Brasília, Brazil. PL spectra of all $GaAs_{1-x}Bi_x$ samples were investigated as a function of laser power and temperature using a Janis closed-loop helium cryostat. The samples were excited with a 532 nm green laser. Prior to exposing the samples to Gamma irradiation, all the samples were checked for uniformity using PL measurements. The PL signal was collected in a 0.5 m Andor monochromator fitted with an InGaAs detector.

7.3 RESULTS AND DISCUSSION

7.3.1 CURRENT – VOLTAGE (I-V) CHARACTERSTICS

The I-V characteristics as a function of temperature (200-340 K with 20 K intervals) were measured for as-grown and irradiated samples in order to extract the diode parameters such as ideality factor (n), barrier height (ϕ_b) and series resistance (R_s). Fig. 7.1 (a) shows the room temperature semi-logarithmic current density - voltage (J-V) plot for as-grown and irradiated samples. All samples show a relatively low leakage current density. It can be seen clearly from Fig. 7.1 that the irradiated samples exhibit a lower reverse and forward current density compared to as-grown samples. In particular, the reverse current density at -4 V for as-grown and 50kGy and 100kGy irradiated samples are ~ 0.015 A/cm^{-2}, and 6x10^{-3} A/cm^{-2} and 3x10^{-3} A/cm^{-2}, respectively. It is worth mentioning that the samples with greater irradiation dose (i.e.100kGy), the effect was more pronounced where the leakage current density decreased by a factor of five as compared to as-grown samples. This reduction in reverse current density with increasing irradiation dose indicates that the radiation improved the electrical characteristics of the devices, as will be demonstrated in next sections by comparing the characteristic parameters of the devices extracted from I-V measurements. Additionally, the devices with lower reverse current may have defects with lower densities or the deep level defects act as a generation-recombination centers and play a role of carrier recombination in the reverse current characteristics [10,11]. These assumptions will be tested further using DLTS.

Additionally, to complement the results, Fig. 7.1 (b) shows the linear plots of all samples. The increase of the turn-on voltage, V_{on}, of the irradiated samples, could be related to decrease of the number of electrically active defects. However, many other effects could contribute to this behavior [12]. Most importantly, these results are consistent with those reported in the literature and as well as with the DLTS data presented in this work [13]. Indeed, Aziz et al. [12] showed that the number of defects detected by DLTS increases with the decrease of V_{on}, however, in this work the number of defects measured by DLTS decreases and V_{on} increases.

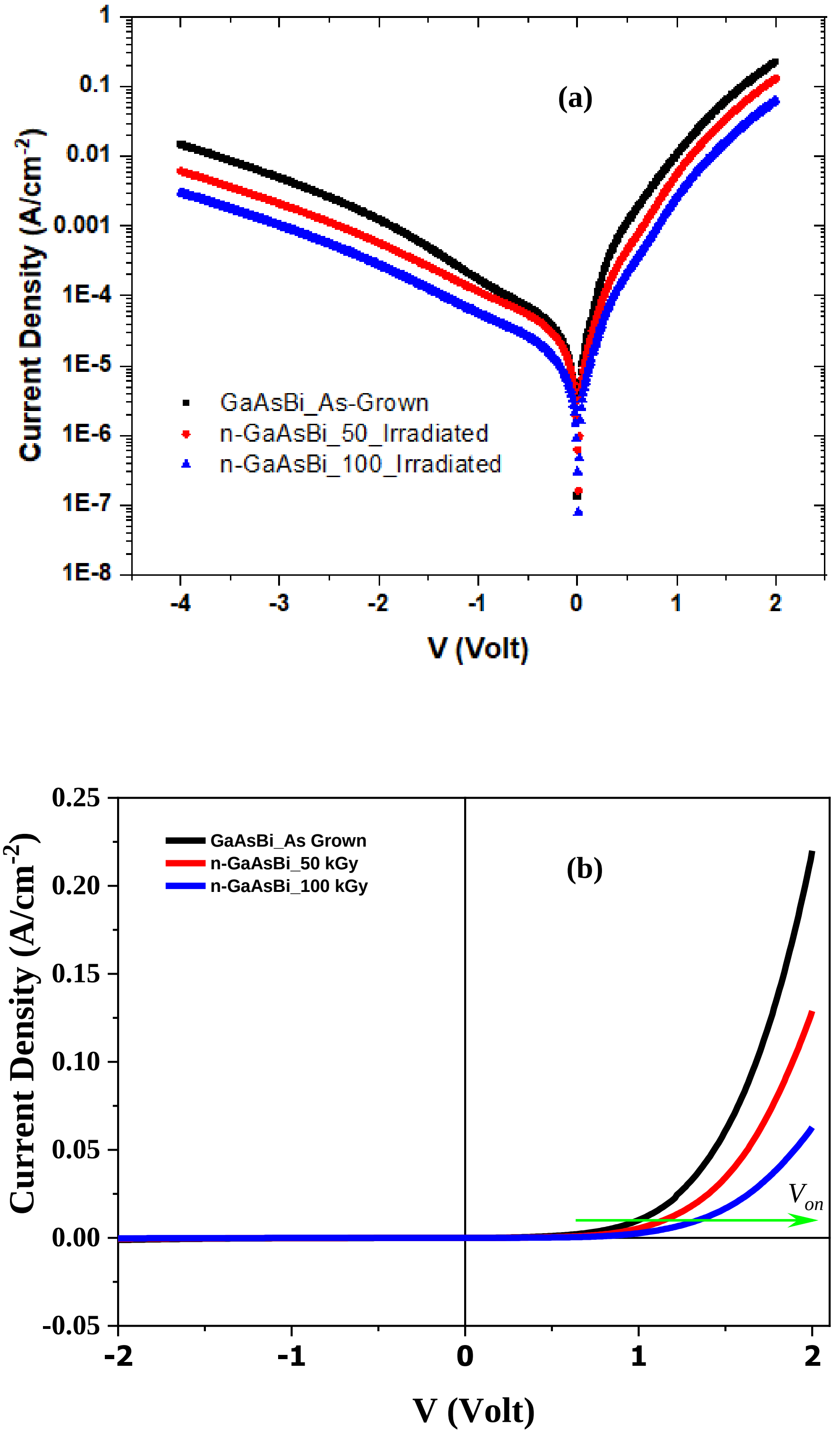

Fig. 7.1: (a) Room temperature semi-logarithmic plots of dark (J-V) characteristics of as-grown and irradiated samples. (b) Linear I–V plots showing the turn-on voltage (V_{on}) increases as a function of the radiation dose.

To gain a better understanding, a further analysis will be presented to bring some clarity on these devices. The I-V characteristics of the diodes can be described by the thermionic emission model [14], as described in Chapter 6, section (6.3.2.1).

Series resistance, ideality factors and barrier height for as-grown and irradiated samples are obtained from the forward I-V characteristics at room temperature. These parameters are summarized in Table 7.1. Fig. 7.2 illustrates the temperature dependence of the ideality factor and barrier height as determined from the I-V characteristic for as-grown and irradiated samples with different gamma dose of 50 kGy and 100 kGy over a temperature range from 200 K to 340 K.

Table 7.1. Experimental data of ideality factor (n), barrier height (ϕ_B) and series resistance (R_S), obtained from dark I-V characteristics at room temperature for as-grown and irradiated samples.

Sample	n	ϕ_B (eV)	R_S (kΩ)
As- grown	2.33±0.01	0.67±0.01	36.30±0.01
50 kGy	2.12±0.02	0.68±0.02	398.87±1.03
100 kGy	1.56±0.01	0.71±0.01	186.19±1.01

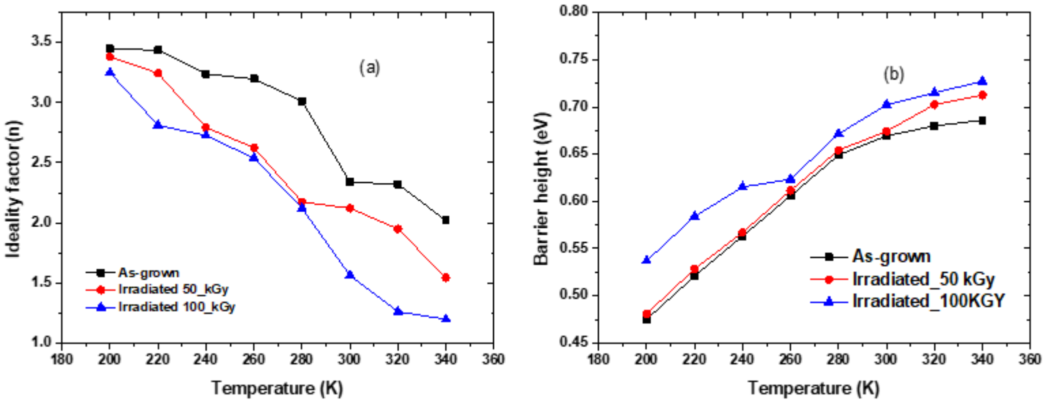

Fig. 7.2: Temperature dependence of (a) ideality factor (n), (b) barrier height (ϕ_b) of as-grown and irradiated n-type GaAsBi samples.

As can be seen from Table 7.1, the ideality factor of all as-grown and irradiated samples in forward bias deviates from unity, but it is important to note that the ideality factor values show a tendency to approach the unit value as the radiation dose is increased. Indeed, the ideality factor greater than unity implies that there is significant generation-recombination in the depletion region, which is the dominant current mechanism [15,16]. It is worth mentioning that such deviation of the ideality factor from unity can be ascribed to a number of factors, such as inhomogeneity of Schottky barrier height, series resistance, interface states and nonuniformity of interfacial charges [4,17,18].

Therefore, as n is decreasing as a result of radiation, one can assume that the radiation is acting on one or more of these factors. Additionally, from Fig. 7.2 (a and b) the experimental values of barrier height ϕ_b of all as-grown and irradiated samples increase with increasing temperature, whereas the values of ideality factor decrease. Furthermore, Table 7.1 shows that the barrier height of the Schottky diodes increases as the gamma dose increases at room temperature. This increment in barrier height was also observed by Ö. Güllü et al. [10,19] after gamma irradiation in Schottky diodes. They attributed this increase in barrier height to the effect of gamma irradiation process on the defects within the band gap of the metal-semiconductor structure investigated. This process is likely to have an impact on the free carrier concentration which results in an increase or decrease of barrier height in semiconductors structures. Hence, the increase in barrier height can be correlated with a modification of carrier concentration at Schottky interfaces caused by gamma irradiation [11]. On the other hand, it is apparent from Table 7.1 and Fig. 7.2(a) that the ideality factor of the 50kGy and 100kGy irradiated samples are lower than that of as-grown. The respective values of n obtained for 50kGy and 100kGy samples are 2.12±0.02 and 1.56±0.01 respectively, whereas it is 2.33±0.01 for the as-grown samples. This reduction in ideality factor in the irradiated samples in addition to the low reverse current density indicate an improvement in the quality of the devices compared with as-grown samples. It is well known that a reduction in interface defect density will increase the number of charge carrier, which leads to a decrease in the leakage current. Therefore, the quality of the diodes would be enhanced due to the improvement in the overall diode parameters [11].

7.3.2 CAPACITANCE – VOLTAGE CHARACTRISTICS

The C-V measurements were carried out at room temperature with a frequency of 1 MHz to obtain the background doping concentration (N_d). Fig. 7.3 (a) displays the experimental values of carrier concentration N_d determined from the slope of $1/C^2$ as a function of reverse bias voltage V for all as-grown and irradiated samples. It can be seen from Fig. 7.3 (a) that the plot of $1/C^2$ versus V are straight lines, indicating that the doping profiles of all samples (before and after irradiation) are homogeneous over the depletion region ~ 0.46 to 0.52 µm corresponding to reverse biases ranging from ~ 0 to -0.5 V. The free carrier concentration of as-grown and irradiated samples (50kGy, 100kGy) are ~1.03×10^{16} cm^{-3}, and 1.11×10^{16} cm^{-3} and 2.84×10^{16} cm^{-3}, respectively. The inset of Fig. 7.3 (a) shows that the doping concentration (N_d) values increase with increasing the dose of irradiation, which is in agreement with the I-V results. Similar observations of the increase of the carrier concentration have been reported by B. Bouzazi et al.[3] for GaAsN diodes grown by CBE subjected to proton and electron irradiation with different doses.

They attributed this increase to the ionization phenomenon and the formation of new donor and/or acceptor-like states. Furthermore, Fig. 7.3 (b) shows typical plot of Capacitance/Area (C/A) versus V for all samples at room temperature. It can be seen from this figure that after irradiation the C/A values decreased in samples irradiated with low dose (50 kGy), however, for high dose (100 kGy) the C/A values increased. This variation in capacitance values could be attributed to partial loss of charge carriers in the Schottky junction as a result of irradiation [20]. While the I-V and C-V results indicate that radiation can help improve the electrical performance, in the next section DLTS, a powerful spectroscopic tool, will be used to investigate further the effects of gamma radiation on the electrically active defects. It is worth noting that radiation could cause an annihilation and/or creation of defects and affect their concentrations as the radiation dose increases.

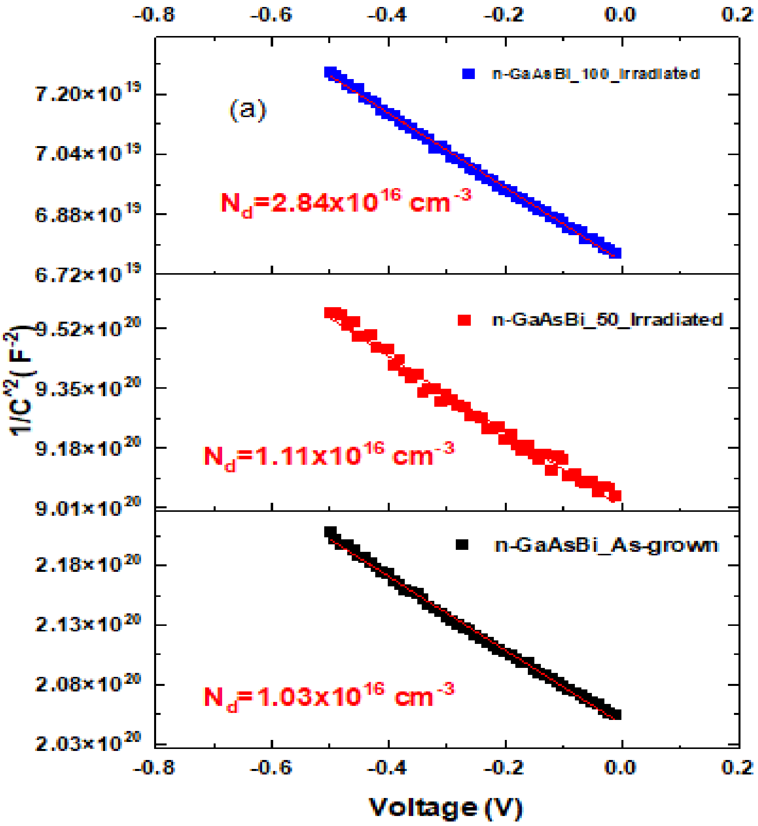

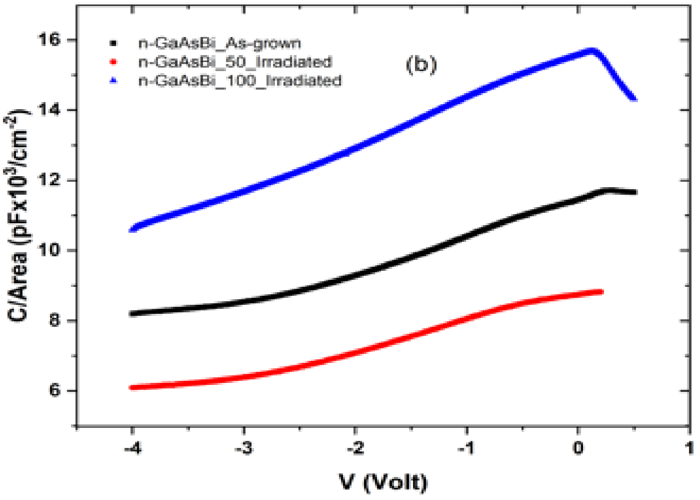

Fig. 7.3: (a) Plot of 1/C^2 versus bias voltage V for as-grown and irradiated (50, 100 kGy) n-GaAsBi Schottky diodes. (b) Typical plot of C/A versus V plots before and after irradiation for all samples at room temperature.

7.3.3 DLTS AND LDLTS CHARACTERSTICS.

In order to investigate the effect of gamma irradiation on the electrically active defects, DLTS measurements have been performed [21] over a temperature range from 100 K to 450 K. The DLTS experimental parameters utilised were a reverse bias (V_R) of -1 V, filling pulse voltage (V_P) of 0V with filling pulse time (t_p) of 1 msec and rate window of 200 s^{-1} for all investigated samples. Fig. 7.4 shows typical DLTS spectra of all samples. For as-grown samples, three positive peaks corresponding to three majority electron traps have been detected. In addition to the electron traps, a hole trap (negative peak) was also observed in as-grown sample. After irradiation, it is clear from Fig. 7.4 that as the gamma irradiation dose increases the number of traps decreases. In particular, for sample with 50 kGy dose three electron traps were observed, while only two electron traps were detected in sample irradiated with 100 kGy. In addition, LDLTS was employed to resolve the broad DLTS peaks [22] that could be caused by defects with closely spaced energy levels. The experimental parameters were similar to those used in the DLTS measurements. It is important to point out that no additional traps were detected by using LDLTS.

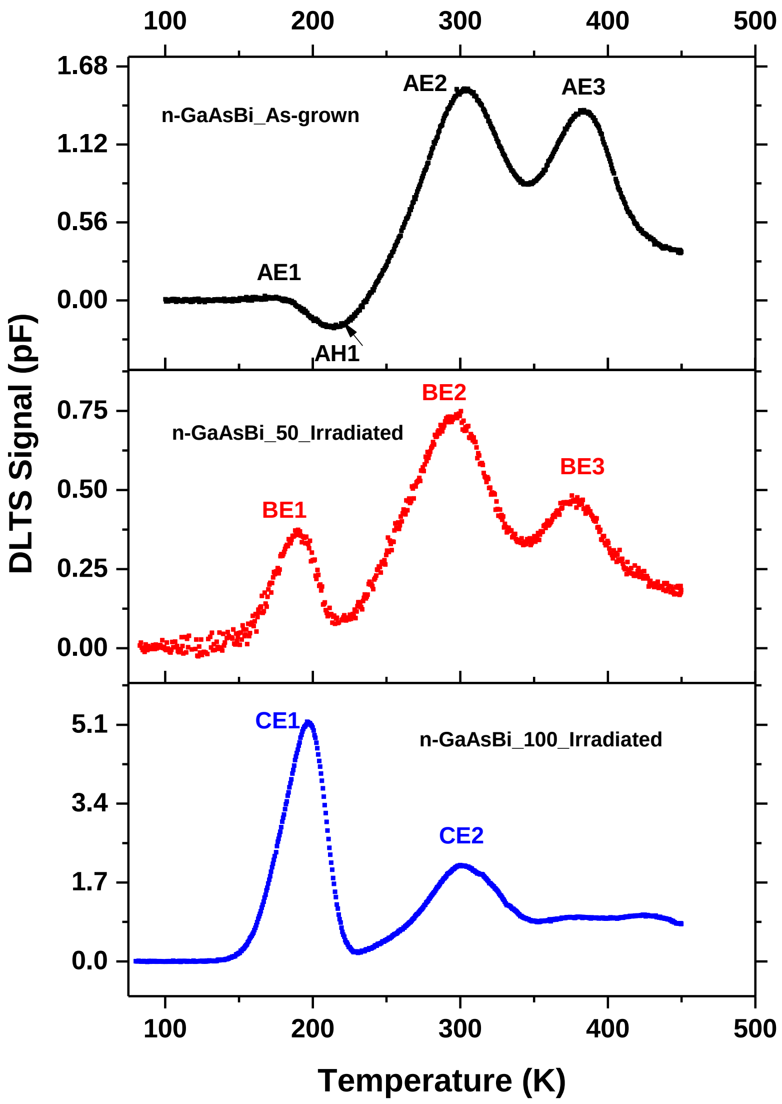

Fig. 7.4: Characteristic DLTS spectra of as-grown and irradiated samples with different dose of irradiation (50, 100 kGy). A, and B and C refer to as-grown, and 50 kGy and 100 kGy irradiated samples, respectively. E and H correspond to electron and hole traps, respectively.

Fig. 7.5 shows Arrhenius plots obtained from LDLTS for as-grown and irradiated samples subjected to gamma radiation with different doses. The activation energy, apparent cross section and concentration of the traps as determined from the slope and intercept of the Arrhenius plot are summarized in Table 7.2.

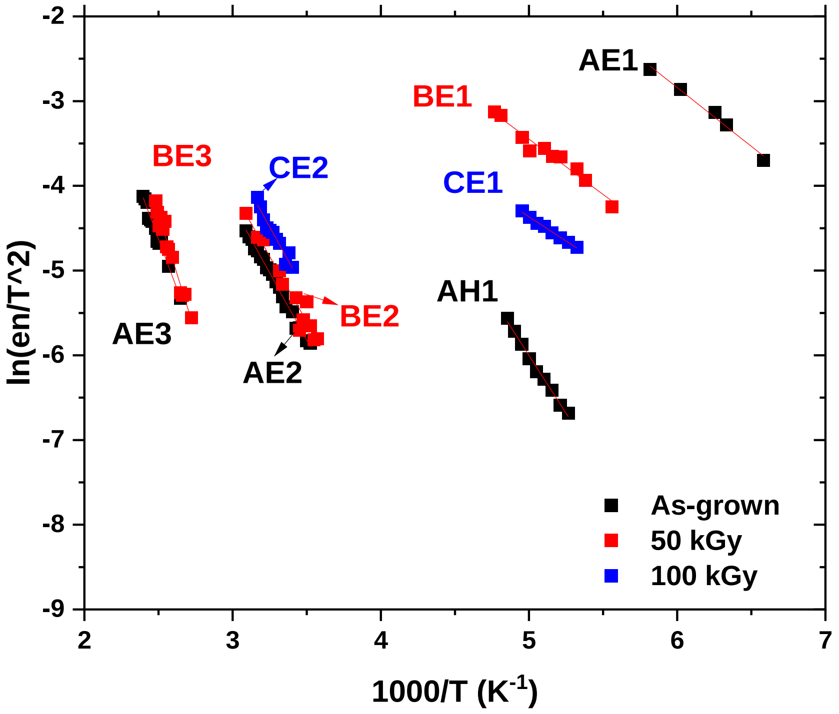

Fig. 7.5: Arrhenius plots obtained from LDLTS for as-grown and irradiated samples with different gamma doses. A, and B and C refer to as-grown, and 50 kGy and 100 kGy irradiated samples, respectively. E and H correspond to electron and hole traps, respectively.

Table 7.2. Traps parameters for as-grown and irradiated samples.

Sample	Trap Label	Activation Energy	Apparent capture cross-section (cm^{2})	Trap concentration (cm^{-3})
n-GaAsBi (as grown)	AE1	0.12±0.01	1.12x10^{-18}±0.1	1.2x10^{13}±0.1
	AH1	0.24±0.01	9.8x10^{-18}±0.8	5.1x10^{13}±0.3
	AE2	0.27±0.01	9.3x10^{-19}±0.9	7.7x10^{14}±0.5
	AE3	0.41±0.04	6.3x10^{-18}±0.7	9.7x10^{14}±0.4
n-GaAsBi (50 kGy)	BE1	0.11±0.01	1.0x10^{-19}± 0.4	4.6x10^{14}±0.5
	BE2	0.26±0.02	8.1x10^{-19}±0.6	6.5x10^{14}±0.3
	BE3	0.49±0.02	9.3x10^{-17}±0.7	4.9x10^{14}±0.1
n-GaAsBi (100kGy)	CE1	0.10±0.01	1.8x10^{-20}±0.1	6.3x10^{14}±0.6
	CE2	0.28±0.02	2.46x10^{-18}±0.1	6.5x10^{14}±0.1

Comparing activation energies and/or DLTS signals is one of the best method to identify those active traps introduced as a result of gamma irradiation. Hence, the observed traps are discussed and the results will be compared with previous works.

The traps AE1 (0.12±0.01 eV), BE1 (0.11±0.01 eV), CE1 (0.10±0.01 eV) observed in as-grown, 50kGy and 100kGy irradiated samples, respectively, are likely to correspond to the same traps labelled as ET_0 and ET_1 with activation energies ranging from 0.07 to 0.19eV [23] and A' with activation energy of 0.12 eV [24] reported previously. These defects were assigned to traps involving Bi as a constituent. It is worth noting, as shown in Table 7.2, that both the apparent capture cross section and concentration of these traps decreased and increased significantly, respectively. Traps AE2 and BE2 and CE2 with similar activation energies (0.26 - 0.27 eV) could be of the same origin, and they are present in as-grown and irradiated diodes. Similar traps labelled as ET_2 with activation energies in the range 0.29 to 0.33eV, were also observed in both GaAs and GaAsBi grown by MBE at low temperature by Gelczuk et al. [23]. This deep level trap can be ascribed to M_3 trap with energy (E_c-0.34 eV) [25,26] , and to EL6 trap reported in ref.[26]. The EL6 trap is usually related to complex pair defects involving arsenic antisite (As_{Ga}) and arsenic vacancy (V_{As}) [26] or to vacancy complex defect (V_{Ga} - V_{As}) [27]. Traps AE3 and BE3 with activation energy (0.41±0.04) and (0.49±0.02eV) eV, and concentrations of $9.7\text{x}10^{14}$ cm^{-3} and $4.9\text{x}10^{14}$ cm^{-3}, respectively, are the deepest traps observed in as-grown and 50kGy irradiated samples. However, this trap is not detected in the 100KGy irradiated samples, and therefore it could be annihilated when the sample was subjected to high dose of irradiation. A similar deep defect, labelled as trap C' [24] and trap ET3 [23] with activation energies varying from

0.45 to 0.52 eV [23], was detected in n-type GaAsBi samples grown at various temperatures, i.e. 330°C and 390°C. This deep level trap most likely corresponds to the trap level M4. The origin of M4 trap was related to an arsenic vacancy (V_{As}) complex involving an impurity [28]. However, since these defects are common in both as-grown and 50kGy irradiated samples, it is believed that these could be attributed to Bi-related defects. Indeed, the theoretical calculations reported by Luo et al [29], using density functional theory (DFT method), revealed the presence of a new complex defect $(V_{Ga} + Bi_{As})^{2-/3-}$ with an activation energy of (E_c- 0.36 eV), which is similar to traps AE3 and BE3 levels. This predicted defect of $(V_{Ga} + Bi_{As})^{2-/3-}$ is also consistent with recent DLTS measurements by Manuel F. et al [30], where they attributed their trap E2 with activation energies varying from 0.32 to 0.48 eV, to a complex defect involving Bi. Furthermore, as illustrated in Table 7.2, one DLTS peak, labelled as AH1 and with activation energy of ~ 0.24±0.01 eV, is detected only in the as-grown samples. AH1, which is associated with a hole emitting level, was reported recently in our previous work [9]. Its DLTS spectra is similar to those observed in p-type GaAsBi grown by MBE [31] and labelled as HT2 and HT3 with activation energies ranging from 0.23 eV to 0.43eV. These traps were assigned to As_{Ga} antisite or its relevant cluster. It is worth pointing out that the hole trap AH1 was not detected in the irradiated samples due to its annihilation by the radiation process. This could be due to the fact that bismuth is highly ionized, and therefore making it act as a donor dopant atom. This behaviour of ionization can be understood through a simple relationship analysis that involves the mass attenuation coefficient (μ) and reaction cross section, σ (cm^2), i.e, $\mu = N_0\sigma/A$, where N_0 is Avogadro's number (6.02×10^{23}) and A is the atomic weight of the absorber [32]. The cross section is the probability of a gamma ray interacting with a single atom. The atomic weight of bismuth, arsenic and gallium are A^{Bi} = 208.9804 u, A^{As} = 74.9216 u and A^{Ga} = 69.723 u, respectively, where u is the atomic mass unit. Therefore, the cross section of bismuth is around three times higher than that of arsenic and gallium (A^{Bi}/A^{As}~2.8 and A^{Bi}/A^{Ga} ~ 3.0). This means that gamma rays interact more strongly with bismuth atoms providing a compensation and annihilation process of defects. This also suggests that GaAs doped with high concentrations of bismuth could be used as a high-performance and high-sensitivity ionizing radiation detector.

7.3.4 OPTICAL PROPERTIES

To verify the effect of ionizing radiation on optical properties of GaAsBi samples, temperature dependent PL measurements were carried out. Fig. 7.6 shows the PL spectra for as-grown and irradiated samples with 50 kGys and 100 kGys doses at 10 K and with excitation power of 10mW. These results corroborate with both the I-V and the DLTS results. Indeed, as can be seen in Fig. 7.6, the PL intensity increases as the irradiation dose increases. This observation supports the I-V and DLTS results which showed a decrease in reverse current and number of electrically active defects, respectively. The PL results are also in good agreement with the C-V results that showed an increase in the carrier concentration with increasing irradiation doses.

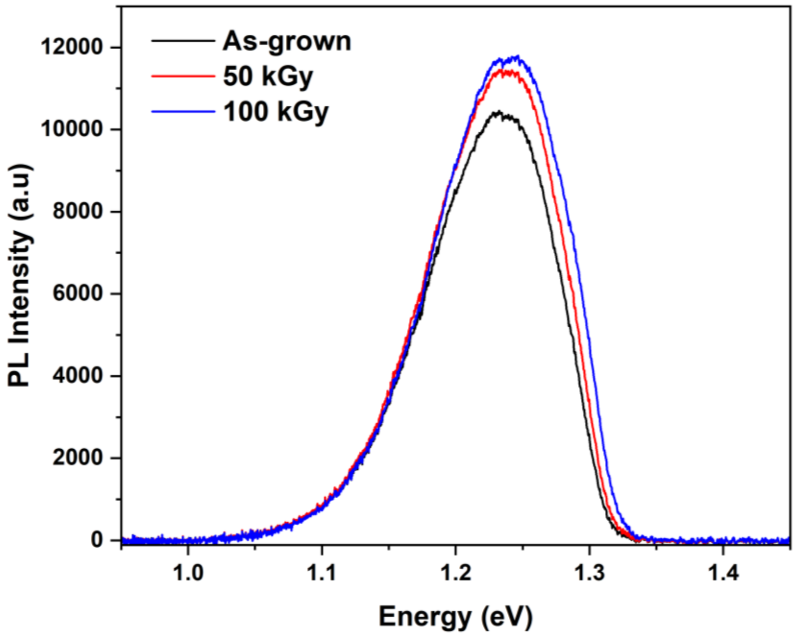

Fig. 7.6: PL spectra for as-grown and 50 kGy (red line) and 100 kGy (blue line) irradiated samples at 10 K and 10mW excitation laser power.

One possible explanation for all these new electrical and optical properties is that only bismuth atoms in GaAsBi lattice become highly ionized due to the ionizing effect of gamma irradiation, and therefore Bi will act as a donor dopant atom. As it is well-known and discussed in the previous section, the cross-section is strongly dependent on the atomic weight of the absorber, which explains the most high-A materials for X- or γ-rays detection and shielding [33]. The three fundamental mechanisms of electromagnetic for γ- rays interaction such as photo-absorption, Compton scattering, and electron-positron pair production are mostly dominant on bismuth atoms or cluster formed by Bi atoms. The presence of Bi cluster will be shown by analysing the temperature dependence of PL intensity with a modified Arrhenius equation [34–36], this equation was described in detials in Chapter 6, Section (6.3.3.2).

Fig. 7.7 shows a plot of integrated PL intensity (IPL) versus 1/ k_BT. The activation energies were obtained from Arrhenius fitting for as-grown and irradiated sample

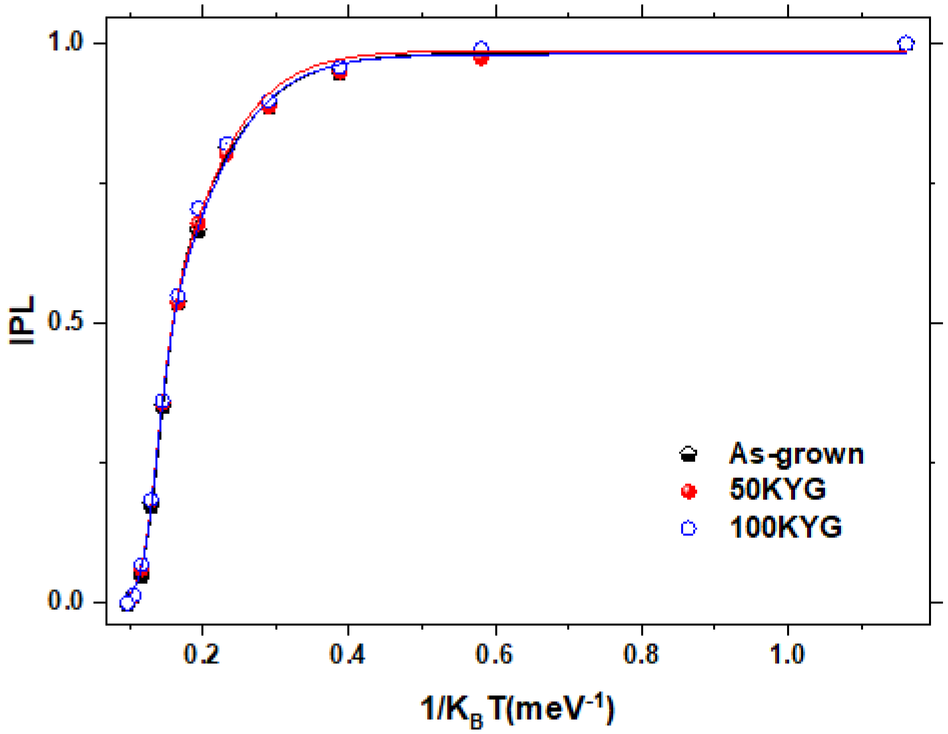

Fig. 7.7: Integrated PL (IPL) intensities as a function of inverse temperature of as-grown and irradiated samples at 10 mW laser excitation power, where the solid line is the best fit of the data.

The values of E_1 and E_2 for all samples are summarized in Table 7.3. The obtained activation energies indicate the formation of Bi clusters and alloy disorder for all samples [37]. Indeed, these two values of activation energies have been attributed to Bi cluster and Bi pair formation related to the lower activation energy value (E_1) and to the GaAsBi alloy disorder for higher activation energy value (E_2) [14, 40]. A recent study showed a very similar behaviour [34] for GaAs samples doped with Bi. Finally, these results not only indicate and contribute to a better understanding of the study of defects in Bi-doped GaAs, but also show that these samples can be used as efficient and very sensitive detectors of ionizing radiation. More interestingly, the detection of ionizing radiation could be monitored by both electrical and optical measurements, demonstrating the versatility of this material system.

Table 7.3. Arrhenius fitting parameters for as-grown and irradiated samples.

Sample	E_1 (meV)	E_2 (meV)
As- grown	20.22±3.05	95.84±4.12
50 kGy	16.94±2.23	97.60±4.32
100 kGy	16.55±3.16	99.58±4.03

7.4 CONCLUSION

The effect of gamma radiation dose on the electrically and optically active defects in n-type GaAsBi Schottky diode samples have been investigated using I-V, C-V, DLTS and PL techniques. It was found that samples exposed to the highest dose of gamma rays showed better diode performance. For example, the parameters such as ideality factor, barrier height and turn-on voltage as well as Current – Voltage and doping concentration have been studied. With increasing gamma dose, the ideality factor and leakage current decreased and the barrier height, turn-on voltage, and doping concentration increased. Indeed, the gamma irradiation caused an improvement in the electrical characteristics of the devices, as well as eliminating a number of electrically active traps. In addition, the optical results showed an enhancement in the PL peak intensity with increasing radiations doses, indicating a reduction of radiative centres which can also influence the photoluminescence properties of GaAsBi layers. As a conclusion, the results above indicate that these materials present high potential for applications in ionizing radiation detectors that could be monitored by both electrical and optical measurements.

REFERENCES

[1] I.P. Vali, P.K. Shetty, M.G. Mahesha, R. Keshav, V.G. Sathe, D.M. Phase, R.J. Choudhary, *Gamma irradiation effects on Al/n-Si Schottky junction properties*, Nucl. Instruments Methods Phys. Res. Sect. B: Beam Interaction with Materials and Atoms. **436**, 191 (2018).

[2] T. Hashizume, H. Hasegawa, *Variation of deep electron traps created by γ irradiation of GaAs*, J. Appl. Phys. **68**, 4598 (1990).

[3] B. Bouzazi, N. Kojima, Y. Ohshita, M. Yamaguchi, *Effect of electron and proton irradiation on recombination centers in GaAsN grown by chemical beam epitaxy*, Curr. Appl. Phys. **13**, 1269 (2013).

[4] N. Al Saqri, J.F. Felix, M. Aziz, D. Jameel, C.I.L. de Araujo, H. Albalawi, F. Al Mashary, H. Alghamdi, D. Taylor, M. Henini, *Investigation of the effects of gamma radiation on the electrical properties of dilute GaAs1−xNx layers grown by Molecular Beam Epitaxy*, Curr. Appl. Phys. **15**, 1230 (2015).

[5] S. Krishnan, G. Sanjeev, M. Pattabi, *Electron irradiation effects on the Schottky diode characteristics of p-Si*, Nucl. Instruments Methods Phys. Res. Sect. B Beam Interact. with Mater. Atoms. **266**, 621 (2008).

[6] Z. Lin, Z. Yimen, Z. Yuming, H. Chao, *Neutron radiation effect on 4H-SiC MESFETs and SBDs*, J. Semicond. **31**, 114006 (2010).

[7] A.T. Sharma, Shahnawaz, S. Kumar, Y.S. Katharria, D. Kanjilal, *Effects of swift heavy ion irradiation on the electrical characteristics of Au/n-GaAs*

Schottky diodes, Appl. Surf. Sci. **254**, 459 (2007).

[8] Ş. Karataş, A. Türüt, Ş. Altindal, *Effects of 60Co γ-ray irradiation on the electrical characteristics of Au/n-GaAs (MS) structures*, Nucl. Instruments Methods Phys. Res. Sect. A Accel. Spectrometers, Detect. Assoc. Equip. **555**, 260 (2005).

[9] S. Alhassan, D. de Souza, A. Alhassni, A. Almunyif, S. Alotaibi, A. Almalki, M. Alhuwayz, I.P. Kazakov, A. V. Klekovkin, V.I. Tsekhosh, I.A. Likhachev, E.M. Pashaev, S. Souto, Y.G. Gobato, N. Al Saqri, H.V.A. Galeti, F. Al mashary, H. Albalawi, N. Alwadai, M. Henini, *Investigation of the effect of substrate orientation on the structural, electrical and optical properties of n-type GaAs1−xBix layers grown by Molecular Beam Epitaxy*, J. Alloys Compd. **885**, 161019 (2021).

[10] Ö. Güllü, F. Demir, F.E. Cimilli, M. Biber, *γ-Irradiation-induced changes at the electrical characteristics of Sn/p-Si Schottky contacts*, Vacuum. **82**, 789 (2008).

[11] A. Bobby, N. Shiwakoti, S. Verma, P.S. Gupta, B.K. Antony, *Enhancement in electrical properties of Au/n-GaAs Schottky diodes exposed to 60Co gamma rays*, Mater. Sci. Semicond. Process. **21**, 116 (2014).

[12] Aziz, Mohsin, Philippe Ferrandis, Abdelmadjid Mesli, Riaz Hussain Mari, Jorlandio Francisco Felix, Azzouz Sellai, Dler Jameel et al. Deep-level transient spectroscopy of interfacial states in “buffer-free” pin GaSb/GaAs devices, Journal of Applied Physics **114**, 134507 (2013)

[13] Jallipalli, A., K. Nunna, M. N. Kutty, G. Balakrishnan, G. B. Lush, L. R. Dawson, and D. L. Huffaker, Compensation of interfacial states located inside the “buffer-free” GaSb/GaAs (001) heterojunction via δ-doping, Applied Physics Letters **95**, 072109 (2009).

[14] S.M. Sze, K.K. Ng, Physics of Semiconductor Devices. (John Wiley & Sons, 2006).

[15] Z. Zhou, D.F. Mendes, R.D. Richards, F. Bastiman, J.P. David, *Absorption properties of GaAsBi based p–i–n heterojunction diodes*, Semicond. Sci. Technol. **30**, 094004 (2015).

[16] C.J. Hunter, F. Bastiman, A.R. Mohmad, R. Richards, J.S. Ng, S.J. Sweeney, J.P.R. David, *Absorption characteristics of GaAs1-xBix/GaAs Diodes in the Near-Infrared*, IEEE Photonics Technol. Lett. **24**, 2191 (2012).

[17] B. Şahin, H. Çetin, E. Ayyildiz, *The effect of series resistance on capacitance–voltage characteristics of Schottky barrier diodes*, Solid State Commun. **135**, 490 (2000).

[18] E.H. Rhoderick, *Metal-semiconductor contacts*, IEE Proc. I-Solid-State Electron Devices. **129**, 1 (1982).

[19] Ö. Güllü, M. Çankaya, M. Biber, A. Türüt, *Gamma irradiation-induced changes at the electrical characteristics of organic-based Schottky structures*, J. Phys. D. Appl. Phys. **41**, 135103 (2008).

[20] S. Belahsene, N.A. Al Saqri, D. Jameel, A. Mesli, A. Martinez, J. De Sanoit, A. Ougazzaden, J.P. Salvestrini, A. Ramdane, M. Henini, *Analysis of deep*

level defects in GaN p-i-n diodes after beta particle irradiation, Electronics. **4**, 1090 (2015).

[21] D. V. Lang, *Deep-level transient spectroscopy: A new method to characterize traps in semiconductors*, J. Appl. Phys. **45**, 3023 (1974).

[22] L. Dobaczewski, A.R. Peaker, K. Bonde Nielsen, *Laplace-transform deep-level spectroscopy: The technique and its applications to the study of point defects in semiconductors*, J. Appl. Phys. **96**, 4689 (2004).

[23] Ł. Gelczuk, J. Kopaczek, T.B.O. Rockett, R.D. Richards, R. Kudrawiec, *Deep-level defects in n-type GaAsBi alloys grown by molecular beam epitaxy at low temperature and their influence on optical properties*, Sci. Rep. **7**, 12824 (2017).

[24] P.M. Mooney, K.P. Watkins, Z. Jiang, A.F. Basile, R.B. Lewis, V. Bahrami-Yekta, M. Masnadi-Shirazi, D.A. Beaton, T. Tiedje, *Deep level defects in n-type GaAsBi and GaAs grown at low temperatures*, J. Appl. Phys. **113**, 13370 (2013).

[25] D. V. Lang, A.Y. Cho, A.C. Gossard, M. Ilegems, W. Wiegmann, *Study of electron traps in n -GaAs grown by molecular beam epitaxy*, J. Appl. Phys. **47**, 2558 (1976).

[26] K. Yokota, H. Kuchii, K. Nakamura, M. Sakaguchi, H. Takano, Y. Ando, *EL2, EL3, and EL6 defects in GaAs highly implanted with sulfur*, J. Appl. Phys. **88**, 5017 (2000).

[27] Z.Q. Fang, T.E. Schlesinger, A.G. Milnes, *Evidence for EL6 (Ec- 0.35 eV)*

acting as a dominant recombination center in n-type horizontal Bridgman GaAs, J. Appl. Phys. **61**, 5047 (1987).

[28] P. Blood, J.J. Harris, *Deep states in GaAs grown by molecular beam epitaxy*, J. Appl. Phys. **56**, 993 (1984).

[29] G. Luo, S. Yang, G.R. Jenness, Z. Song, T.F. Kuech, D. Morgan, *Understanding and reducing deleterious defects in the metastable alloy GaAsBi*, NPG Asia Mater. **9**, E345 (2017).

[30] M. Fregolent, M. Buffolo, C. De Santi, S. Hasegawa, J. Matsumura, H. Nishinaka, M. Yoshimoto, G. Meneghesso, E. Zanoni, M. Meneghini, *Deep levels and carrier capture kinetics in n-GaAsBi alloys investigated by deep level transient spectroscopy,* J. Phys. D. Appl. Phys. **54**, 345109 (2021).

[31] T. Fuyuki, S. Kashiyama, Y. Tominaga, K. Oe, M. Yoshimoto, *Deep-hole traps in p-type GaAs1-xBix grown by molecular beam epitaxy*, Jpn. J. Appl. Phys. **50**, 080203 (2011).

[32] D.R. G. Nelson, "*Gamma-Ray Interactions with Matter"*, Passive Nondestructive Analysis of Nuclear Materials, **p. 27** (1991).

[33] W. Heitler, *The quantum theory of radiation. 3d ed*, Oxford: (Clarendon Press, 1954).

[34] H. Alghamdi, V.O. Gordo, M. Schmidbauer, J.F. Felix, S. Alhassan, A. Alhassni, G.A. Prando, H. Coelho-Júnior, M. Gunes, H.V.A. Galeti, Y.G. Gobato, M. Henini, *Effect of thermal annealing on the optical and structural properties of (311)B and (001) GaAsBi/GaAs single quantum wells grown*

by MBE, J. Appl. Phys. **127**, 125704 (2020).

[35] S. M. Olsthoorn, F. A. J. M. Driessen, A. P. A. M. Eijkelenboom, and L. J. Gilling, *Photoluminescence and photoluminescence excitation*, J. Appl. Phys. **73**, 7798 (1993).

[36] H.D. Sun, S. Calvez, M.D. Dawson, J.A. Gupta, G.C. Aers, G.I. Sproule, *Thermal quenching mechanism of photoluminescence in 1.55 μm GaInNAsSb/Ga(N)As quantum-well structures,* Appl. Phys. Lett. **89**, 101909 (2006).

[37] M. Usman, C.A. Broderick, A. Lindsay, E.P. O'Reilly, *Tight-binding analysis of the electronic structure of dilute bismide alloys of GaP and GaAs*, Phys. Rev. B. **84**, 245202 (2011).

CHAPTER 8: STRUCTURAL AND OPTICAL PROPERTIES OF N-TYPE AND P-TYPE $GaAs_{1-X}Bi_X$ THIN FILMS GROWN BY MOLECULAR BEAM EPITAXY ON (311)B GaAs SUBSTRATES

In this chapter, a study will be reported on the structural and optical properties of n-type Si-doped and p-type Be-doped $GaAs_{1-x}Bi_x$ thin films grown by MBE on (311)B GaAs substrates with nominal Bi content x=5.4%. Similar samples without Bi were also grown for comparison purposes (n-type GaAs and p-type GaAs). XRD, micro-Raman at room temperature, and PL measurements as a function of temperature and laser excitation power (P_{EXC}) were performed to investigate their structural and optical properties. XRD results revealed that the composition of Bi incorporated in both n-type and p-type doped GaAsBi was similar, despite that the samples present remarkable differences in the number of Bi related defects, non-radiative centers and alloy disorder. Particularly, the results evidence that the Bi-related defects in n- and p-doped GaAsBi alloys have important impact on the differences of their optical properties.

8.1 INTRODUCTION

The incorporation of Bi and N into the host lattice of GaAs perturbs the valence band and conduction band, respectively, and allows localised states to be formed [1]. Due to the strong carrier scattering at localized states, Bi alloys (GaAsBi) affects the hole density and mobility in GaAs, whereas N alloys (GaAsN) affects the electron density and mobility [2,3]. Charge-carrier mobility is a key parameter of the transport properties of semiconductor materials and is strongly related to the speed and performance of electronic devices. Cooke et al. [4] showed that the electron mobility in nominally undoped GaAsBi layers is relatively not affected by Bi incorporation. Moreover, Kini et al. [2] reported an investigation on the effect of Bi alloying on electron mobility using n-type (Si doped) GaAsBi epilayers. They observed that no significant degradation in electron mobility with Bi incorporation in GaAs, up to a concentration of 1.2%. However, at high Bi concentration (>1.6%) some degradation of electron mobility was observed. On the contrary, N incorporation in GaAs degrades the electron mobility even at low concentrations (~ 0.1%) [2]. The influence of Bi alloying in p-type GaAsBi on the hole mobility was also reported [3,5]. Kini et al. [3] presented a detailed study of the hole mobility in p-doped GaAsBi epilayers using Hall measurements. Their results showed that, unlike the electron mobility in GaAsBi, the hole mobility decreased with increasing Bi concentration. They suggested that the decrease in hole mobility is due to the hole scattering at the isolated state and the Bi-Bi pair states.

Several optical studies have been reported on undoped dilute bismide alloys, however, there are very few on intentionally doped (n-type and p-type) GaAsBi. It is well known that Bi incorporation into GaAs can create acceptor and/or donor levels due to the presence of Bi-related defects [6]. For n-doped and p-doped GaAsBi layers, Bi-induced levels are mainly electron traps [6] and hole traps [7], respectively. Therefore, the presence of different Bi generated traps could affect differently the optical properties of n-type and p-type layers, resulting for example in different shifts of the PL peak energy. PL measurements, which have been used to investigate n-type $GaAs_{1-x}Bi_x$ ($x<0.023$) grown on GaAs substrates by MBE [6], have shown that with the increase of Bi concentration the GaAsBi related PL peak redshifts to lower energies.

In addition, they reported another contribution to the PL spectra which was related with the optical transition between Bi induced donor trap (DT) and valence band (VB). Furthermore, an emission band was observed and associated with a transition between band to band (B-B) recombination at high temperatures.

PL studies of p-type $GaAs_{1-x}Bi_x$ layers grown by MBE with various doping levels [8] have shown that both p-$GaAs_{1-x}Bi_x$ epilayers (with $p = 1x10^{17}$ cm^{-3}) and undoped $GaAs_{1-x}Bi_x$ demonstrated an S-shaped behaviour in their temperature dependence PL spectra. The PL peaks show redshift, blueshift, and then redshift with increasing temperature. They suggested that the S-shape originates from the localized states that are formed as a result of Bi-induced defects. However, p-$GaAs_{1-x}Bi_x$ layers (with a high $p = 2x10^{18}$ cm^{-3}) showed only a redshift with increasing temperature, indicating an absence of the Bi localized states.

While optoelectronic devices require a controllable methodology for the doping of alloys, there are relatively very few studies addressing the doping process of only (100) $GaAs_{1-x}Bi_x$ [2,6–12]. These investigations have particularly concentrated on the effects the doping has on the structural, electrical and optical properties. Therefore, it is worth noting that the structural and optical properties of n-type and p-type $GaAs_{1-x}Bi_x$ alloys and heterostructures using non-(100) GaAs substrates have not been investigated yet.

In this study, a detailed investigation will be reported on the structural and optical properties of n-type and p-type doped $GaAs_{1-x}Bi_x$ layers grown on high index (311)B oriented GaAs substrates. n-type and p-type GaAs control samples were also grown for comparison purposes. The samples were grown by MBE, and Bi compositions were determined by HR-XRD measurements. Both n-doped and p-doped $GaAs_{1-x}Bi_x$ samples were found to have the same Bi composition, meaning that the substitutional incorporation of Bi does not depend on the type of doping. The optical properties were investigated using PL and micro-Raman spectroscopy. The obtained results, which revealed that the n and p $GaAs_{1-x}Bi_x$ samples have remarkable differences in terms of the density of structural defects and non-radiative centers, indicate that the density of Bi-related defects depend on the type of doping in $GaAs_{1-x}Bi_x$.

8.2 EXPERIMENTAL DETAILS

The samples investigated in this work were grown by MBE under the same conditions as those samples discussed in Chapter 6. The samples consisted of a 100 nm thick doped GaAs buffer layer (n and p = ~2-3 x 10^{18} cm^{-3}) followed by 1 µm thick doped $GaAs_{1-x}Bi_x$ layer (Si-doped n-type = 2 x 10^{16} cm^{-3}; Be-doped p-type = 2 x 10^{16} cm^{-3}, nominal x=6%) grown on (311)B oriented GaAs substrates. The respective control samples do not contain Bi and are just doped GaAs with similar layer structures grown under the same conditions. For simplicity, the samples are labeled as n-GaAs, n-$GaAs_{0.94}Bi_{0.06}$, p-GaAs and p-$GaAs_{0.94}Bi_{0.06}$. Doping of n- or p-type conductivity was carried out during the growth of $GaAs_{1-x}Bi_x$ layers from standard molecular sources, which contained Si and Be dopants at temperatures of 850 ^oC and 652 ^oC, respectively. The Si (n-type dopant) and Be (p-type dopant) sources were calibrated by growing Si-doped and Be-doped GaAs control samples and using Hall measurements to determine the free electron and hole concentrations, respectively.

In addition, SIMS (secondary ion mass spectrometry) depth profiling measurements were carried out on p-i-n samples in order to obtain information about the in-depth distribution of Si and Be elements (see Fig. 8.1).

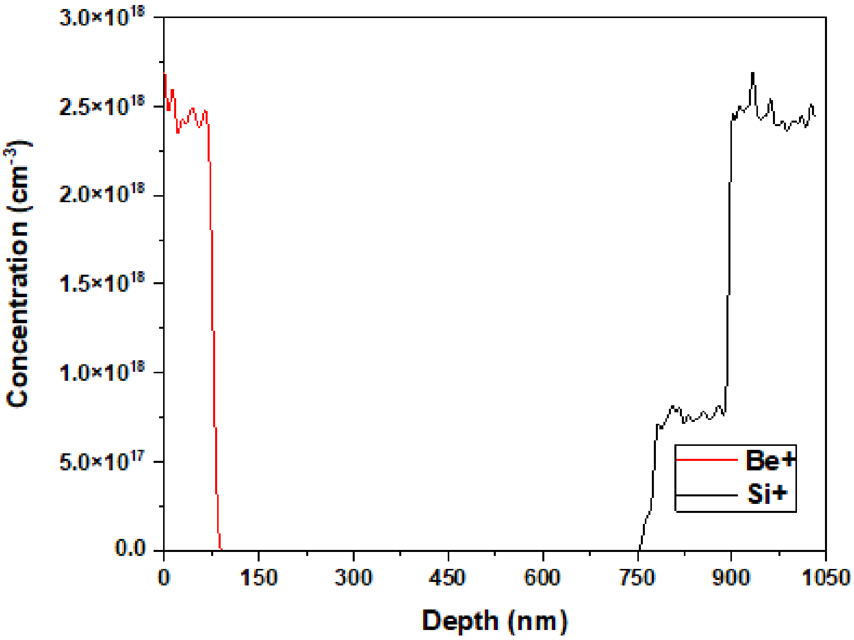

Fig. 8.1: SIMS concentration profile of a GaAs calibration sample (p-i-n structure).

$GaAs_{1-x}Bi_x$ layer was grown at a growth rate of 0.1 nm/s and substrate temperature of ~ 400 °C. Calibration of the substrate temperature at low temperature was carried out using temperature reference points of the arsenic desorption and transition of surface reconstruction on the (100) from (4x4) to (2x3) [13]. In the process of growing the GaAsBi layer, the Ga, Bi and As beam equivalent pressures as measured by an ion gauge were 1.5×10^{-7} Torr, 6.4×10^{-8} Torr, and 1.3×10^{-6} Torr, respectively. It is worth mentioning that when growing a $GaAs_{1-x}Bi_x$ layer on (100) GaAs substrate, a (1x3) or (4x3) reconstruction was observed. XRD measurements of those samples are similar to those presented in Chapter 6.

The optical properties of $GaAs_{1-x}Bi_x$ samples were investigated using PL and micro-Raman techniques as described in Chapter 6. PL measurements were performed as a function of temperature, between 15 and 200 K, and excitation power, ranging from 0.5 mW to 50 mW. Micro-Raman measurements were carried out with laser power in the range from 0.3mW to 30mW.

8.3 RESULTS AND DISCUSSION

8.3.1 HIGH-RESOLUTION X-RAY DIFFRACTION (HR-XRD)

In order to determine the Bi content in the $GaAs_{1-x}Bi_x$ epilayers, the experimental X-ray diffraction curves were simulated and are shown in Fig. 8.2. From the calculated lattice parameters and the Vegard's law, an average concentration of Bi atoms incorporated into the epilayers' lattice was determined. The simulations show that the lattice parameter of $GaAs_{1-x}Bi_x$ is equal to 5.684 Å and the Bi concentrations in both n-type and p-type samples grown on (311)B substrates are 5.4%. The distortion of the lattice of the strained $GaAs_{1-x}Bi_x$ layers was determined by analyzing the asymmetric reflections. The biaxial elastic strains of the lattice cell were estimated assuming a cubic lattice of Bi-containing layer. The value of the lattice parameter of $GaAs_{1-x}Bi_x$ layer was calculated using the Vegard law and lattice parameters of GaAs and GaBi [14]. For the present work it was considered that GaBi has a zinc-blende cubic lattice with a lattice parameter a = 6.178 Å.

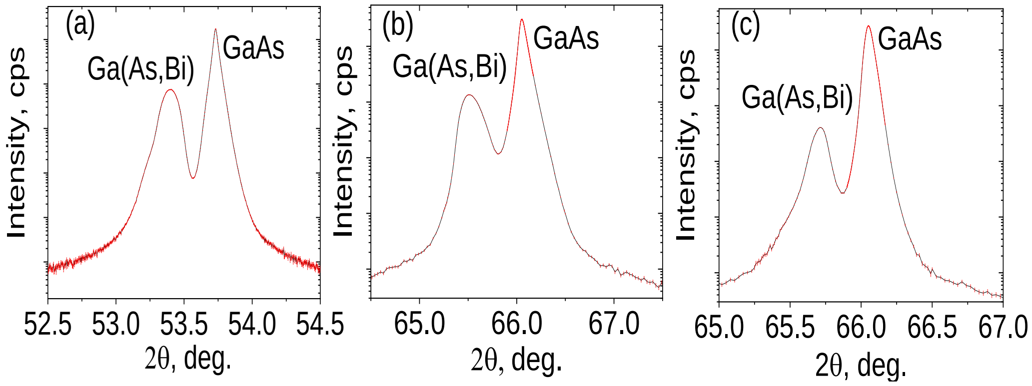

Fig. 8.2: Experimental symmetrical (311) (a) and two asymmetrical (400) (b, c) XRD curves from the p-$GaAs_{0.94}Bi_{0.06}$ sample. The n-$GaAs_{0.94}Bi_{0.06}$ sample demonstrates similar XRD curves, as shown in Fig. 6.2. The asymmetrical XRD curves correspond to small (b) and large (c) incidence angles of the X-rays.

The strain in the vertical (ε_{zz}) and lateral (ε_{xx}) directions are given by equations

$\varepsilon_{zz}= \frac{a_{\perp}-a_{FR}}{a_{FR}}$ and $\varepsilon_{xx}= \frac{a_{\|}-a_{FR}}{a_{FR}}$, respectively, where $a_{\perp}$ is the lattice parameter in vertical direction, $a_{\|}$ - lattice parameter in the lateral direction and a_{FR} – lattice parameter of fully relaxed GaAs lattice.

Using the above equations, ε_{zz} and ε_{xx} of both samples are found to be the same and have values of 0.00035 and -0.018, respectively. One can therefore conclude that there is some residual strain in $GaAs_{1-x}Bi_x$ layers [15]. It is important to point out that due to the large size of the spot of X-rays impinging on the samples, the data shown here represent only averaged values of strain. Particular features of the layer's strains need detailed analysis which is out of the scope of this thesis. For the reference doped GaAs samples no biaxial strain was found indicating that there is no second lattice parameter.

8.3.2 RAMAN SPECTROSCOPY

Fig. 8.3 shows typical room temperature Raman spectra for 3mW laser power of p-GaAs, n-GaAs, p-$GaAs_{0.94}Bi_{0.06}$ and n-$GaAs_{0.94}Bi_{0.06}$ samples. Two Raman peaks were observed at around 289 cm^{-1} and 266 cm^{-1} for all samples. These peaks are associated with the well-established longitudinal and transversal-optics phonons at the center of the Brillouin zone, LO(Γ) and TO(Γ), respectively. The Raman spectrum of crystalline zinc blende structure of GaAs tetrahedral (*Td symmetry*) present only two first order peaks around 292 cm^{-1} LO(Γ) and 267 cm^{-1} TO(Γ) [16–19]. It is noticed that these modes show a clear redshift, which is associated with sample growth conditions, carriers-plasmons-phonons coupling, and an increase of compressive strain with increased Bi content.

The existence of compressive strain in these samples is in agreement with the HR-XRD results. For backscattering Raman configuration of (311)B face, both Raman LO(Γ) and TO(Γ) modes are allowed by selection rules.

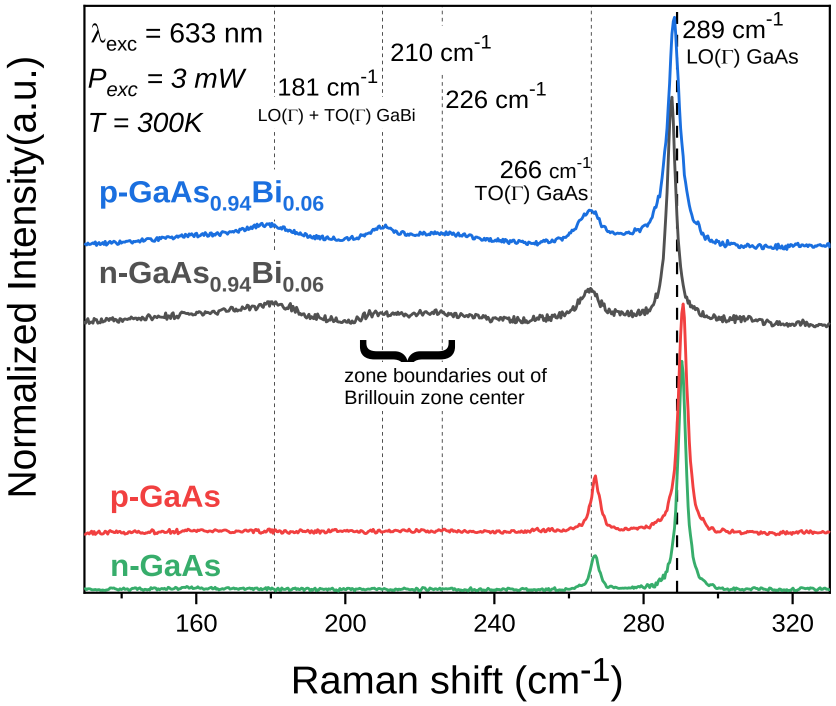

Fig. 8.3: Room temperature Raman spectra of n-GaAs, p-GaAs, and n-$GaAs_{0.94}Bi_{0.06}$, and p- $GaAs_{0.94}Bi_{0.06}$ (311)B samples obtained with a laser excitation and power of 633nm and 3 mW, respectively.

The observed Bi related Raman peaks, around 181, 210, and 226 cm^{-1}, were previously reported in the literature [15,20–30]. However, the interpretation of these peaks is controversial [21,22,26,29,30]. Usually, the 181 cm^{-1} and 210 cm^{-1} Raman peaks are associated with the GaBi TO(Γ) mode and GaBi LO(Γ) mode, respectively. On the other hand, the Raman mode around 226 cm^{-1} could be due to other zone boundaries such as longitudinal-acoustics phonons: LA(X) and LA(L), which are not allowed due to momentum conservation. These Raman modes can be induced by the increase of disorder due to Bi incorporation in $GaAs_{1-x}Bi_x$ samples. Other possible interpretations for these observed peaks were also reported in the literature. For example, the peak at around 181 cm^{-1} could not only be a TO(Γ) mode but it could be associated with the convoluted LO(Γ) + TO(Γ) GaBi vibrational mode [30,31]. However, it is well established that the 181 cm^{-1} peak is related to the GaBi Raman mode. In the following, the discussion will focus on the two different ranges of the Raman spectra where different modes were observed, namely, range **I:** TO(Γ) and LO(Γ) GaAs modes (240 cm^{-1} to 310 cm^{-1}) and range **II:** Bi induced Raman modes (140 cm^{-1} à 240 cm^{-1}).

Fig. 8.4 shows the Raman spectra for all samples in the range 140-240 cm^{-1}. It is worth pointing out that no Raman peak was detected in this range for n-GaAs and p-GaAs samples. On the other hand, the n-$GaAs_{0.94}Bi_{0.06}$ and p-$GaAs_{0.94}Bi_{0.06}$ samples show clearly Raman peaks. These Bi induced peaks are associated with GaBi Raman modes and Bi-disorder-induced breakdown selection rules in the crystal structure. The observation of Bi-induced peaks confirms that the Bi atom is incorporated in the GaAs (311)B host lattice resulting in $GaAs_{1-x}Bi_x$ crystal.

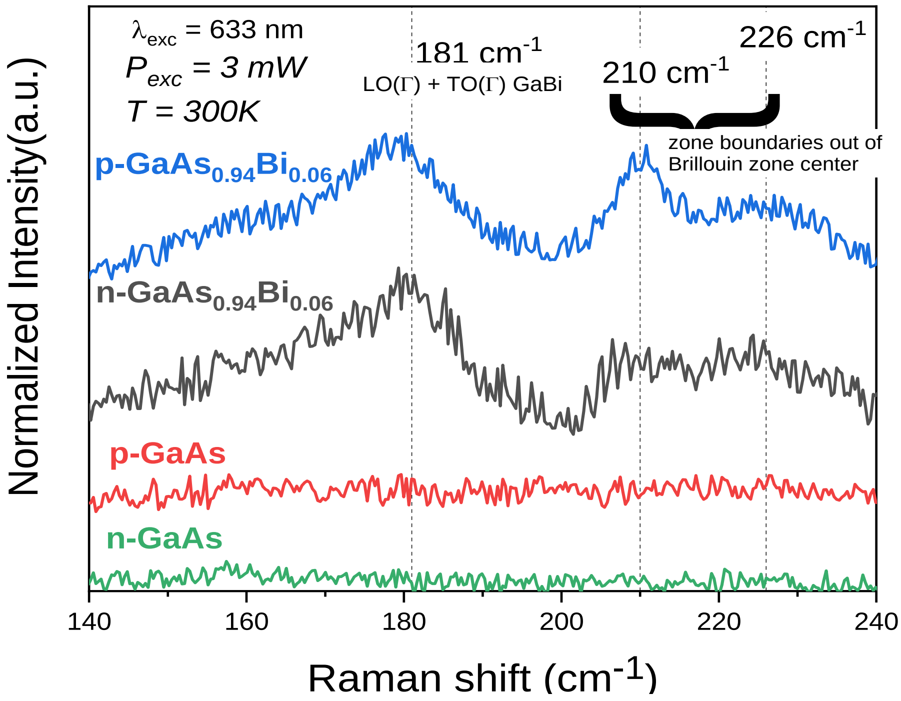

Fig. 8.4: Raman spectra of n-GaAs, p-GaAs, n- $GaAs_{0.94}Bi_{0.06}$, and p- $GaAs_{0.94}Bi_{0.06}$ (311)B samples in the range of Bi-related Raman modes (**range I**). The laser excitation and power were 633nm and 3mW, respectively.

For doped samples, it is necessary to consider the contribution of the longitudinal optical phonon-plasmon-coupled (LOPC) Raman modes, which usually change the shape of the spectrum in the LO(Γ) and TO(Γ) region [32–38]. Actually, in doped samples the carriers plasmons couple with LO phonon and result in L^+ and L^- Raman peaks, which depend on effective mass, mobility, and carrier concentration. Usually, the L^- peak is broader and has a frequency lower than TO(Γ) Raman mode. As the carrier concentration increases, the L^- peak becomes sharper and closer to the TO(Γ) Raman frequency. On the other hand, the L^+ peak is usually sharp and close to the LO(Γ) Raman frequency, presents a blueshift, and a broadening with increasing carrier concentration. For samples with low mobility, usually only one LOPC Raman mode is observed, between LO(Γ) and TO(Γ) frequencies, due to the strong plasmon damping.

For low carrier concentration, LOCP is close to LO(Γ) Raman frequency. If the carrier concentration is increased, the LOPC has an initial blueshift, followed by a redshift up to the TO(Γ) Raman frequency, with increase broadening. Usually, for GaAs, except for the L^+ for $n > 10^{18}$ cm^{-3}, the LOPC Raman peaks are not well resolved in the range of LO(Γ) and TO(Γ). The LO(Γ) and TO(Γ) Raman peaks are due to regions with reduced density of carriers (depletion regions) where there is no effect of phonon-plasmon coupling.

The effect of laser power on LOPC modes was also studied. However, it is not the purpose of this work to investigate the effect of photon-generated carriers. The main aim was to determine the limit of laser power that does not introduce important changes due to the photo-generated carriers. Depending on the laser power, the Raman spectra can have a significant contribution from photo-generated carriers [39–45], which can modify the LOPC modes due to intrinsic doping. Fig. 8.5 shows typical Raman spectra of p-GaAs$_{0.94}$Bi$_{0.06}$, n-GaAs, p-GaAs and n-GaAs$_{0.94}$Bi$_{0.06}$ samples for different laser powers. Marked changes were observed for laser power in the range of 3 mW to 30 mW.

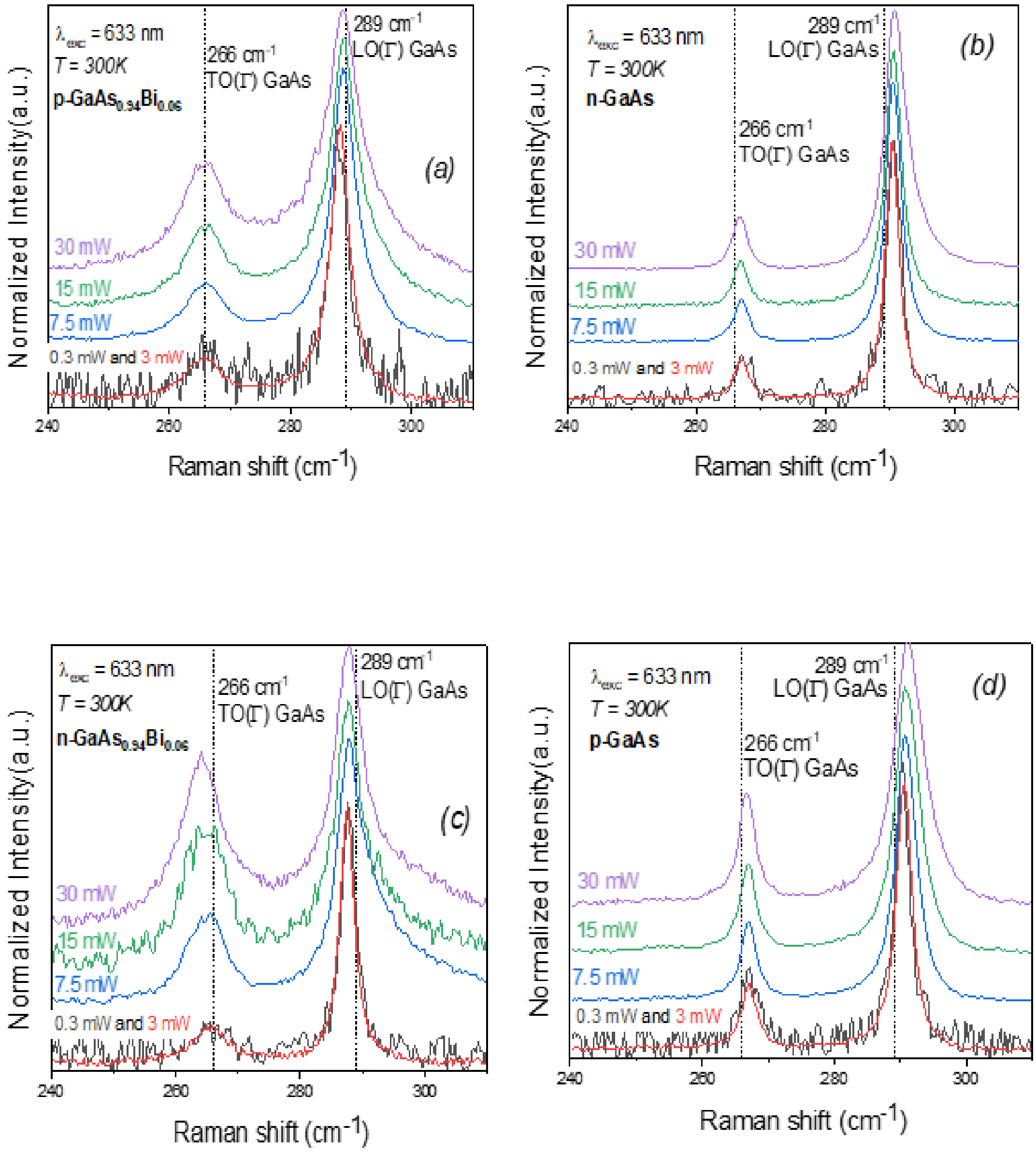

Fig. 8.5: Laser power dependence of Raman spectra for (a) p-GaAs$_{0.94}$Bi$_{0.06}$, (b) n-GaAs, (c) n-GaAs$_{0.94}$Bi$_{0.06}$ and (d) p-GaAs samples using a laser excitation of 633nm.

On the other hand, there is no significant change in Raman spectra for 0.3 mW and 3 mW powers. The fitting of the spectra with two Lorentz functions shows that the variations of parameters in this laser power range are less than 8%. However, it is remarked that the LOCP modes induced by photon-generated carriers are dependent on the type of intrinsic doping and it is different for n-GaAs, p-GaAs, n-GaAs$_{0.94}$Bi$_{0.06}$, and p-GaAs$_{0.94}$Bi$_{0.06}$ samples. One can conclude that the contribution of photon-generated carriers can be disregarded for laser power less than 3 mW. Therefore, a 3 mW of laser power was used for the Raman measurements.

Fig. 8.6 shows the Raman spectra for all samples in the range 240 to 310 cm^{-1} (range II). Two sharp Raman peaks related to TO(Γ) and LO(Γ) GaAs Raman modes for GaAs samples were observed. No evident effect of doping was noticed, probably due to the low doping concentration of these samples: 2 x 10^{16} cm$^{-3,}$ for n and p-doping. Notably, the peak L^{+} was not observed in the range 290 to 1500 cm^{-1} (not shown here), which is usually expected for n-type samples. The Raman spectrum is well fitted with two Lorentz functions. There is no clear contribution of LOCP modes in the range 260 to 300 cm^{-1} (fitting parameters shown in Table 8.1). In addition, the obtained full width at half maximum (FWHM) of about 3 cm^{-1} which is a typical value obtained for GaAs bulk crystals also shows that there is no evidence of an important contribution of LOCP modes. For the p-GaAs sample, a small effect in the width of LO(Γ) Raman mode was observed, probably related to the small increased crystal disorder.

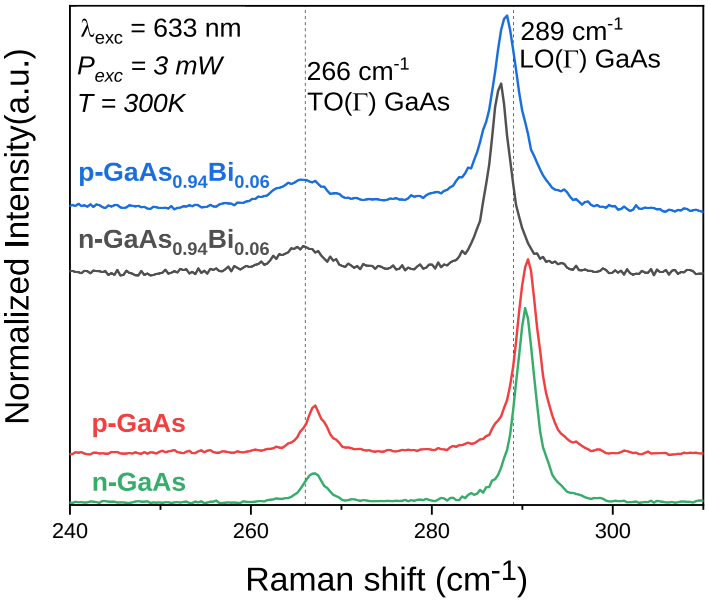

Fig. 8.6: Raman spectra of n-GaAs, p-GaAs, n-$GaAs_{0.94}Bi_{0.06}$, and p-$GaAs_{0.94}Bi_{0.06}$ (311)B samples for laser excitation and power of 633nm and 3mW, respectively, in the range of GaAs Raman modes (**range II**).

Furthermore, for the n-$GaAs_{0.94}Bi_{0.06}$ samples, the L^+ Raman mode was not observed. There is no evidence of a third peak in the range of 260 to 300 cm^{-1}, like for the p-$GaAs_{0.94}Bi_{0.06}$ samples. These spectra can also be fitted by two Lorentz functions centered at 265.4 and 265.6 cm^{-1} next to the TO peak (266 cm^{-1} TO(Γ) GaAs), and 287.5 and 288.2 next to LO peak (292 cm^{-1} LO(Γ) GaAs) (see Table 8.1). It was also observed a clear redshift and a broadening for Raman modes of n-$GaAs_{0.94}Bi_{0.06}$ and p-$GaAs_{0.94}Bi_{0.06}$ samples as compared to n-GaAs and p-GaAs. The redshift due to bismuth is different for LO(Γ) modes (for n-type $\Delta\omega = 3.0$ cm^{-1} and for p-type $\Delta\omega = 2.3$ cm^{-1}) and TO(Γ) modes (for n-type $\Delta\omega = 1.6$ cm^{-1} and for p-type $\Delta\omega = 1.4$ cm^{-1}). This redshift, which is usually associated with strain and Bi incorporation, is given by $\Delta\omega_{\mathrm{Lo\ or\ To}} = \Delta\omega_{alloy} + \Delta\omega_{strain}$[20,46]. Similar behavior was reported previously in the literature for undoped (100) and (311)B

$GaAs_{1-x}Bi_x$ samples [15,20,23,25,28,29,46]. Taking LO(Γ) of bulk GaAs crystal at 292 cm^{-1} as reference, the experimental value obtained for the ratio Δω/xBi for LO(Γ) GaAs mode, -86.5 cm^{-1} (n-type) and -70.4 cm^{-1} (p-type), and TO(Γ) GaAs mode, -26.6 cm^{-1} (n-type) and -25.9 cm^{-1} (p-type), are consistent with values obtained in literature, i.e., -68 cm^{-1} to -120 cm^{-1} and -20 cm^{-1} to -30 cm^{-1}, respectively [16,20,24,26,30].

It is well known that the crystal structure is affected by the incorporation of Bi atom, which substitutes an As atom and, therefore, introduces strain and crystal disorder [15,20,23,25,26,28–30,46]. The increase of disorder could explain the observed broadening of the LO(Γ) GaAs mode, in the p-$GaAs_{0.94}Bi_{0.06}$ sample, and TO(Γ) GaAs Raman modes. On the other hand, the incorporation of Bi atom could also contribute to intrinsic p-doping, which increases with increasing Bi concentration with doping in the range p = 10^{17} to 10^{18} cm^{-3} and could possibly play a part in the broadening of the peaks. The observation of similar linewidth of LO(Γ) peaks for n-$GaAs_{0.94}Bi_{0.06}$ as compared to n-GaAs or p-GaAs, indicates a compensation effect of n-doping with the intrinsic p-doping due to Bi incorporation in GaAs [26].

Table 8.1. Raman parameters for n-GaAs and p-GaAs reference samples, and n-$GaAs_{0.94}Bi_{0.06}$ and p-$GaAs_{0.94}Bi_{0.06}$ samples.

Samples	n-GaAs		n-$GaAs_{0.94}Bi_{0.06}$		p-GaAs		p-$GaAs_{0.94}Bi_{0.06}$	
Mode	LO	TO	LO	TO	LO	TO	LO	TO
ω_{peak} (cm^{-1})	290.4	267.0	287.5	265.4	290.6	267.1	288.2	265.6
FWHM	2.7	3.0	2.8	7.0	3.0	3.0	3.8	8.3
I_{peak}	1	0.15	1	0.15	1	0.25	1	0.16

The LOCP for undoped $GaAs_{1-x}Bi_x$ samples is due to hole plasmons, which usually contribute to the changes observed in the Raman spectra, particularly for $x > 1\%$ [20,24,29,30]. However, the observed differences between n-$GaAs_{0.94}Bi_{0.06}$ and p-$GaAs_{0.94}Bi_{0.06}$ samples are not related to Bi concentrations which are 5.4% for both samples, or to the effect of strain, also the same for the two samples, as the XRD results indicate. The broadening and little blueshift of LO peak observed in the p-$GaAs_{0.94}Bi_{0.06}$ samples as compared to n-$GaAs_{0.94}Bi_{0.06}$ samples could be associated with the convoluted LOCP and LO(Γ) Raman peaks. Other effects, such as increasing in disorder and defects density could also contribute to these differences of Raman spectra for these samples. These effects could also manifest themselves in the PL spectra as will be discussed below.

8.3.3 PHOTOLUMINESCENCE

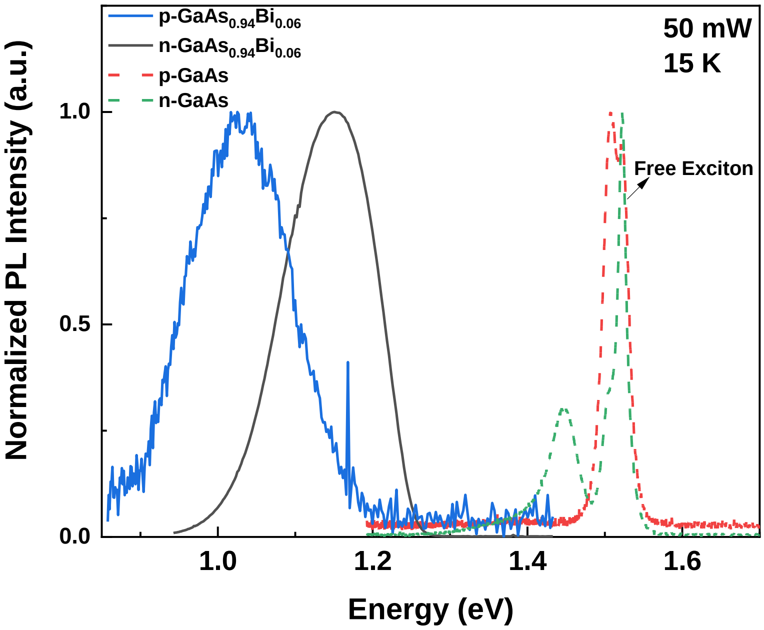

Fig. 8.7: Typical normalized PL spectra for n-$GaAs_{0.94}Bi_{0.06}$, p-$GaAs_{0.94}Bi_{0.06}$, n-GaAs, and p-GaAs samples at 15K.

Fig. 8.7 shows low-temperature (15 K) PL spectra for doped $GaAs_{0.94}Bi_{0.06}$ and GaAs samples. The PL peaks observed in doped GaAs samples at around 1.52 eV and between 1.3 to 1.5 eV are associated with free exciton recombination (FE) (peaks with high intensity and sharp profile), and impurities (n or p dopant) recombination, respectively. The PL peaks of $GaAs_{0.94}Bi_{0.06}$ samples show a strong redshift as compared to GaAs samples, as expected due to Bi incorporation and consequent reduction of the band-gap energy and formation of localized states [1,47–50]. It was observed that the redshift of the PL emission increases from n-$GaAs_{0.94}Bi_{0.06}$ (1.152 eV) to p-$GaAs_{0.94}Bi_{0.06}$ (1.027 eV) samples, which could indicate a higher Bi incorporation for p-doped samples. If one assumes that the substitutional Bi causes a band-gap reduction of 84 meV per % of Bi and compare with the free excitonic (FE) band-gap of GaAs, one could estimate the amount of effective substitutional Bi incorporated in each $GaAs_{1-x}Bi_x$ sample (x = 5.8% for p-doped and x = 4.4% for n-doped). On the other hand, both $GaAs_{0.94}Bi_{0.06}$ samples present the same estimated value of Bi content (x = 5.4%) and similar residual strain values as estimated by HR-XRD data. However, as mentioned above the PL emissions at low temperatures are observed in an energy range distinct of the expected band-gap reduction. Therefore, other contributions such as strain or Bi-defect level- band related transition could also contribute to explain the observed differences in PL peak position for n- and p-doped GaAsBi samples.

As discussed previously, the giant reduction in the band-gap energy of $GaAs_{1-x}Bi_x$ alloys has been described using a valence band (VB) anti-crossing interaction between the Bi level and the host GaAs VB. Additionally, the low-temperature PL peak is also expected to present an energy shift for samples under different strain conditions (compressive versus tensile), due to changes in the structure of the band.

In samples with compressive strain usually the PL peak is redshifted with respect to the expected free exciton [50,51] and, therefore, this effect should happen with similar magnitude in both $GaAs_{0.94}Bi_{0.06}$ samples as pointed by HR-XRD strain estimation. On the other hand, the presence of Bi-related localized states close to the VB edge also cause a redshift in the PL peak since the exciton localized recombination changes the PL line shapes to exhibit an asymmetric characteristic with a low energy tail, which usually dominates the excitonic recombination processes at low temperatures. The origin of these localized states is attributed to the formation of Bi-related complexes and to alloy disorder in Ga(As, Bi).

As pointed out previously, there are few studies on optical and electrical properties of n- and p-doped $GaAs_{1-x}Bi_x$ alloys [2,6,7,9–12,52]. Particularly, it was shown that the incorporation of Bi suppresses the formation of GaAs-like electron traps, thus reducing the total trap concentration in dilute $GaAs_{1-x}Bi_x$ layers as compared to GaAs grown under the same growth conditions [6]. However, the Bi incorporation can also introduce Bi-related defects which can be acceptor and donor levels [6]. For n-doped $GaAs_{1-x}Bi_x$ samples it was previously shown that the Bi-induced levels are mainly electron traps [6] while for p–doped samples they are mainly hole traps [7]. These Bi-induced traps can affect considerably the optical properties of $GaAs_{1-x}Bi_x$ layers [6]. In addition, the presence of different Bi induced traps for n- or p-doped samples can affect differently the optical properties of n- and p-doped GaAsBi layers with the same Bi-concentration. For n-doped $GaAs_{0.94}Bi_{0.06}$ layers it was previously shown that both band to band (B-B) and donor to valence band (D-B) optical recombinations can contribute to the PL spectrum (see Fig.8.8) [6]. The D-B emission was attributed to the recombination of carriers from Bi-induced donor traps and VB [6]. The contribution of this D-B transition explains the observed lower red-shift of the PL peak energy observed in these n-doped $GaAs_{0.94}Bi_{0.06}$ samples as compared to the standard band-gap reduction (i.e., 84 meV per % of Bi). Actually, it is well known that the energy position of Bi-induced donor trap level does change with the Bi incorporation while the Bi-related shift of the VB is typically 51 meV/%Bi [6]. As both emissions are not well resolved at low temperature, the total PL peak energy has a smaller red shift than the expected band-gap reduction for 5.4% Bi. A similar contribution of the D-B emission in the PL spectra was previously observed for GaAsN layers [53].

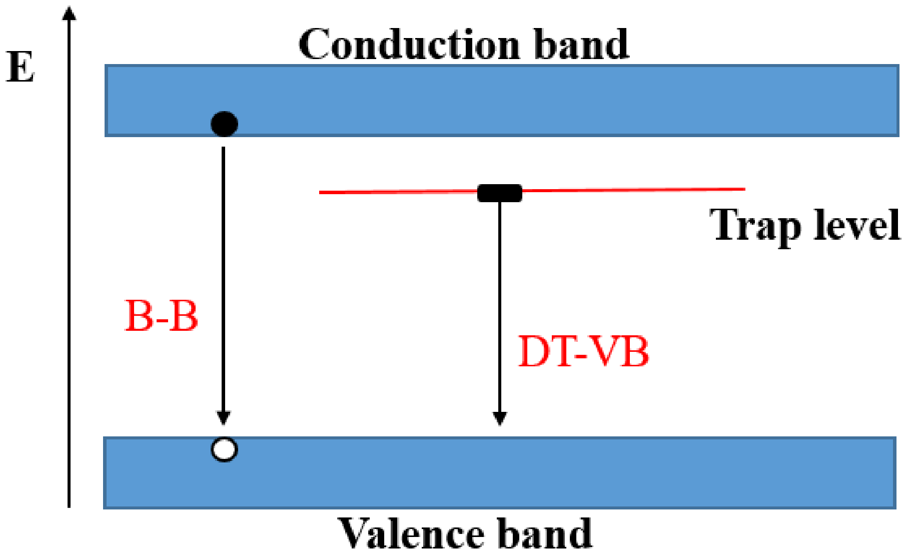

Fig. 8.8: Diagram of Bi-induced changes in the conduction (CB) and valence bands (VB) and energy position of Donor Trap (DT). The optical transitions observed in the PL spectra (DT-VB and Band-Band (B-B) transition) are also shown.

On the other hand, for p-doped samples it was previously shown that the energy red-shift of the PL peak as compared to p-GaAs samples could be associated with the following optical transition: (1) conduction band (CB) to Bi-induced states and (2) CB to shallow Be acceptor states (B–A) [8]. These contributions explain the temperature and laser power dependence of the results presented here.

In addition, it important to note that the PL spectrum of the p-GaAs$_{0.94}$Bi$_{0.06}$ samples has much smaller optical efficiency (lower PL intensity and higher signal-to-noise ratio) as compared to the n-GaAs$_{0.94}$Bi$_{0.06}$ samples. This behavior is also consistent with the observed broadening of the LO Raman peak sample. This indicates that higher density of non-radiative centers is present in p-GaAs$_{0.94}$Bi$_{0.06}$ as compared to n-GaAs$_{0.94}$Bi$_{0.06}$ samples. The non-radiative centers do not contribute to effectively change the band-gap energy in the electronic structure of the host lattice [54–56] but affects the optical efficiency.

In general, the obtained results indicate that the density of non–radiative Bi related defects are higher for the p-doped GaAs$_{1-x}$Bi$_x$ than for the n-doped GaAs$_{1-x}$Bi$_x$. Particularly, the contribution of different Bi-related traps in n- and p-type samples seems to have important role on optical properties of these (311)B oriented alloys.

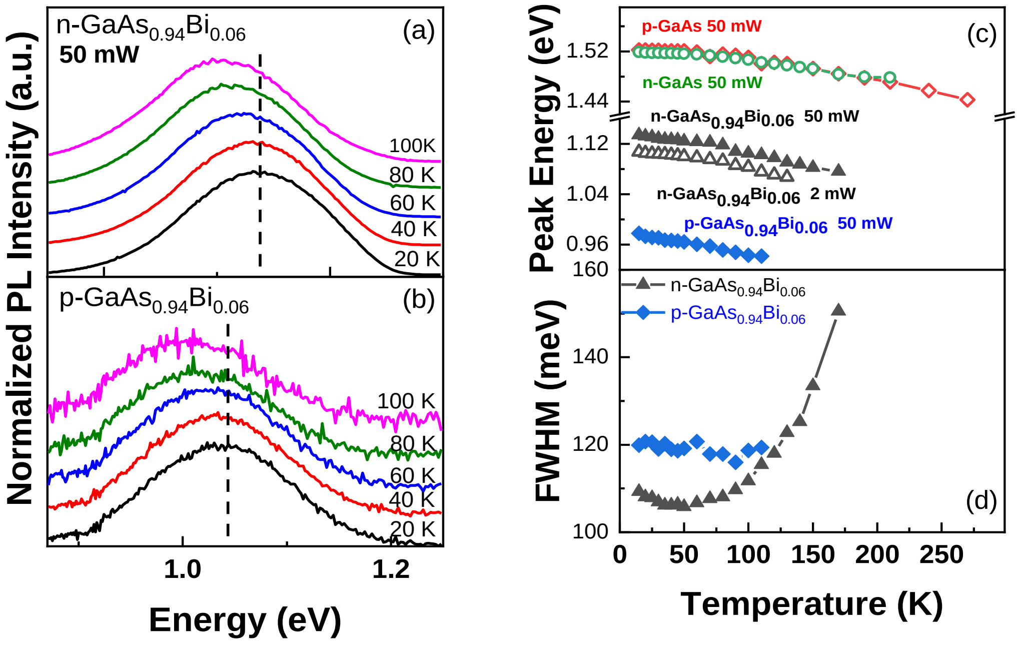

Fig. 8.9: Typical normalized PL spectra as a function of temperature for (a) n-type and (b) p-type under 50mW laser excitation power. (c) PL energy peak and (d) PL FWHM temperature dependences.

Fig. 8.9 (a, b) presents the temperature dependence of the PL spectra of doped $GaAs_{1-x}Bi_x$ samples. The PL energy peaks exhibit a monotonic redshift with increasing temperature due to the decrease of the band-gap energy, and follow the Varshni empirical dependence formalism [54,57,58]. The latter observation indicates the apparent absence of the Bi localization effect which manifests itself as an S-shape profile typically observed in N and Bi diluted III-V alloys. The temperature dependence of the PL peak position and FWHM does not evidence an S-shape profile, which is usually observed for $GaAs_{1-x}Bi_x$ samples [59–61]. This S-shape behavior could probably occur in these investigated samples at higher temperatures. However, the PL signal of these samples is only detected in the range of 15- 100K, which is probably not enough to observe the S-shape behavior. On the other hand, the laser excitation power of 50 mW could also be high enough to observe the S-shape, since at this condition, the exciton localization regime can be lost already and the radiative recombination are dominated by the free exciton regime. In order to avoid a misinterpretation due to the saturation effect of the localized states at high power excitation, PL measurements using lower laser power excitation (2mW) were performed for n-type samples (Fig. 8.9 (c)). As clearly seen in Fig. 8.9 (c) the temperature dependence of the PL peak shows the same trend for both laser excitation powers of 2mW and 50mW. On the other hand, the p-$GaAs_{0.94}Bi_{0.06}$ samples have no significant PL intensity at low laser power excitation of 2mW (not shown here). In addition, the PL signal is observed only at higher laser excitation powers because its optical efficiency is lower than that of the n-$GaAs_{0.94}Bi_{0.06}$ samples.

Moreover, the important PL quenching observed for the p-doped sample with increasing temperature could be due to a higher density of non-radiative Bi complexes and native defects related to GaAs host lattice. A similar effect has been observed in nitrogen diluted III-V alloys [62].

As reported previously in the literature for p-doped (100) $GaAs_{1-x}Bi_x$ samples [8], this monotonic PL energy dependence as a function of temperature indicates a downward shift of the Fermi level induced by p-type doping that modifies carrier occupation at the localized states. As previously discussed, the incorporation of Bi atom could also contribute to intrinsic p-doping, which increases the overall doping with increasing Bi concentration [6]. Bi complexes or clusters involving two or more Bi atoms have been experimentally evidenced as the most likely candidates to form such acceptor levels [12,63] and can contribute to the B-A recombination.

In order to further investigate the temperature dependence of PL intensity and activation energies of carriers involved in the radiative recombination, the PL data was first fitted using a simple Arrhenius equation as described in Chapter 6, section (6.3.3.2). However, the fitting was not satisfactory as two distinct exponential trends were observed, indicating two activation energies, which describe the thermal activation of carriers in two temperature regimes. Therefore, an additional energy term was included in the Arrhenius equation [60,63,64] and was found to fit the data better. Fig. 8.10 shows a plot of integrated PL intensity (IPL) versus 1/ k_BT.

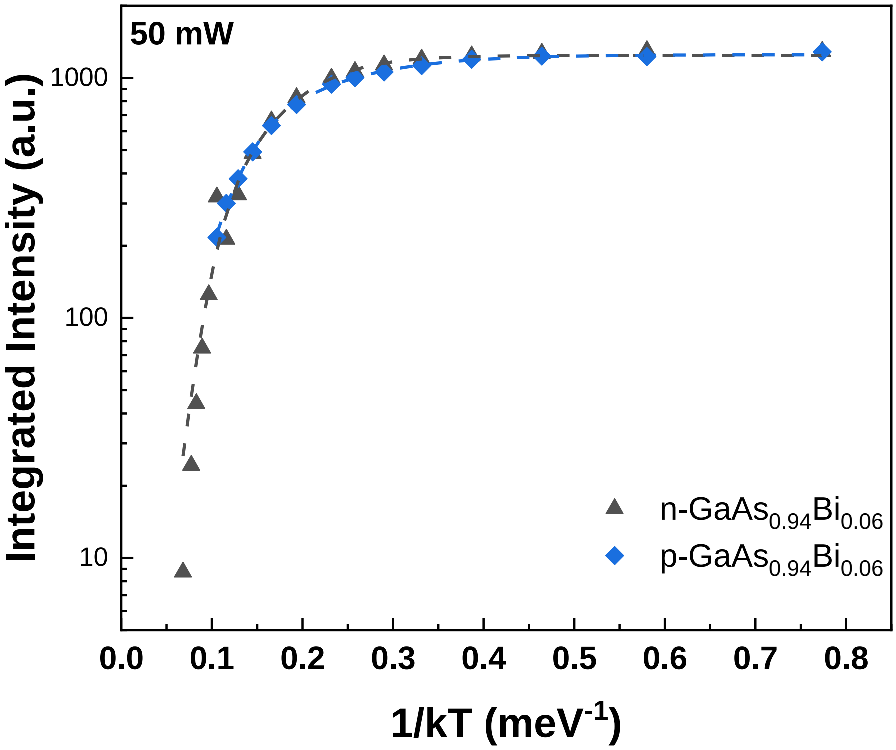

Fig. 8.10: Arrhenius plot of PL intensity for p-GaAs$_{0.94}$Bi$_{0.06}$ and n-GaAs$_{0.94}$Bi$_{0.06}$ samples. Dashed lines illustrate the fitted lines using Arrhenius equation.

As discussed previously, GaAs$_{1-x}$Bi$_x$ alloys tend to form localized pairs and clusters, which have different configurations and binding energies [47,51,55,65], alloy disorder, and potential fluctuation. These states are usually associated with two groups with different activation energies in undoped GaAs$_{1-x}$Bi$_x$ samples: one ranges from 8–17 meV and is related to Bi clusters and Bi pairs [47,61,66,67], and the other energy around 50 meV is related to alloy disorder [59,67–69]. For samples shown in Fig. 8.10 (a), E$_1$ energies ranging between 11 meV and 20 meV are attributed to Bi clusters and Bi pairs, while E$_2$ values ranging from 41 to 73 meV are associated with alloy disorder (around 50 meV). While Bi clusters and alloy disorder are present in both n- and p- doped GaAsBi samples, the fitting results

(Table 8.2) indicate higher contribution of E_1 centers for p-$GaAs_{0.94}Bi_{0.06}$ (A_1>>A_2) and higher contribution of E_2 centers for n-$GaAs_{0.94}Bi_{0.06}$ (A_1<<A_2). These results indicate that the density of Bi related defects is higher for p-doped $GaAs_{1-x}Bi_x$ than for n-doped $GaAs_{1-x}Bi_x$.

Table 8.2: Arrhenius fitting parameters for n-$GaAs_{0.94}Bi_{0.06}$ and p-$GaAs_{0.94}Bi_{0.06}$ samples.

Samples	Activation Energy (meV)		Parameter A	
n-$GaAs_{0.94}Bi_{0.06}$	E_1	19.89±3.02	A_1	3.30±1.02
	E_2	73.85±3.12	A_2	39.92±12.01
p-$GaAs_{0.94}Bi_{0.06}$	E_1	11.74±6.05	A_1	243.8±16.02
	E_2	41.32±1.07	A_2	5.03±2.01

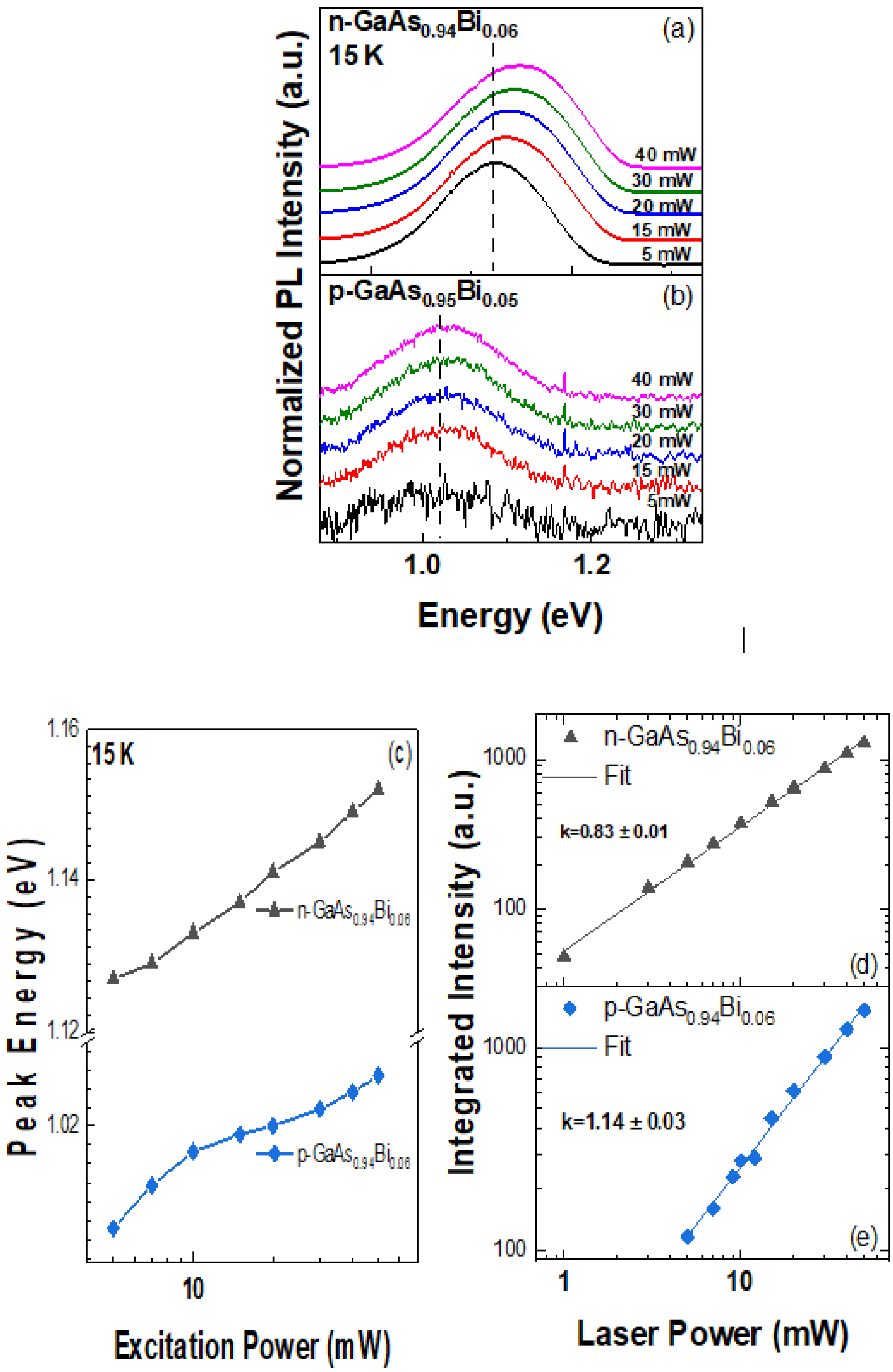

Fig. 8.11: (a, b) PL spectra for different laser power. (c) Peak energy as a function of P_{EXC}. (d, e) Integrated PL intensity (I_{PL}) at 15 K as function of Pexc for p-$GaAs_{0.94}Bi_{0.06}$ and n-$GaAs_{0.94}Bi_{0.06}$ samples. The dashed lines illustrate the fitting using equation: $I_{PL} = \beta(P_{EXC})^k$.

Fig. 8.11 shows the PL spectra, PL peak energy and PL intensity as a function of P_{EXC} for both doped samples. As the excitation power increases the PL peak blueshifts as shown in Fig. 8.11 (c), which evidences the filing of localized states. The lowest PL peak energy observed at 5 mW excitation is attributed to localized exciton recombination (LE), while the highest energy emission observed at 40 mW excitation is assigned to free exciton (FE). On the other hand, it is expected that PL peak energy for the impurity related recombination remains constant irrespective of the laser excitation intensity. It was observed that the PL spectra of n- and p-doped $GaAs_{0.94}Bi_{0.06}$ samples are relatively less sensitive to laser power excitation, i.e. show a relatively small appreciable energy shift as a function of excitation power. This effect is particularly more important in p-doped GaAsBi samples. These results can be attributed to the contribution of different recombination mechanisms for both samples, as reported previously [6,8].

The integrated PL intensity (I_{PL}) as a function of laser excitation power (P_{EXC}) is shown in Fig. 8.11 (d)–(e) and their respective fitting curves using the power-law $I_{PL} = \beta(P_{EXC})^k$ [70], where β and k are fitting parameters. The exponent k=1 for excitonic recombination (whether radiative or non-radiative recombination dominates) and k=2 for free carrier recombination, assuming that non-radiative recombination dominates. The value of k is approximately unity at 15 K for both samples, which indicates the dominance of excitonic recombination. However, $k > 1$ for p-doped samples, indicating that free excitons and free carriers (as B-A recombination) contribute to the recombination, and it is limited by non-radiative centers, while $k < 1$ for n-doped samples indicate that the emission is governed by localized excitons.

8.4 CONCLUSION

Structural and optical properties of n- and p-doped $GaAs_{1-x}Bi_x$ thin films grown by molecular beam epitaxy on (311)B GaAs substrates reveal the same effective amount of Bi incorporation and strain in both types of doped $GaAs_{1-x}Bi_x$ samples. However, the samples present remarkable differences in terms of density of Bi-related defects. Particularly, these defects have important contribution in the presence of non-radiative centers and also contribute to different radiative recombination such as acceptor (donor) to band transition. The results also indicate that the density of Bi related defects depend on the type of doping (n-or p-doping) of $GaAs_{1-x}Bi_x$ and have different effects on the PL properties of n- and p-doped GaBiAs layers grown on (311)B substrate orientation.

REFERENCES

[1] K. Alberi, O.D. Dubon, W. Walukiewicz, K.M. Yu, K. Bertulis, A. Krotkus, *Valence band anticrossing in GaBi xAs 1-x*, Appl. Phys. Lett. **91**, 051909 (2007).

[2] R.N. Kini, L. Bhusal, A.J. Ptak, R. France, A. Mascarenhas, *Electron Hall mobility in GaAsBi*, J. Appl. Phys. **106**, 04370 (2009).

[3] R.N. Kini, A.J. Ptak, B. Fluegel, R. France, R.C. Reedy, A. Mascarenhas, *Effect of Bi alloying on the hole transport in the dilute bismide alloy GaAs1-xBix*, Phys. Rev. B - Condens. Matter Mater. Phys. **83**, 1 (2011).

[4] D.G. Cooke, F.A. Hegmann, E.C. Young, T. Tiedje, *Electron mobility in dilute GaAs bismide and nitride alloys measured by time-resolved terahertz spectroscopy*, Appl. Phys. Lett. **89**, 122103 (2006).

[5] D.A. Beaton, R.B. Lewis, M. Masnadi-Shirazi, T. Tiedje, *Temperature dependence of hole mobility in GaAs1-xBix alloys*, J. Appl. Phys. **108**, 083708 (2010).

[6] Ł. Gelczuk, J. Kopaczek, T.B.O. Rockett, R.D. Richards, R. Kudrawiec, *Deep-level defects in n-type GaAsBi alloys grown by molecular beam epitaxy at low temperature and their influence on optical properties*, Sci. Rep. **7**, 12824 (2017).

[7] P.M. Mooney, M.C. Tarun, V. Bahrami-Yekta, T. Tiedje, R.B. Lewis, M. Masnadi-Shirazi, *Defect energy levels in p-type GaAsBi and GaAs grown by MBE at low temperatures*, Semicond. Sci. Technol. **31**, 065007 (2016).

[8] M. Yoshimoto, M. Itoh, Y. Tominaga, K. Oe, *Quantitative estimation of*

density of Bi-induced localized states in GaAs1−xBix grown by molecular beam epitaxy, J. Cryst. Growth. **378**, 73 (2013).

[9] P.M. Mooney, K.P. Watkins, Z. Jiang, A.F. Basile, R.B. Lewis, V. Bahrami-Yekta, M. Masnadi-Shirazi, D.A. Beaton, T. Tiedje, *Deep level defects in n-type GaAsBi and GaAs grown at low temperatures*, J. Appl. Phys. **113**, 13370 (2013).

[10] R.L. Field, J. Occena, T. Jen, D. Del Gaudio, B. Yarlagadda, C. Kurdak, R.S. Goldman, *Influence of surface reconstruction on dopant incorporation and transport properties of GaAs(Bi) alloys*, Appl. Phys. Lett. **109**, 252105 (2016).

[11] M.A. Stevens, S. Lenney, J. McElearney, K.A. Grossklaus, T.E. Vandervelde, *Characterization of tellurium and silicon as n-type dopants for GaAsBi*, Semicond. Sci. Technol. **35**, 105006 (2020).

[12] R.N. Kini, A.J. Ptak, B. Fluegel, R. France, R.C. Reedy, A. Mascarenhas, *Effect of Bi alloying on the hole transport in the dilute bismide alloy GaAs1-xBix*, Phys. Rev. B - Condens. Matter Mater. Phys. **83**, 1 (2011).

[13] V. V. Preobrazhenskii, M.A. Putyato, B.R. Semyagin, *Measurements of parameters of the low-temperature molecular-beam epitaxy of GaAs*, Semiconductors. **36**, 837 (2002).

[14] M. Ferhat, A. Zaoui, *Structural and electronic properties of III-V bismuth compounds*, Phys. Rev. B. **73**, 115107 (2006).

[15] E. Tisbi, E. Placidi, R. Magri, P. Prosposito, R. Francini, A. Zaganelli, S. Cecchi, E. Zallo, R. Calarco, E. Luna, J. Honolka, M. Vondráček, S.

Colonna, F. Arciprete, *Increasing Optical Efficiency in the Telecommunication Bands of Strain-Engineered Ga(As,Bi) Alloys*, Phys. Rev. Appl. **14**, 014028 (2020).

[16] R. Loudon, *The Raman effect in crystals*, Adv. Phys. **13**, 423 (1964).

[17] R. Merlin, A. Pinczuk, and W. H. Weber, *Overview of Phonon Raman Scattering in Solids*, in *Raman Scattering in Materials Science*, edited by R. Merlin and W. H. Weber (Springer, New York, 2000).

[18] J. Menendez, *Characterization of Bulk Semiconductors Using Raman Spectroscopy*, in *Raman Scattering in Materials Science*, edited by W. H. Weber and R. Merlin (Springer, New York, 2000).

[19] R.A. Muñoz-Hernández, S. Jiménez-Sandoval, G. Torres-Delgado, C. Roch, X.K. Chen, J.C. Irwin, *Light scattering in p-type GaAs:Ge*, J. Appl. Phys. **80**, 2388 (1996).

[20] J.A. Steele, R.A. Lewis, M. Henini, O.M. Lemine, A. Alkaoud, *Raman scattering studies of strain effects in (100) and (311)B GaAs 1-xBix epitaxial layers*, J. Appl. Phys. **114**, 19351 (2013).

[21] M. J. Seong, S. Francoeur, S. Yoon, A. Mascarenhas, S. Tixier, M. Adamcyk, and T. Tiedje, *Bi-Induced Vibrational Modes in GaAsBi*, Superlattices Microstruct. **37**, 394 (2005).

[22] F. Sarcan, Ö. Dönmez, K. Kara, A. Erol, E. Akalın, M. Çetin Arıkan, H. Makhloufi, A. Arnoult, C. Fontaine, *Bismuth-induced effects on optical, lattice vibrational, and structural properties of bulk GaAsBi alloys*, Nanoscale Res. Lett. **9**, 119 (2014).

[23] J. A. Steele, R. A. Lewis, M. Henini, O. M. Lemine, D. Fan, Y. I. Mazur, V. G. Dorogan, P. C. Grant, S.-Q. Yu, and G. J. Salamo, *Raman Scattering Reveals Strong LO-Phonon-Hole-Plasmon Coupling in Nominally Undoped GaAsBi: Optical Determination of Carrier Concentration*, Opt. Express **22**, 11680 (2014).

[24] J. Li, K. Forghani, Y. Guan, W. Jiao, W. Kong, K. Collar, T.H. Kim, T.F. Kuech, and A.S. Brown, *GaAs1-yBiy Raman signatures: Illuminating relationships between the electrical and optical properties of GaAs1-yBiy and Bi incorporation*, AIP Adv. **5**, 067103 (2015).

[25] P. Wang, W. Pan, X. Wu, C. Cao, S. Wang, Q. Gong, *Heteroepitaxy growth of GaAsBi on Ge(100) substrate by gas source molecular beam epitaxy*, Appl. Phys. Express. **9**, 045502 (2016).

[26] A. Erol, E. Akalin, K. Kara, M. Aslan, V. Bahrami-Yekta, R.B. Lewis, T. Tiedje, *Raman and AFM studies on nominally undoped, p- and n-type GaAsBi alloys*, J. Alloys Compd. **722**, 339 (2017).

[27] R. Butkutė, G. Niaura, E. Pozingytė, B. Čechavičius, A. Selskis, M. Skapas, V. Karpus, A. Krotkus, *Bismuth Quantum Dots in Annealed GaAsBi/AlAs Quantum Wells*, Nanoscale Res. Lett. **12**, 436 (2017).

[28] A.S. Pashchenko, L.S. Lunin, S.N. Chebotarev, M.L. Lunina, *Study of the Structural and Luminescence Properties of InAs/GaAs Heterostructures with Bi-Doped Potential Barriers*, Semiconductors. **52**, 729 (2018).

[29] R.S. Joshya, V. Rajaji, C. Narayana, A. Mascarenhas, R.N. Kini, *Anharmonicity in light scattering by optical phonons in GaAs1-xBix*, J. Appl.

Phys. **119**, 20570 (2016).

[30] P. Verma, K. Oe, M. Yamada, H. Harima, M. Herms, G. Irmer, *Raman Studies on GaAs1−xBi x and InAs1−xBix*, J. Appl. Phys. **89**, 1657 (2001).

[31] S. Souto, J. Hilska, Y. Galvão Gobato, D. Souza, M.B. Andrade, E. Koivusalo, J. Puustinen, M. Guina, *Raman spectroscopy of GaSb1-xBixalloys with high Bi content*, Appl. Phys. Lett. **116**, 202103 (2020).

[32] A. Mooradian, A.L. McWhorter, *Polarization and intensity of Raman scattering from plasmons and phonons in gallium arsenide*, Phys. Rev. Lett. **19**, 849 (1967).

[33] A. Mooradian, G.B. Wright, *Observation of the Interaction of Plasmons with Longitudinal Optical Phonons in GaAs*, Phys. Rev. Lett. **16**, 999 (1966).

[34] M. Cardona, *Proceedings of the 15th International Conference on the Physics of Semiconductors, Kyoto, Sept. 1st-5th, 1980*, in *Journal of the Physical Society of Japan, v.49(1980) Suppl. A.*, edited by S. Tanaka and Y. Toyozawa (Physical Society of Japan, Kyoto, 1980), p. 23.

[35] D. Olego, M. Cardona, *Raman scattering by coupled LO-phononplasmon modes and forbidden TO-phonon Raman scattering in heavily doped p-type GaAs*, Phys. Rev. B. **24**, 7217 (1981).

[36] G. Abstreiter, M. Cardona, and A. Pinczuk, *Light Scattering by Free Carrier Excitations in Semiconductors*, in *Light Scattering in Solids IV. Topics in Applied Physics, Vol 54*, edited by M. Cardona and G. Güntherodt (Springer, Berlin, 1984).

[37] R. Fukasawa and S. Perkowitz, *Raman-scattering spectra of coupled LO-phonon-hole-plasmon modes in p-type GaAs*, Phys. Rev. B. **50**, 14119 (1994).

[38] G. Irmer, M. Wenzel, J. Monecke, *Light scattering by a multicomponent plasma coupled with longitudinal-optical phonons: Raman spectra of-type GaAs:Zn*, Phys. Rev. B - Condens. Matter Mater. Phys. **56**, 9524 (1997).

[39] J. Hu, O. V. Misochko, A. Goto, K.G. Nakamura, *Delayed formation of coherent LO phonon-plasmon coupled modes in n- and p-type GaAs measured using a femtosecond coherent control technique*, Phys. Rev. B - Condens. Matter Mater. Phys. **86**, 235145 (2012).

[40] R. Srnanek, G. Irmer, J. Geurts, M. Lentze, D. Donoval, B. Sciana, D. Radziewicz, M. Tlaczala, M. Florovic, and I. Novotny, *Micro-Raman Study of Photoexcited Plasma in GaAs Bevelled Structures*, Appl. Surf. Sci. **243**, 96 (2005).

[41] J. E. Kardontchik and E. Cohen, *Raman Scattering from Plasmons in Photoexcited GaP*, Phys. Rev. Lett. **42**, 669 (1979).

[42] A. Pinczuk, J. Shah, P.A. Wolff, *Collective modes of photoexcited electron-hole plasmas in GaAs*, Phys. Rev. Lett. **47**, 1487 (1981).

[43] S. Yoon, M.J. Seong, B. Fluegel, A. Mascarenhas, S. Tixier, T. Tiedje, *Photogenerated plasmons in GaAs1-xBix*, Appl. Phys. Lett. **91**, 082101 (2007).

[44] H. Talaat, T. A. El-Brolossy, S. Negm, and S. Abdalla, *Photomodulation of the Coupled Plasmon-LO Phonon of GaAs Surfaces*, J. Phys. Condens.

Matter **15**, 5829 (2003).

[45] S. Zhu, W. Qiu, H. Wang, T. Lin, P. Chen, and X. Wang, *Raman Spectroscopic Determination of Hole Concentration in Undoped GaAsBi*, Semicond. Sci. Technol. **34**, 015008 (2019).

[46] J. A. Steele, *Structural and Optical Studies of GaAs1-XBix and p-Bi203 for Optoelectronic Devices*. (University of Wollongong, 2015).

[47] M. Usman, C.A. Broderick, A. Lindsay, E.P. O'Reilly, *Tight-binding analysis of the electronic structure of dilute bismide alloys of GaP and GaAs*, Phys. Rev. B - Condens. Matter Mater. Phys. **84**, 245202 (2011).

[48] X. Lu, D.A. Beaton, R.B. Lewis, T. Tiedje, Y. Zhang, *Composition dependence of photoluminescence of GaAs1-x Bi x alloys*, Appl. Phys. Lett. **95**, 041903 (2009).

[49] R. Kudrawiec, M. Syperek, P. Poloczek, J. Misiewicz, R.H. Mari, M. Shafi, M. Henini, Y.G. Gobato, S. V. Novikov, J. Ibáñez, M. Schmidbauer, S.I. Molina, *Carrier localization in GaBiAs probed by photomodulated transmittance and photoluminescence,* J. Appl. Phys. **106**, 02351 (2009).

[50] M. Usman, C.A. Broderick, Z. Batool, K. Hild, T.J.C. Hosea, S.J. Sweeney, E.P. O'Reilly, *Impact of alloy disorder on the band structure of compressively strained GaBixAs1-x,* Phys. Rev. B - Condens. Matter Mater. Phys. **87**, 115104 (2013).

[51] Z. Batool, K. Hild, T.J.C. Hosea, X. Lu, T. Tiedje, S.J. Sweeney, *The electronic band structure of GaBiAs/GaAs layers: Influence of strain and band anti-crossing,* J. Appl. Phys. **111**, 11310 (2012).

[52] M. Yoshimoto, M. Itoh, Y. Tominaga, and K. Oe, *Quantitative Estimation of Density of Bi-Induced Localized States in GaAs1-XBix Grown by Molecular Beam Epitaxy*, J. Cryst. Growth **378**, 73 (2013).

[53] R. Kudrawiec, M. Latkowska, M. Welna, J. Misiewicz, M. Shafi, R.H. Mari, M. Henini, W. Walukiewicz, *Correlations between the band structure, activation energies of electron traps, and photoluminescence in n-type GaNAs layers*, Appl. Phys. Lett. **101**, 082109 (2012).

[54] T. Wilson, N.P. Hylton, Y. Harada, P. Pearce, D. Alonso-Álvarez, A. Mellor, R.D. Richards, J.P.R. David, N.J. Ekins-Daukes, *Assessing the Nature of the Distribution of Localised States in Bulk GaAsBi*, Sci. Rep. **8**, 6457 (2018).

[55] K. Alberi, T.M. Christian, B. Fluegel, S.A. Crooker, D.A. Beaton, A. Mascarenhas, *Localization behavior at bound Bi complex states in GaA s1-x B ix*, Phys. Rev. Mater. **1**, 024605 (2017).

[56] K. Alberi, B. Fluegel, D.A. Beaton, M. Steger, S.A. Crooker, A. Mascarenhas, *Origin of deep localization in GaA s 1-x B ix and its consequences for alloy properties*, Phys. Rev. Mater. **2**, 114603 (2018).

[57] R. Kudrawiec, M. Syperek, P. Poloczek, J. Misiewicz, R.H. Mari, M. Shafi, M. Henini, Y.G. Gobato, S. V. Novikov, J. Ibáñez, M. Schmidbauer, S.I. Molina, *Carrier localization in GaBiAs probed by photomodulated transmittance and photoluminescence*, J. Appl. Phys. **106**, 023518 (2009).

[58] A.R. Mohmad, F. Bastiman, J.S. Ng, S.J. Sweeney, J.P.R. David, *Photoluminescence investigation of high quality GaAs1-x Bi x on GaAs*, Appl. Phys. Lett. **98**, 122107 (2011).

[59] S. Imhof, A. Thränhardt, A. Chernikov, M. Koch, N.S. Köster, K. Kolata, S. Chatterjee, S.W. Koch, X. Lu, S.R. Johnson, D.A. Beaton, T. Tiedje, O. Rubel, *Clustering effects in Ga(AsBi)*, Appl. Phys. Lett. **96**, 131115 (2010).

[60] M.K. Shakfa, D. Kalincev, X. Lu, S.R. Johnson, D.A. Beaton, T. Tiedje, A. Chernikov, S. Chatterjee, M. Koch, *Quantitative study of localization effects and recombination dynamics in GaAsBi/GaAs single quantum wells*, J. Appl. Phys. **114**, 164306 (2013).

[61] O. Donmez, A. Erol, M.C. Arikan, H. Makhloufi, A. Arnoult, C. Fontaine, *Optical properties of GaBiAs single quantum well structures grown by MBE*, Semicond. Sci. Technol. **30**, 094016 (2015).

[62] M. Latkowska, R. Kudrawiec, G. Sk, J. Misiewicz, J. Ibáez, M. Henini, M. Hopkinson, *Thermal quenching of single localized excitons in GaInNAs layers*, Appl. Phys. Lett. **98**, 8 (2011).

[63] G. Pettinari, A. Patanè, A. Polimeni, M. Capizzi, X. Lu, T. Tiedje, *Bi-induced p-type conductivity in nominally undoped Ga(AsBi)*, Appl. Phys. Lett. **100**, 092109 (2012).

[64] G.A. Prando, V. Orsi Gordo, J. Puustinen, J. Hilska, H.M. Alghamdi, G. Som, M. Gunes, M. Akyol, S. Souto, A.D. Rodrigues, H.V.A. Galeti, M. Henini, Y.G. Gobato, M. Guina, *Exciton localization and structural disorder of GaAs1-xBix/GaAs quantum wells grown by molecular beam epitaxy on (311)B GaAs substrates*, Semicond. Sci. Technol. **33**, 084002 (2018).

[65] Y. Zhang, A. Mascarenhas, L.W. Wang, *Similar and dissimilar aspects of III-V semiconductors containing Bi versus N*, Phys. Rev. B - Condens.

Matter Mater. Phys. **71**, 155201 (2005).

[66] S. Mazzucato, H. Lehec, H. Carrère, H. Makhloufi, A. Arnoult, C. Fontaine, T. Amand, X. Marie, *Low-temperature photoluminescence study of exciton recombination in bulk GaAsBi*, Nanoscale Res. Lett. **9**, 19 (2014)

[67] S. Mazzucato, P. Boonpeng, H. Carrère, D. Lagarde, A. Arnoult, G. Lacoste, T. Zhang, A. Balocchi, T. Amand, X. Marie, C. Fontaine, *Reduction of defect density by rapid thermal annealing in GaAsBi studied by time-resolved photoluminescence*, Semicond. Sci. Technol. **28**, 022001 (2013).

[68] S. Imhof, C. Wagner, A. Thränhardt, A. Chernikov, M. Koch, N.S. Köster, S. Chatterjee, S.W. Koch, O. Rubel, X. Lu, S.R. Johnson, D.A. Beaton, T. Tiedje, *Luminescence dynamics in Ga(AsBi)*, Appl. Phys. Lett. **98**, 161104 (2011).

[69] M. Yoshimoto and K. Oe, *Present Status and Future Prospects of Bi-Containing Semiconductors*, 1st Int. Work. Bismuth Contain. Semicond., (2010).

[70] T. Schmidt, K. Lischka, W. Zulehner, *Excitation-power dependence of the near-band-edge photoluminescence of semiconductors*, Phys. Rev. B. **45,** 8989 (1992).

CHAPTER 9: CONCLUSION AND FUTURE WORK

This chapter summarises the research work carried out on the electrical and optical properties of dilute bismide (GaAsBi) materials. XRD, I-V, C-V, DLTS, Laplace DLTS, Raman and PL characterization techniques were used to investigate these alloys. Future work suggestions also are presented in this chapter.

9.1 CONCLUSION

In summary, deep level defects in n-type GaAsBi layers grown by MBE on GaAs (100) and (311)B planes, with Bi concentration of 5.4%, were investigated using DLTS and LDLTS. It was observed that the incorporation of Bi into GaAs suppresses the formation of GaAs electron traps by reducing their total trap concentration by more than two order of magnitude compared to trap concentration in GaAs. In addition, the DLTS measurements showed that the number of defects were different in the structures grown on the two GaAs substrate orientations, namely (100) and (311)B planes. Additionally, PL and Raman were also used to investigate the optical properties of those alloys. Both techniques revealed that traps states of Bi-induced and the existence of different compressive strain affect the optical properties of (100) and (311)B GaAsBi layers. Also in this thesis, the effects of gamma (γ-) irradiation dose on the electrical and optical properties of dilute GaAsBi layers have been studied. After irradiation the samples exposed to gamma rays showed better diode performance. DLTS and LDLTS measurements revealed that after irradiation the number of defects decreased. In addition, the optical results showed an enhancement in the PL peak intensity with increasing radiations doses, indicating a reduction of radiative centres which can also influence the photoluminescence properties of GaAsBi layers. Furthermore, this investigation evidenced that Bi alloys materials present high potential for applications in ionizing radiation detectors that could be monitored by both electrical and optical measurements. Furthermore, XRD, micro-Raman at room temperature, and PL measurements as a function of temperature and laser excitation power (P_{EXC}) were used to investigate the structural and optical properties of n-type Si-doped and p-type Be-doped $GaAs_{1-x}Bi_x$ thin films grown by MBE on (311)B GaAs substrates. This study indicated that the density of Bi related defects depend on the type of doping (n- or p-doping) of $GaAs_{1-x}Bi_x$, which have different effects on the PL properties of n- and p-doped GaBiAs layers grown on (311)B substrate orientation. These defects have important contribution in the presence of non-radiative centers and also contribute to different radiative recombination.

9.2 FUTURE WORK SUGGESTIONS

Suggestions for further investigations are proposed based on the experimental results obtained in this thesis as follows:

(i) It is well known that heat treatment process reduce the concentration of defects and/or eliminate completely defects. Hence, the electrical, optical and structural properties of the materials and devices will be improved. Indeed, several reports have shown that the post-growth thermal annealing enhances the structural and optical properties of GaAsBi materials [1–4]. However, the effect of thermal annealing on the electrically active defects has not been investigated yet. Therefore, it is of paramount importance to perform electrical measurements to investigate the annealing effects on these defects states in order to improve the quality of the material and understand the effect of deep level defects on the performance of future devices based on these materials systems.

(ii) In case of dilute GaAsBi samples it will be worth to carry out a systematic study to investigate the effect of gamma irradiation on the electrically active defects grown on high-index GaAs substrates, in order to find the best material for high-performance ionizing radiation detectors. It would also be interesting and important to investigate the effect of different sources of irradiation on these materials, in order to determine the suitability of dilute bismide-based materials and devices for space applications such as satellite communications.

(iii) For n-type Si-doped and p-type Be-doped $GaAs_{1-x}Bi_x$ structures, it is worth performing further studies on same structures and under similar growth conditions without intentionally doping (intrinsic alloy). This could provide easier identification of the doping effect, and also help to improve the quality of the material and understand the role of doping type on the performance of future devices based on these material systems.

REFERENCES

[1] H. Makhloufi, P. Boonpeng, S. Mazzucato, J. Nicolai, A. Arnoult, T. Hungria, G. Lacoste, C. Gatel, A. Ponchet, H. Carrère, X. Marie, C. Fontaine, *Molecular beam epitaxy and properties of GaAsBi/GaAs quantum wells grown by molecular beam epitaxy: effect of thermal annealing*, Nanoscale Res. Lett. **9,** 1 (2014).

[2] Grant, Perry C., Dongsheng Fan, Aboozar Mosleh, Shui-Qing Yu, Vitaliy G. Dorogan, Michael E. Hawkridge, Yuriy I. Mazur, Mourad Benamara, Gregory J. Salamo, and Shane R. Johnson, *Rapid thermal annealing effect on GaAsBi/GaAs single quantum wells grown by molecular beam epitaxy*, Journal of Vacuum Science and technology B, Microelectron. Nanom. Struct. **32,** 02C119 (2014).

[3] H. Alghamdi, V.O. Gordo, M. Schmidbauer, J.F. Felix, S. Alhassan, A. Alhassni, G.A. Prando, H. Coelho-Júnior, M. Gunes, H.V.A. Galeti, Y.G. Gobato, M. Henini, *Effect of thermal annealing on the optical and structural properties of (311)B and (001) GaAsBi/GaAs single quantum wells grown by MBE,* J. Appl. Phys. **127,** 125704 (2020).

[4] O.M. Lemine, A. Alkaoud, H. V. Avanço Galeti, V. Orsi Gordo, Y. Galvão Gobato, H. Bouzid, A. Hajry, M. Henini, *Thermal annealing effects on the optical and structural properties of (1 0 0) GaAs1-xBix layers grown by Molecular Beam Epitaxy,* Superlattices Microstruct. **65**, 48 (2014).